Strong wind events across Greenland's coast and their influence on the ice sheet, sea ice and ocean

by

Marilena Oltmanns

B.S. in Earth and Space Sciences, Jacobs University Bremen (2009)

Submitted in partial fulfillment of the requirements for the degree of

Doctor of Philosophy

at the

MASSACHUSETTS INSTITUTE OF TECHNOLOGY

and the

WOODS HOLE OCEANOGRAPHIC INSTITUTION

June 2015

© Marilena Oltmanns, 2015. All rights reserved.

The author hereby grants to MIT and to WHOI permission to reproduce and to distribute publicly paper and electronic copies of this thesis document in whole or in part.

Author .....

Joint Program in Physical Oceanography
Massachusetts Institute of Technology
& Woods Hole Oceanographic Institution
May 22, 2014

Certified by .....

Dr. Fiamma Straneo
Senior Scientist
Woods Hole Oceanographic Institution
Thesis Supervisor

Accepted by .....

Prof. Glenn R. Flierl
Chair, Joint Committee for Physical Oceanography
Massachusetts Institute of Technology

Strong wind events across Greenland's coast and their influence on the ice sheet, sea ice and ocean

by

Marilena Oltmanns

Submitted to the Joint Program in Physical Oceanography
Massachusetts Institute of Technology
& Woods Hole Oceanographic Institution
on May 22, 2014, in partial fulfillment of the
requirements for the degree of
Doctor of Philosophy

Abstract

In winter, Greenland's coastline adjacent to the subpolar North Atlantic and Nordic Seas is characterized by a large land-sea temperature contrast. Therefore, winds across the coast advect air across a horizontal temperature gradient and can result in significant surface heat fluxes both over the ice sheet (during onshore winds) and over the ocean (during offshore winds). Despite their importance, these winds have not been investigated in detail, and this thesis includes the first comprehensive study of their characteristics, dynamics and impacts. Using an atmospheric reanalysis, observations from local weather stations, and remote sensing data, it is suggested that high-speed wind events across the coast are triggered by the superposition of an upper level potential vorticity anomaly on a stationary topographic Rossby wave over Greenland, and that they intensify through baroclinic instability. Onshore winds across Greenland's coast can result in increased melting, and offshore winds drive large heat losses over major ocean convection sites.

Strong offshore winds across the southeast coast are unique over Greenland, because the flow is funneled from the vast ice sheet inland into the narrow valley of Ammassalik at the coast, where it can reach hurricane intensity. In this region, the cold air, which formed over the northern ice sheet, is suddenly released during intense downslope wind events and spills over the Irminger Sea where the cold and strong winds can drive heat fluxes of up to 1000 W m^{-2}, with potential implications for deep water formation. Moreover, the winds advect sea ice away from the coast and out of a major glacial fjord.

Simulations of these wind events in Ammassalik with the atmospheric Weather Research and Forecast Model show that mountain wave dynamics contribute to the acceleration of the downslope flow. In order to capture these dynamics, a high model

resolution with a detailed topography is needed. The effects of using a different resolution locally in the valley extend far downstream over the Irminger Sea, which has implications for the evolution and distribution of the heat fluxes.

Thesis Supervisor: Dr. Fiamma Straneo
Title: Senior Scientist
Woods Hole Oceanographic Institution

Acknowledgments

First I would like to thank my advisor Fiamma Straneo, for her extraordinary support throughout my time in the Joint Program. She has given me countless helpful advice both with regard to my research and my career, has always encouraged me, and made time for me even when her schedule was already crammed. Fiamma has given me great academic freedom, inspired me in my research and beyond, and given me confidence. I am very grateful that I could be part of her group, and I know that I will benefit from this time in my future work and life.

My thesis committee consisting of Claudia Cenedese, Kerry Emanuel, Glenn Flierl, Steve Lentz and Kent Moore has also supported me in my research. Thus, they have contributed to improving the quality of this thesis. I am particularly thankful to Kent Moore for always giving me constructive feedback and valuable advice, especially when I got started with my thesis research. Other scientists at WHOI and MIT, for instance Hyodae Seo, Young-Oh Kwon and Joseph Pedlosky have also provided helpful comments and suggestions, and they always had time when I had a question.

In addition, I have received support from Fiamma's group members including Clark Richards, Magdalena Andres, Andree Ramsey, Becca Jackson, Nat Wilson, Ben Harden, Laura Stevens, Nick Beaird, Ken Mankoff, and Mattias Cape, as well as from fellow students, e.g. Wilken von Appen, Julian Schanze, Ru Chen, Ping Zhai, Elise Olson, Alec Bogdanoff, Deepak Cherian, Isabela Le Bras, Melissa Moulton, Dan Amrhein, Nick Woods and many others.

I would further like to acknowledge the following data and research centers that collect, archive and/or distribute the data and model products used in this thesis: the European Centre for Medium-Range Weather Forecasts (ECMWF), the Danish Meteorological Institute (DMI), the Geological Survey of Denmark and Greenland (GEUS), the Steffen Research Group at the Cooperative Institute for Research in Environmental Sciences (CIRES), the National Aeronautics and Space Administration (NASA), the University of Copenhagen, the National Snow and Ice Data Center (NSIDC), the University of Hamburg, and the University Corporation for Atmospheric Research (UCAR). Financially, this work was supported by grants of the National Science Foundation (OCE-0751554 and OCE-1130008) as well as the Natural Sciences and Engineering Research Council of Canada.

Contents

Chapter 1

Introduction

Greenland and the surrounding subpolar North Atlantic ocean (Figure 1-1a) are regions of large climatic significance. Greenland, on the one hand, stores sufficient freshwater in its ice sheet to raise global mean sea level by 7 m [Houghton et al., 2001]. Furthermore, increased freshwater runoff from the Greenland ice sheet could also affect global ocean circulation by freshening the North Atlantic [Manabe and Stouffer, 1995, Stammer, 2008, Marsh et al., 2010, Weijer et al., 2012, Hu et al., 2013]. In recent years, the ice sheet has undergone rapid changes. Its mass loss has quadrupled from 51 ± 65 Gt yr^{-1} between 1992 and 2001 to 211 ± 37 Gt yr^{-1} between 2002 and 2011 and thereby raised global mean sea level by 7.5 ± 1.8 mm from 1992 to 2011 [Shepherd et al., 2012, Hanna et al., 2013]. These changes show how variable the mass balance of the ice sheet is, and since part of its mass loss has been attributed to increased surface melt [Van Den Broeke et al., 2009, Hanna et al., 2011, Hall et al., 2013], they also suggest that alterations in its surface energy budget entail large-scale climatic consequences.

On the other hand, the subpolar North Atlantic and Nordic Seas bordering the southwest, southeast and east coast, include three of the few locations where dense waters are formed, which are the Greenland Sea [Rudels and Quadfasel, 1991, Böning et al., 1996], the Labrador Sea [Talley and McCartney, 1982, Clarke and Gascard,

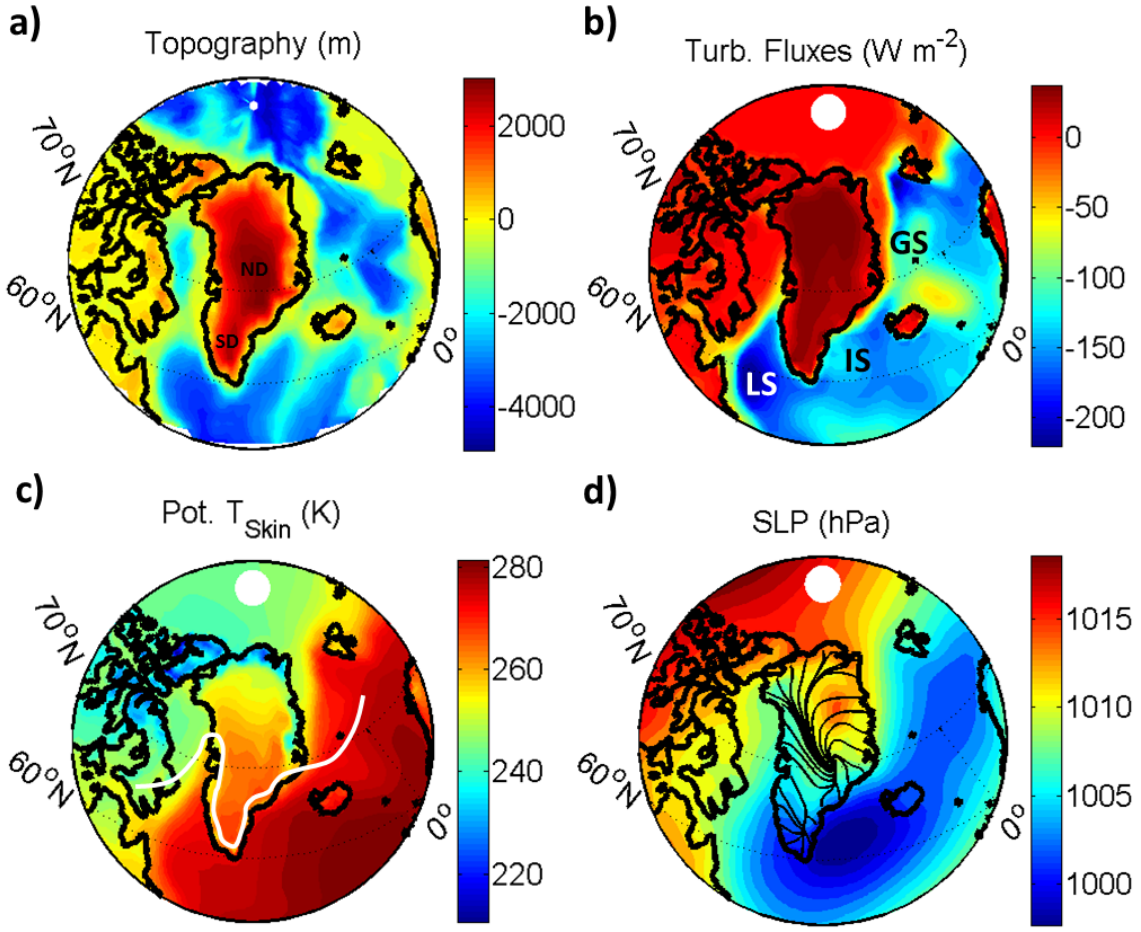

Figure 1-1: (a) The high elevation of Greenland represents a barrier to the mean westerly atmospheric flow. SD indicates the location of the southern dome and ND that of the northern dome. The region between them is referred to as the Saddle region. (b) Large winter (DJFM) mean heat losses occur over the ocean southwest, southeast and east of Greenland (based on ERA-I). IS indicates the location of the Irminger Sea, GS is the Greenland Sea, and LS is the Labrador Sea. Over the ice sheet, the winter mean turbulent heat fluxes are positive, meaning that heat is transferred from the atmosphere into the surface. (c) As a frontier to the Arctic, Greenland's winter mean potential skin temperature increases from the northwest to the southeast (based on ERA-I). The white line indicates the approximate border of the high Arctic zone, defined as the region where the average temperature during the warmest month lies below 5 °C. (d) The winter mean sea level pressure (SLP) field is characterized by an anticyclone over northeast Greenland and the Icelandic Low over the Irminger Sea. The streamlines over Greenland are based on the winter mean 10m-wind field. They start over the southern and northern dome and end at the coast. Both the SLP and the wind field are obtained from ERA-I.

1983, Gascard and Clarke, 1983], and the Irminger Sea [Pickart et al., 2003b, Våge et al., 2011, de Jong et al., 2012] (Figure 1-1b). Ocean convection in these regions constitutes an integral component of the Atlantic Meriodional Overturning Circulation (AMOC), and thus the northward ocean heat transport [Trenberth and Caron, 2001]. Studies have suggested that the AMOC is not a stable circulation [Bryden et al., 2005], and variations in the northward ocean heat transport in the past have been linked with abrupt climate change [Clark et al., 2002, McManus et al., 2004, Gherardi et al., 2005, Lynch-Stieglitz et al., 2007]. Since deep convection is forced by buoyancy losses at the surface [Marshall and Schott, 1999], changes in the surface energy budget of the ocean convection sites around Greenland can influence the northern part of the AMOC and thus have large scale implications.

The energy budget of the subpolar North Atlantic and the ice sheet is in turn affected by turbulent heat fluxes across the surface [Serreze and Barry, 2005]. In winter, the mean turbulent heat fluxes are directed into the surface over Greenland and out of the surface over the ocean, implying that the ocean loses heat to the atmosphere (Figure 1-1b). This heat loss can in part be explained by the comparatively warm ocean surface, which results from currents advecting warm subtropical water masses into the subpolar North Atlantic and Nordic Seas [Siedler et al., 2001]. The advection of warm water near Greenland's coast creates a land-sea temperature contrast across the southwest, southeast and east coast, especially in winter (Figure 1-1c), and this temperature contrast can be amplified through the lower albedo over the ocean, which results in more absorbed solar radiation, compared to the ice sheet [Bonan, 2002]. Therefore, winds across the coast advect air across a horizontal temperature gradient and can give rise to large sensible heat fluxes. While onshore winds can advect heat onto the ice sheet, offshore winds can result in large heat losses over the subpolar North Atlantic and Nordic Seas. Thus, the atmospheric circulation around Greenland can influence the surface energy balance over the ice sheet and over the ocean through winds across the coast.

The atmospheric circulation over Greenland is in turn affected by the ice sheet, both mechanically and thermodynamically. The thermodynamic influence is related to the radiation balance over the ice sheet. In winter, the net radiation over the ice sheet is negative, causing the air masses above to cool and sink [Born and Boecher, 2000]. Thus, a region of high thermal pressure develops over the ice cap and a temperature inversion forms above a layer of cold, dense air. This results in a katabatic flow down the smooth terrain of the central ice sheet that accelerates near the steeper coasts (Figure 1-1d) [Schwerdtfeger, 1984, Parish and Bromwich, 1987, Rasmussen, 1989, Bromwich et al., 1996, Parish and Cassano, 2001]. In summer, the high pressure field weakens and the katabatic flow is less pronounced.

The mechanical influence of Greenland on the atmosphere arises from its high elevation of $\sim$3000 m that represents a considerable obstacle to the mean westerly flow (Figure 1-1a). The interaction of synoptic weather systems with the high topography can result in intense wind events, particularly around southern Greenland, which is one of the windiest regions in the World Ocean [Sampe and Xie, 2007]. Among these wind events are tip jets around the southern tip of Greenland [Doyle and Shapiro, 1999, Våge et al., 2009, Moore and Renfrew, 2005, Renfrew et al., 2009a, Outten et al., 2009], barrier winds at different locations along the east coast [Moore and Renfrew, 2005, Petersen et al., 2009, Harden et al., 2011, Harden and Renfrew, 2012, Moore, 2012] and plateau jets along the eastern and western margin of the ice sheet [Moore et al., 2013]. Observations indicate the existence of another type of wind event associated with a strong downslope flow across Greenland's southeast coast [Klein and Heinemann, 2002, Mills and Anderson, 2003], but to date there has been no comprehensive study about this type of wind event, and winds across Greenland's coast, either onshore or offshore, have generally received very limited attention.

This gap in our knowledge about high-speed winds across Greenland's coast motivates the research described in this thesis. In Chapter 2, I will present a comprehensive analysis of the large-scale distribution, characteristics, dynamics, and influences

of strong cross-coastal wind events, mostly using an atmospheric reanalysis. I will show that strong wind events across the southeast coast have a large effect on the heat fluxes over the ice sheet and the ocean. Strong onshore winds are associated with a warming of the ice sheet and can result in melting or conduct heat deeper into the snow with implications for melting later in the year. Strong offshore winds advect cold air over the subpolar North Atlantic, resulting in large ocean heat losses. There are strong indications, that both types of wind events are triggered by the superposition of an upper level potential vorticity anomaly at the tropopause over a stationary topographic Rossby wave, and that they intensify through baroclinic instability, which culminates in the breaking of the Rossby wave.

Strong offshore winds across the southeast coast are unique over Greenland, because the flow is funneled from the vast ice sheet inland into the narrow valley of Ammassalik at the coast, where it can reach hurricane intensity. Therefore, I will investigate the local characteristics of these high-speed wind events in southeast Greenland in more detail in Chapter 3 using the reanalysis and meteorological stations. In addition, I will study their dynamics, and show that both the local topographic and the large-scale atmospheric forcing are important during the wind events. As previous studies have suggested that ocean convection is driven by intense, intermittent wind events [Marshall and Schott, 1999], I will further analyze the immediate impact of strong individual wind events on the heat loss over the Irminger Sea. I will show that heat fluxes during individual events can reach 1000 W m^{-2} and that these events significantly contribute to the total heat loss in this region. Based on satellite data, I also find that downslope wind events in southeast Greenland advect sea ice off the shelf and out of the local fjord, with potential implications for the coastal ecology and the local outlet glacier. A modified version of this chapter has been published in the Journal of Climate [Oltmanns et al., 2014] and is reprinted here with permission of the American Meteorological Society.

The dynamical analysis in Chapter 3 is based on the reanalysis which does not

obtain the full wind speed observed by the weather stations. Therefore, a more detailed investigation of smaller scale processes, unresolved by the reanalysis, will be carried out in Chapter 4 using higher resolution model simulations. I will show that small-scale dynamics associated with mountain waves contribute to the acceleration of the downslope flow, and that a high model resolution with a detailed topography is needed to capture these dynamics. The effects of using a different resolution over the steep coastal slope extend downstream over the Irminger Sea with implications for the distribution and evolution of the heat fluxes. A modified version of this chapter is currently in press in the Journal of the Atmospheric Sciences and reprinted here with the permission of the American Meteorological Society. In Chapter 5, I will reflect on how the results of this thesis contribute to advancing the scientific understanding of ice-ocean-atmosphere interactions around Greenland, and suggest future study directions.

Chapter 2

Large surface heat fluxes over the ice sheet and ocean driven by winds across Greenland's southeast coast

2.1 Abstract

As a frontier to the Arctic, Greenland is characterized by a large land-sea temperature contrast such that strong winds across the southwest, southeast, and east coast advect air perpendicular to a horizontal temperature gradient and can result in significant sensible heat fluxes. Here, the dynamics and influences of high-speed winds across Greenland's coast are investigated using the atmospheric reanalysis ERA-I, weather stations and remote sensing data. It is found that the largest heat fluxes result from high-speed wind events across the southeast coast (onshore and offshore). Both types of wind events are triggered by the superposition of an upper level potential vorticity anomaly on a stationary topographic Rossby wave over Greenland, and there are strong indications that they intensify through baroclinic instability. Offshore flow is generally preceded (followed) by flow across the Arctic border to the west (north). They advect cold air over the Labrador, Irminger and Greenland Seas,

and are highly correlated with the winter mean heat losses of these ocean convection regions. Onshore winds advect warm air from the ocean and upper levels over the ice sheet and can cause increased melting. The occurrence of these flows across the southeast coast, or similarly the phase of the topographic Rossby wave, is connected with the previously identified blocking mode over Greenland. Thus, this study provides a physical link between the large-scale climate mode, the topographically forced wind events, and their impact on the ice sheet and ocean.

2.2 Introduction

Greenland is a frontier to the Arctic. From the northwest, where it borders the Arctic Ocean, to the southeast, where it borders the Irminger Sea, the winter mean potential temperature difference can be as high as 40 °C (Figure 1-1c). The border of the high Arctic zone, defined as the region where the average temperature during the warmest month lies below 5 °C [Born and Boecher, 2000], runs approximately along Greenland's southwest, southeast and east coast. High-speed winds across these coasts (both onshore and offshore) advect air normal to a horizontal temperature gradient and can result in large sensible surface heat fluxes over the ocean and the ice sheet.

Offshore winds across the coast advect cold air from the ice sheet over the ocean. Next to the east, southeast and southwest coast, the ocean loses heat to the atmosphere in winter (Figure 1-1b). These regions (the Greenland, Irminger and Labrador Seas respectively) are ocean convection sites that feed the northern branch of the Atlantic Meridional Overturning Circulation (AMOC) [Talley and McCartney, 1982, Clarke and Gascard, 1983, Gascard and Clarke, 1983, Rudels and Quadfasel, 1991, Marshall and Schott, 1999, Pickart et al., 2003b]. The substantial amount of heat transported poleward as part of the AMOC has profound influences on many aspects of the global climate system [Survey, 2012]. By preconditioning deep convection

through large surface heat fluxes, cold winds from the Arctic could have larger scale implications. Specifically, they could affect the climate of northwest Europe [Vellinga and Wood, 2002] and the sequestration of carbon dioxide by the deep ocean [Sabine et al., 2004]. Despite their potential importance, the effects of strong offshore winds across Greenland's coast have not yet been studied in detail. Thus, in this chapter, I will investigate the influences of these offshore winds across Greenland's coast on the downstream air-sea fluxes.

Onshore winds across the southeast, east and southwest coast can advect warm air onto the ice sheet which could impact melting. Even if the temperature does not reach above freezing, the heat anomaly that is transferred to the ice through sensible surface fluxes can be conducted into deeper layers and stored in the ice sheet [Serreze and Barry, 2005], and potentially speed up melting later in the year. Thereby, warm and strong onshore winds could affect the surface mass balance of the ice sheet with consequences for sea level rise. Moreover, when melting occurs in fall, winter or spring and is followed by refreezing, it can affect ecosystems as animals cannot reach the vegetation underneath [Born and Boecher, 2000]. In peak summer, winds over Greenland are weaker compared to winter, fall and spring, and inland the radiative fluxes are more important than the turbulent heat fluxes [Serreze and Barry, 2005]. Yet, even the summer temperature over Greenland is strongly linked to the atmospheric circulation [Fettweis et al., 2011, Overland et al., 2012, Fettweis et al., 2013, Hanna et al., 2013] and extremely warm summers have been associated with preceding warm air advection over the ice sheet [Box et al., 2012, Hanna et al., 2014]. The advection of warm air, in turn, has been linked to an anticyclonic circulation over Greenland that results in warm southerly winds across the western coast [Hanna et al., 2014]. In this chapter, I will investigate the characteristics of onshore winds also across the southeast and east coast of Greenland, and study their effect on the surface energy balance over the ice sheet.

Given the potentially large impacts of strong onshore and offshore winds, it is

important to understand their dynamics and predictability. Greenland itself likely plays a crucial role in forcing the cross-coastal flows, as previous studies have found that the interaction of the large-scale atmosphere with the high topography (shown in Figure 1-1a) creates strong wind events, particularly near the east coast [Moore, 2003]. These include tip jets around the southern tip of Greenland [Doyle and Shapiro, 1999, Våge et al., 2009, Moore and Renfrew, 2005, Renfrew et al., 2009a, Outten et al., 2009] and barrier winds at different locations along the east coast [Moore and Renfrew, 2005, Petersen et al., 2009, Harden et al., 2011, Harden and Renfrew, 2012, Moore, 2012], and it was found that both types of wind events are associated with deep cyclones. In fact, the regions off the southwest, southeast and east Greenland coast are characterized by a particularly high cyclone frequency and large deepening rates [Zhang et al., 2004, Tsukernik et al., 2007]. The deepening rates have been attributed to cyclone bifurcation around the southern tip of Greenland [Moore and Vachon, 2002, Kurz, 2004] and lee cyclogenesis east [Kristjánsson and McInnes, 1999, Skeie et al., 2006] and southeast of Greenland [Kristjánsson et al., 2009], and numerical model simulations and case studies suggest that, in each case, the high topography of Greenland is crucial for cyclone development [Kristjánsson and McInnes, 1999, Skeie et al., 2006, Kristjánsson et al., 2009]. Yet, the role of the topography in forcing specifically strong onshore or offshore wind events across different coastal regions, as well as their connection to large-scale atmospheric flow regimes, remains to be determined.

The questions that I am addressing in this chapter are therefore:

- Where do strong wind events across Greenland's coast occur?
- What are their large-scale characteristics?
- When (or how) do they occur?
- What is the role of offshore winds across the coast for ocean heat losses over the convection sites?

- Can onshore winds influence the surface energy balance of the ice sheet?

First, I will characterize strong onshore and offshore wind events across Greenland's coast with the reanalysis product ERA-Interim, and show that winds across the southeast coast have the largest effect on the heat fluxes both over the ocean (in the case of offshore winds) and over the ice sheet (in the case of onshore winds). Next, I will investigate the large-scale dynamic setting of these wind events, and show that they are triggered by the superposition of an upper level potential vorticity anomaly at the tropopause on a stationary topographic Rossby wave over Greenland. There are strong indications that the wind events intensify through baroclinic instability, which culminates in the breaking of the Rossby wave. The phase of the topographic Rossby wave, and thus the variability of the flow across the southeast coast, is connected with the blocking mode over Greenland. Lastly, I study the influences of strong offshore and onshore flows across the southeast coast. I find that offshore flows are indeed associated with large heat losses over the subpolar North Atlantic and Nordic Seas. Using ERA-I, weather stations and satellite data, I further show that onshore flows across the southeast coast can result in melting and store anomalous heat in deeper layers of the snow with implications for melting later in the year.

2.3 Background

The surface energy budget in the Arctic can be described by a balance between radiative fluxes and non-radiative fluxes [Serreze and Barry, 2005, Serreze et al., 2007]. The total radiative fluxes (R_{net}) include shortwave (Q_{SW}) and longwave radiation (Q_{LW}):

$$R_{net} = Q_{SW} + Q_{LW}. \tag{2.1}$$

Q_{SW} represents the net absorbed radiation, $Q_{SW} = R_{SW}\,(1 - \alpha)$, where R_{SW} is the total downward shortwave radiation and α is the albedo of the surface. Fresh snow

has an albedo between 0.7 and 0.9, whereas melting snow has an albedo between 0.5 and 0.6 [Serreze and Barry, 2005]. Q_{LW} represents the net outgoing longwave radiation, $Q_{LW} = R_{LW} - \varepsilon\sigma T_S^4$, where R_{LW} is the total downward longwave radiation and the second term represents the emitted longwave flux which depends on the surface emissivity ε, the Stefan Boltzman constant σ and skin temperature T_S. Q_{SW} is positive, while Q_{LW} is usually negative, where I am using a sign convention such that negative fluxes indicate energy losses of the surface and positive fluxes indicate energy transfers into the surface. The radiative fluxes are balanced by non-radiative energy transfers:

$$R_{net} = Q_S + Q_L + M + C, \tag{2.2}$$

where Q_S is the sensible heat flux, Q_L is the latent heat flux, M represents melting and freezing directly at the interface, and C represents the conduction of heat inside the surface. The sensible and latent heat fluxes are estimated by bulk formulas (e.g. Stewart [2004], Goosse et al. [2015]):

$$Q_S = \rho C_P C_S u \cdot dT \qquad \text{and} \qquad Q_L = \rho L_E C_L u \cdot dq_s,$$

where u is wind speed, dT is the temperature difference between the surface and the air, dq_s is the specific humidity difference, ρ is the density of air, C_P is the specific heat at constant pressure, C_S is the sensible heat transfer coefficient, C_L is the latent heat transfer coefficient and L_E is the latent heat of evaporation. Again, I use a sign convention such that a positive sensible (latent) heat flux implies that the near surface air has a higher temperature (humidity) compared to the surface. The transfer coefficients depend on the stability of the atmospheric boundary layer, the wind speed and the surface roughness. Over land, the latent heat flux is also a function of water availability. Thus, the turbulent heat fluxes depend both on the temperature (or humidity) difference between the surface and the air and on wind

speed. At any particular location, the surface air temperature is itself influenced by the surface heat fluxes and horizontal advection. High-speed winds that advect air across a horizontal temperature gradient, can therefore result in large turbulent heat fluxes and will tend to equalize the temperature difference. If the flow extends over a wide part of the ice sheet and initiates melting, it can change the albedo over a large area generating a positive feedback where more solar radiation is absorbed [Box et al., 2012].

2.4 Data

To identify and describe strong winds across Greenland's coast, I use the atmospheric reanalysis ERA-Interim (ERA-I) from the European Centre for Medium-Range Weather Forecasts [Dee et al., 2011]. The model runs on 60 vertical levels and has a horizontal resolution of approximately 80 km near the surface. I mainly use the surface temperature, 10m-wind, SLP and heat flux fields in the time period between 1979 and 2012 with a 6-hourly temporal resolution.

Several studies have compared ERA-I to observations around southeast Greenland and over the ice sheet. In October 2008, a comparison with data collected over the Irminger Sea from the research vessel Knorr (KN194-4) was undertaken to verify the ERA-I product. The overall conclusion is that ERA-I reproduces surface fields well. Especially the pressure is in excellent agreement with the observations [Harden et al., 2011]. During high wind speed conditions the 10m-winds are underrepresented by $\sim$1 m s^{-1} and the 2m-air temperature has a cold bias of $\sim$2 °C. Dropsonde measurements have been compared to the vertical structure of the ERA-I output [Harden et al., 2011, Renfrew et al., 2008] and it was found that even though the basic structure of the wind and the temperature field is captured, ERA-I tends to underestimate the strength of gradients during high wind speed conditions. Over the Greenland ice sheet, the 10m-wind field was compared to observations from automated weather stations [Moore

et al., 2013] and it was found that the data agree with root mean square errors of $\sim$1 m s^{-1} and correlations of $\sim$0.65. Temperature profiles from ERA-I were compared to radiosonde data in a study about surface based inversions of the Arctic boundary layer with the overall conclusion that the data agree reasonably well with the ERA-I output [Zhang et al., 2011]. ERA-I heat fluxes have successfully been used in other studies (e.g. Moore et al. [2012], Renfrew et al. [2009b]), and a comparison of ERA-I heat fluxes with shipboard observations over the Labrador and Irminger Sea showed that the ERA-I heat fluxes were within the bounds of observational uncertainty [Renfrew and Anderson, 2002, Renfrew et al., 2009b].

In addition to the reanalysis, I use several weather stations over the Greenland ice sheet and along the coast to compare the observed winds, temperature and pressure with the ERA-I output fields. The data are distributed and quality controlled by the Danish Meteorological Institute (DMI) [Cappelen, 2011], the Greenland Climate Network (GCNet) [Steffen et al., 1996], and the Geological Survey of Denmark and Greenland (GEUS), which operates the Programme for Monitoring the Greenland Icesheet (PROMICE) [Ahlstrøm et al., 2011]. The DMI stations that I use in this study are located along the east and west coast (locations are shown in Figure 2-9). They have at least a 3-hourly resolution and cover at least 25 years, where most of the stations have a much longer data record. From the GCNet stations I mostly use station Summit over the central ice sheet (Figure 2-9), station Saddle between the southern and the northern dome, and station South Dome over the southern dome (Figures 2-12b and 2-15a) which have at least a 3-hourly resolution, and been operated since 1995, 1997 and 1997 respectively. From the PROMICE stations, I use the stations in Nuuk and Tasiilaq (Figure 2-15), which record data since 2007. Sometimes breakdowns of the stations occurred during the time period of operation, but they did not affect the results of this study and the composites obtained from these stations are based on at least 100 events (in the case of the DMI and GCNet stations) and more than 50 events (in the case of the PROMICE stations).

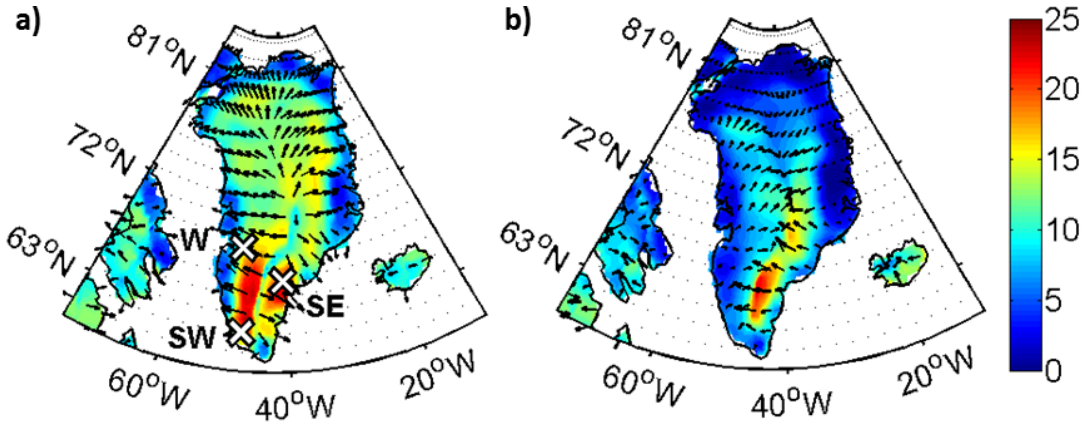

Figure 2-1: The mean of the 2 % fastest downslope (a) and upslope winds (b), based on 34 years in ERA-I. Shown is the wind speed in m s^{-1}. The crosses indicate the locations used for the composites shown in Figure 2-3.

To investigate the influence of the winds on melting over Greenland, I use a melt extent product, derived from brightness temperature by three satellite-borne microwave radiometers: the Scanning Multichannel Microwave Radiometer (SMMR), the Special Sensor Microwave/Imager (SSM/I), and the Special Sensor Microwave Imager/Sounder (SSMIS) [Mote, 2007]. The occurrence of melting is determined from a sharp increase in emissivity of the snow when liquid water is present. The data have a 25 km horizontal resolution with an approximately daily resolution from 1979 to 2012. Several gaps of one day occurred during this period, but they do not affect our results. At each location, there is either melt or no melt, and thus the data does not quantify the amount of melting at that location. More information about this data set is provided in Mote [2007].

2.5 Results

2.5.1 Characteristics of strong wind events across the coast

In order to investigate where high-speed winds across Greenland's coast occur, I use the topographic gradient with a smoothed topography to identify downslope

(and upslope) winds because they tend to be perpendicular to the coastline. Using ERA-I, I find that the strongest cross-coastal winds occur in the south and reach wind speeds above 20 m s^{-1}. In the north, the winds are weaker (Figure 2-1). The north-south differences are likely connected to the North Atlantic storm track south of Greenland [Chang et al., 2002]. Indeed, based on a spectral analysis, I find that the wind speed at weather stations along the southeast and west coast is highly correlated with the pressure on synoptic time scales, and 90 degree out of phase (Figure 2-2), which indicates that the wind has a geostrophic component, supporting connection to cyclones. At the southeast coast, the strong downslope winds are focused within the valley of Ammassalik, which suggests that topographic effects are important too [Bromwich et al., 1996, Oltmanns et al., 2014]. The strongest upslope winds occur across the southeast coast, and they are stronger inland over the ice sheet where the topography is less steep (Figure 2-1). Thus, the dynamical role of the regional topography is likely very different for downslope and upslope winds across the southeast coast.

In the following, I build composites of wind events in southeast Greenland (SE), southwest Greenland (SW) and west Greenland (W) at locations near the coast where the winds are strongest (see Figure 2-1a for locations). The composite of the upslope wind events in southeast Greenland (SE_{up}) is based on the same location as the one for the SE downslope wind events. The results do not change appreciably if nearby regions are chosen. To define the events, I use a threshold on downslope (or upslope) wind speed, such that approximately the same number of wind events is obtained at each location, which is about nine to ten events per year (thresholds and downslope wind directions are given in Table 2.1).

The composites of the strong cross-coastal wind events confirm that they are associated with deep cyclones (Figure 2-3). All wind events reach speeds of $\sim$20 m s^{-1}, which is comparable to the calculated geostrophic velocities associated with the cyclones, indicating that the pressure signal is significant. The location of the cyclone

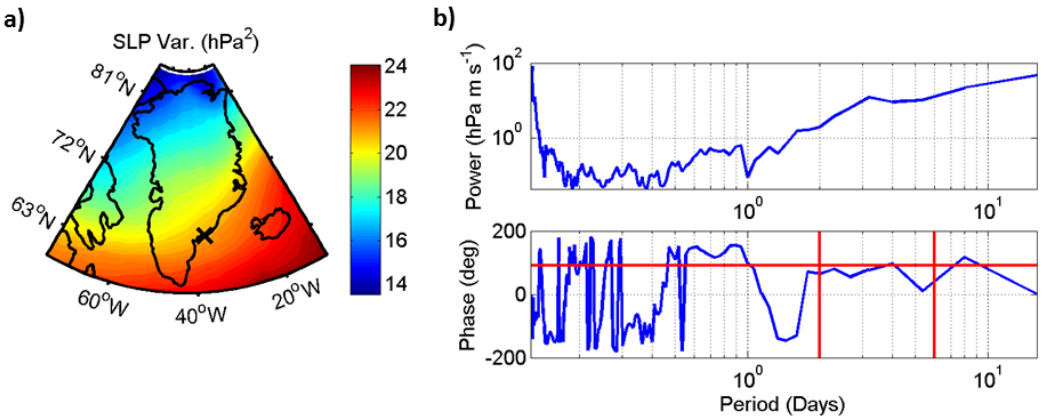

Figure 2-2: (a) Storm track estimated from spectral analysis of SLP in ERA-I. Shown is the SLP variance in the 2- to 6-day period range. The black cross indicates the location of the DMI station whose date is used to calculate the cross-spectrum shown in (b). (b) Cross-spectrum (including the power and the phase) between downslope wind speed and pressure measured by a DMI station at the location shown in (a). The red lines mark the 90 degrees phase shift and the 2- to 6-day period range. A phase shift of 90 degrees is expected for geostrophic winds.

	W	SW	SE	SE_{up}
Threshold on wind speed (m s^{-1})	10.3	11.5	16.5	9.3
Downslope wind direction (degrees eastward from N)	90 (E)	50 (NE)	312 (NW)	312 (NW)
Number of events in 34 years	315	305	315	322

Table 2.1: Definitions of the wind events shown in Figure 2-3. There are approximately 9 to 10 events per year.

either east of Greenland (as in the SE case) or west or southwest of Greenland (as in the SW, W and SE_{up} cases) has a strong influence on the air temperature anomaly over Greenland (Figure 2-3). During SE events, cold air from the north is advected downstream over the warmer ocean. During W, SW and SE_{up} wind events, warm air from the southeast is advected over Greenland. The temperature during wind events along the west coast is up to ∼10 K higher compared to the monthly mean whereas the temperature during wind events at the southeast coast is ∼8 K lower compared to the monthly mean (Figure 2-3). The temperature anomalies are especially pronounced

over the southwest coast. SE wind events are associated with a focused outflow out of the larger scale Ammassalik valley. The influence of the topography on the SW, W and SE_{up} wind events is less pronounced. Weather stations along the coast generally support these results from ERA-I (Figure 2-4). While the obtained wind speed during the events is sensitive to the exact station location, pressure and temperature are not. Thus, all weather stations record a drop in pressure during the wind events. In addition, the stations at the southwest and west coast obtain a warming during SW and W events respectively, while the station at the southeast coast records a cooling during SE events.

Even though I use the term 'upslope' for the SE_{up} wind events, I note that it is unlikely that the southeasterly flow crosses the topography. From radiosonde data over Greenland, I obtain a typical stratification of $N =\sim 0.01$ s^{-1} in winter, and a mean flow of $U =\sim 10$ m s^{-1}. As the height of the southern dome is $H =\sim 2500$ m, I calculate the inverse Froude number defined as $\frac{1}{Fr} = \frac{NH}{U}$ to be $\sim$2.5. According to the flow regime diagram in Smith [1989], and its extension to rotational flows [Ólafsson and Bougeault, 1997], the flow is blocked under these conditions, and the air on the western side of the ice sheet must have descended from upper levels. During the descent, the air warms adiabatically, as typical for Foehn winds [McKnight and Hess, 2000], and this likely contributes to the warming over the west coast [Born and Boecher, 2000].

The relationship between temperature and downslope wind speed not only holds for strong wind events but also for weaker winds, and it can be extended to specific humidity. Thus, downslope wind speed at the west coast is positively correlated with the temperature anomaly and to a lesser extend with the humidity anomaly (relative to the monthly mean), whereas downslope wind speed over the southeast coast is anti-correlated with the temperature and humidity anomaly (Figure 2-5). Since the sensible and latent heat fluxes depend on the temperature and humidity difference between the surface and the air, downslope winds across the southeast coast can cause

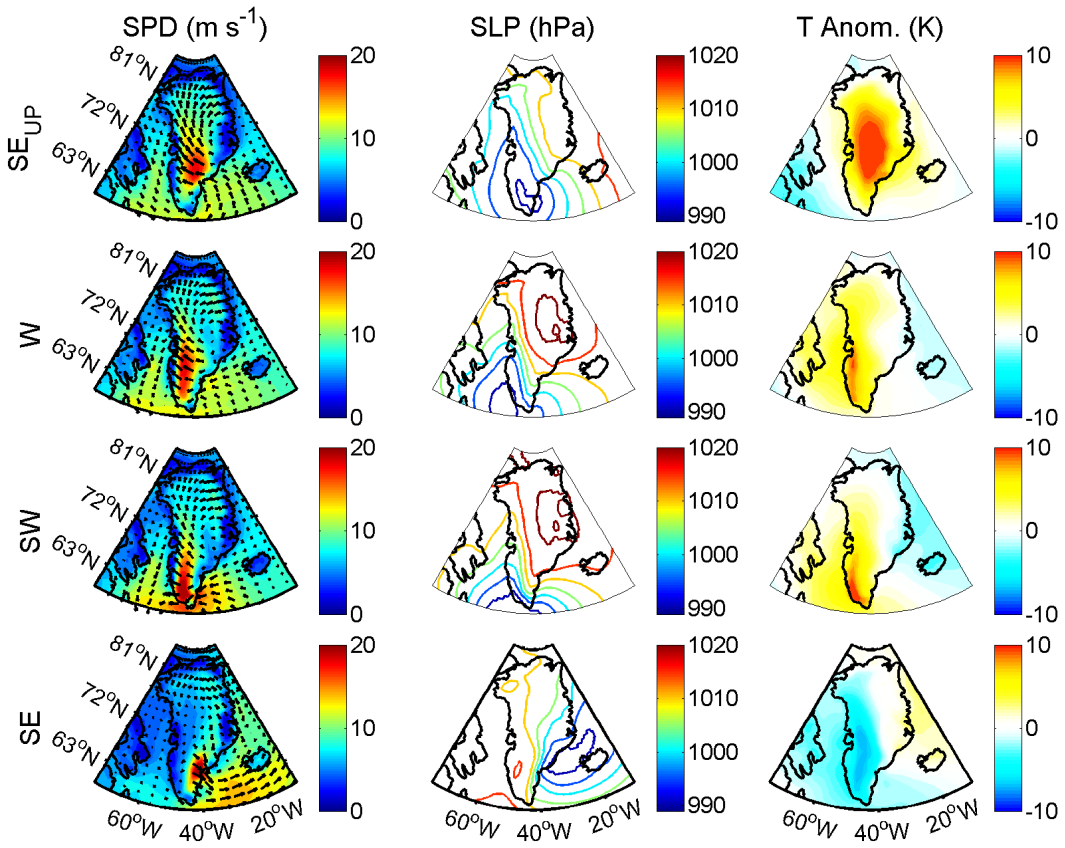

Figure 2-3: ERA-I composites of wind speed, sea level pressure (SLP) and temperature anomaly (relative to the monthly mean) during the high-speed wind events at the locations shown in Figure 2-1. SE_{up} events are based on the same location as SE events. For each location, the composites are based on more than 300 wind events between 1979 and 2012 (see Table 2.1 for definitions).

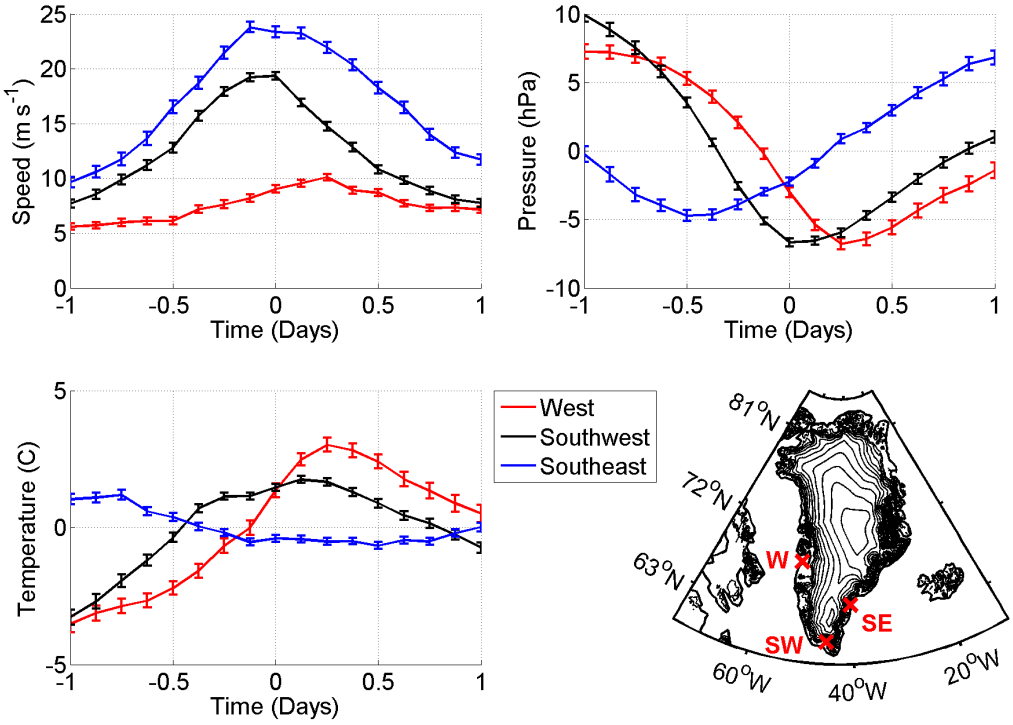

Figure 2-4: DMI weather station composites of wind speed, pressure and temperature evolution of the downslope wind events identified with ERA-I at the locations shown in the map. For pressure and temperature, the mean during the events has been subtracted. The station at the southeast coast is used for the SE events, the station at the southwest coast for the SW events, and the station at the west coast for the W events. In the case of the SE and the SW events, the composites are based on ∼200 wind events. The station at the west coast obtains over 300 W events.

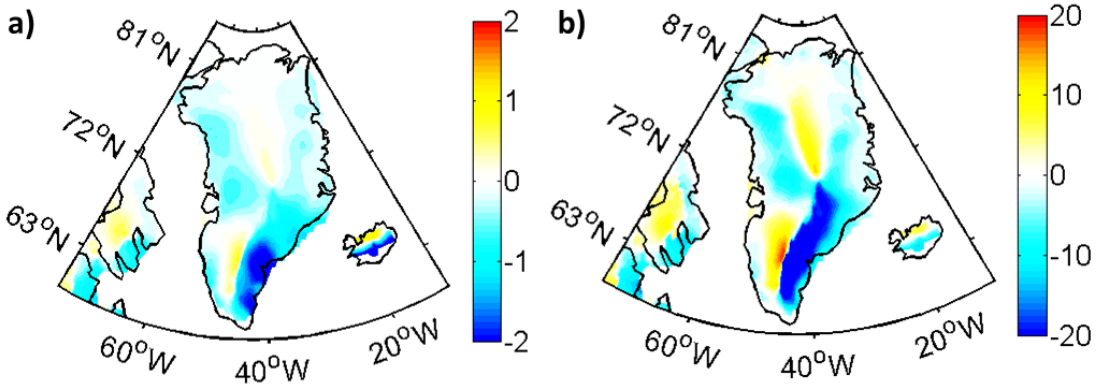

Figure 2-5: (a) Shown is $\overline{u'q'_s}$ between 1979 to 2012, where u is downslope wind speed in m s^{-1} and q_s is specific humidity in g kg^{-1}. The overline indicates a monthly average and the primes denote deviations from the monthly mean. (b) same as (a) but with for temperature (K) instead of humidity. All variables are obtained from ERA-I.

both latent and sensible heat losses over the ocean. The effects on the heat fluxes will be investigated in more detail in Section 2.5.4.

2.5.2 Variability

As the composite of the wind events indicates, W, SW and SE$_{up}$ events are connected. In fact, allowing for a time difference of 2 days 50% of the W events are associated with SW events, 29% of SW events are associated with SE$_{up}$ events, and 41% of the W events are associated with SE$_{up}$ events. Even if events are not followed or preceded by wind wind events at the other locations, ERA-I and weather stations indicate the occurrence of enhanced wind speeds at the other locations. There are fewer connections of each of the west coast wind events with the SE events. Allowing for a time shift of four days, 6% of the SW events, 10% of the W events and 12% of the SE$_{up}$ events are followed by SE wind events. Since SW, W and SE$_{up}$ events are similar with regard to the cyclone location and temperature anomaly, I will focus in the following on the comparison between SE and W wind events only.

The interannual distribution of SE and W events suggests a weak anti-correlation

as years with many SE events tend to be associated with fewer W events and vice versa ($r = -0.4$ in winter; the anti-correlation is significant to the 95% confidence interval, determined by testing the null hypothesis). In some years, SE and W events are similarly frequent (Figure 2-6). While the number of wind events obtained is sensitive to the threshold on wind speed, the seasonal and inter-annual distributions are not. Both types of wind events have a large inter-annual variability with the number of events per year varying between 4 and 17. While the distribution of W events clearly peaks in winter, SE events are also frequent in fall and spring (Figure 2-6). The cyclone that triggers SE events is farther north (and north of the mean jet stream location in winter). Such a northward position is likely facilitated by the reduced stability over land in fall and spring, when solar insolation and surface heating is larger. This will be investigated in more detail in the next section.

2.5.3 Large-scale dynamics

Large-scale atmospheric forcing

To understand what causes the wind events, I start by investigating their large-scale evolution. Composites of equivalent potential temperature at the tropopause during the evolution of SE and W events show that a cold temperature anomaly (which is representative of a positive PV anomaly [Hoskins et al., 1985]) is present over Greenland during SE events and over the Labrador Sea during W events (Figures 2-7 and 2-8). An upper level PV anomaly was also found to be influential for the evolution of the cyclone in case studies on intense lee cyclones east of Greenland [Kristjánsson et al., 1999, Skeie et al., 2006], and in case studies on bifurcation around the southern tip of Greenland [Moore and Vachon, 2002, Kurz, 2004]. Simultaneously, warm air at the surface is advected northward over the Irminger Sea in the case of SE events, and over the Labrador Sea in the case of W events (shown by the meridional stretching of surface isentropes at 0 hours in Figures 2-7 and 2-8). Especially for the W events, the surface temperature contours are well aligned with the upper level temperature

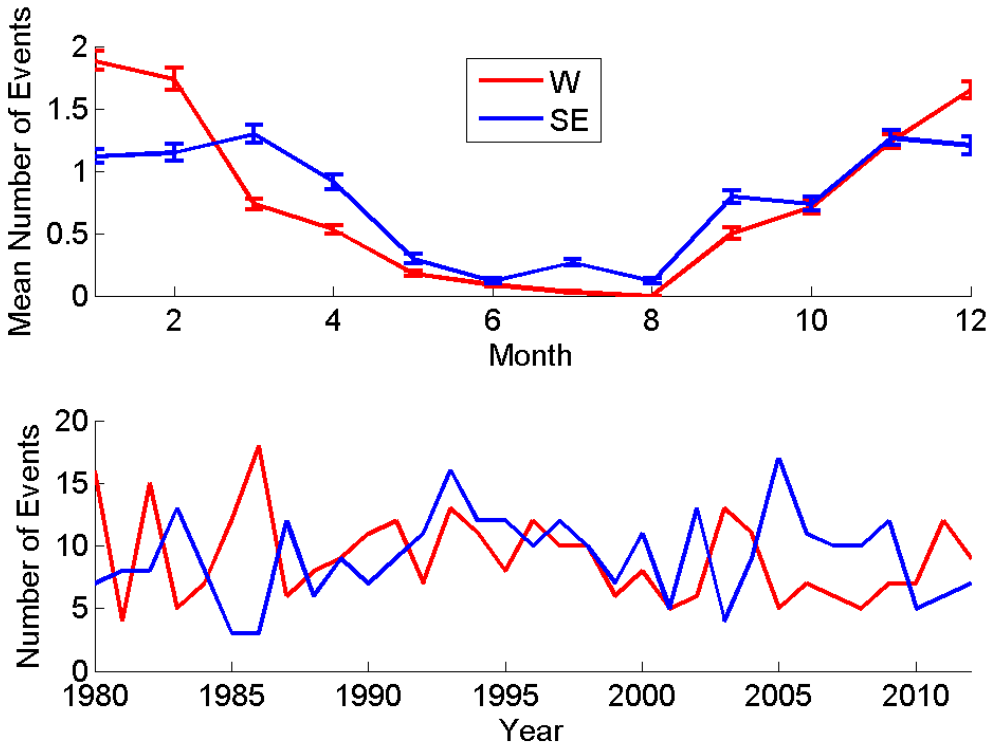

Figure 2-6: Seasonal and interannual variability of SE and W wind events. W event occurrence peaks in winter whereas SE events are also frequent in fall and spring. Error bars indicate the standard error of the mean. Both types of wind events have a large inter-annual variability. For the interannual variability, a year has been defined to extend from July to the following June, so as not to split the winters.

contours in the region of the Rossby wave breaking – where colder isotherms at the tropopause are southward of warmer ones. This indicates that the wind events intensify through baroclinic instability.

In order to investigate whether both anomalies (at the surface and the tropopause) contribute to the instability and the Rossby wave breaking, I estimate the penetration depth H of the anomalies with $H = \frac{fL}{N} = 10$ km, where I have used a characteristic length scale of $L = 1000$ km, a typical stratification of $N = 0.01$ s^{-1} and a Coriolis parameter of $f = 10^{-4}$ s^{-1}. Thus, the velocity at the height of the tropopause $z_t =\sim 9$ km, induced by the surface temperature anomaly, can be estimated with $-H\frac{\partial v}{\partial z}\exp\left(\frac{-z_t}{H}\right)$, where $\frac{\partial v}{\partial z}$ is obtained from thermal wind balance. For both types of wind events, low level temperature anomalies (relative to the monthly mean) suggest a temperature difference of 5 K over 1000 km (on a constant pressure surface), which corresponds to a velocity perturbation of 7 to 8 m s^{-1} at the tropopause. Since the basic state (i.e. the monthly mean temperature distribution) is itself not completely balanced, the background flow associated with the large temperature contrast across Greenland's east coast likely also influences the upper level anomaly, especially during SE events. From the temperature evolution at the tropopause, I estimate an advective velocity of 500 km over 12 hours (Figure 2-8), which is equivalent to 11 to 12 m s^{-1}. Since this velocity is of the same order of magnitude as that estimated from the surface anomalies, the results suggest that the surface anomalies indeed contribute to augmenting the upper level anomalies, and that both types of wind events intensify through baroclinic instability.

The large-scale evolution of the cyclones provides a potential explanation why SE events are more frequent in fall and spring compared to W events (Figure 2-6). During SE events, cyclones are present east of Greenland (Figure 2-7), and during W events cyclones intensify over the Labrador Sea (Figure 2-8). Thus, the PV anomaly responsible for SE events moves over land, while the one responsible for W events moves over the ocean. The surface temperature west and northwest of Greenland

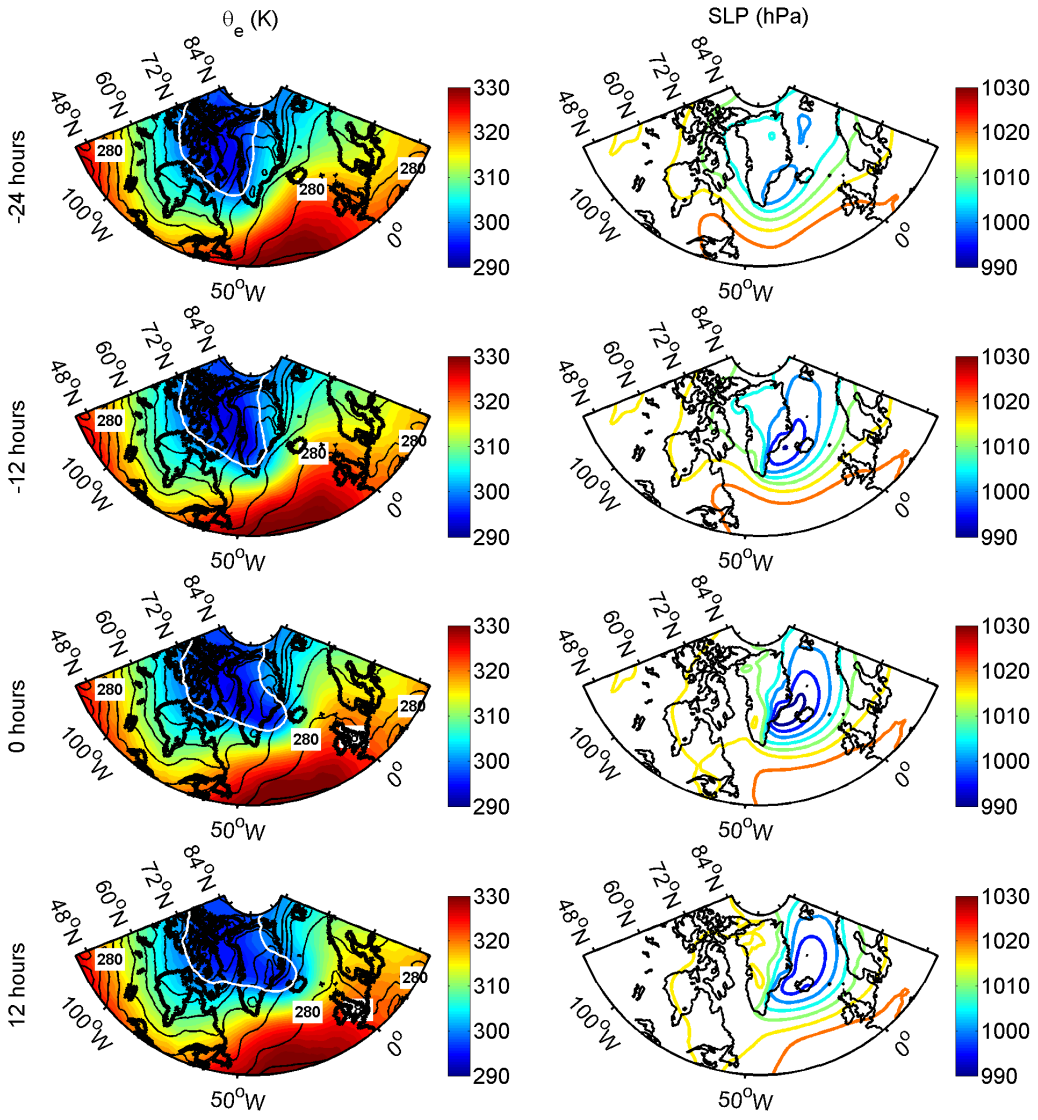

Figure 2-7: Left: Composite evolution of equivalent potential temperature θ_e at the tropopause (shading), defined as the 2 PVU (potential vorticity units) surface, and at the surface (contours) during SE events. The white line marks the location of the 300 K isotherm at the tropopause to show the breaking of the Rossby wave. The contour interval of equivalent potential temperature at the surface is 5 K. Right: Composite evolution of SLP during SE events. The composites are based on 315 events between 1979 and 2012.

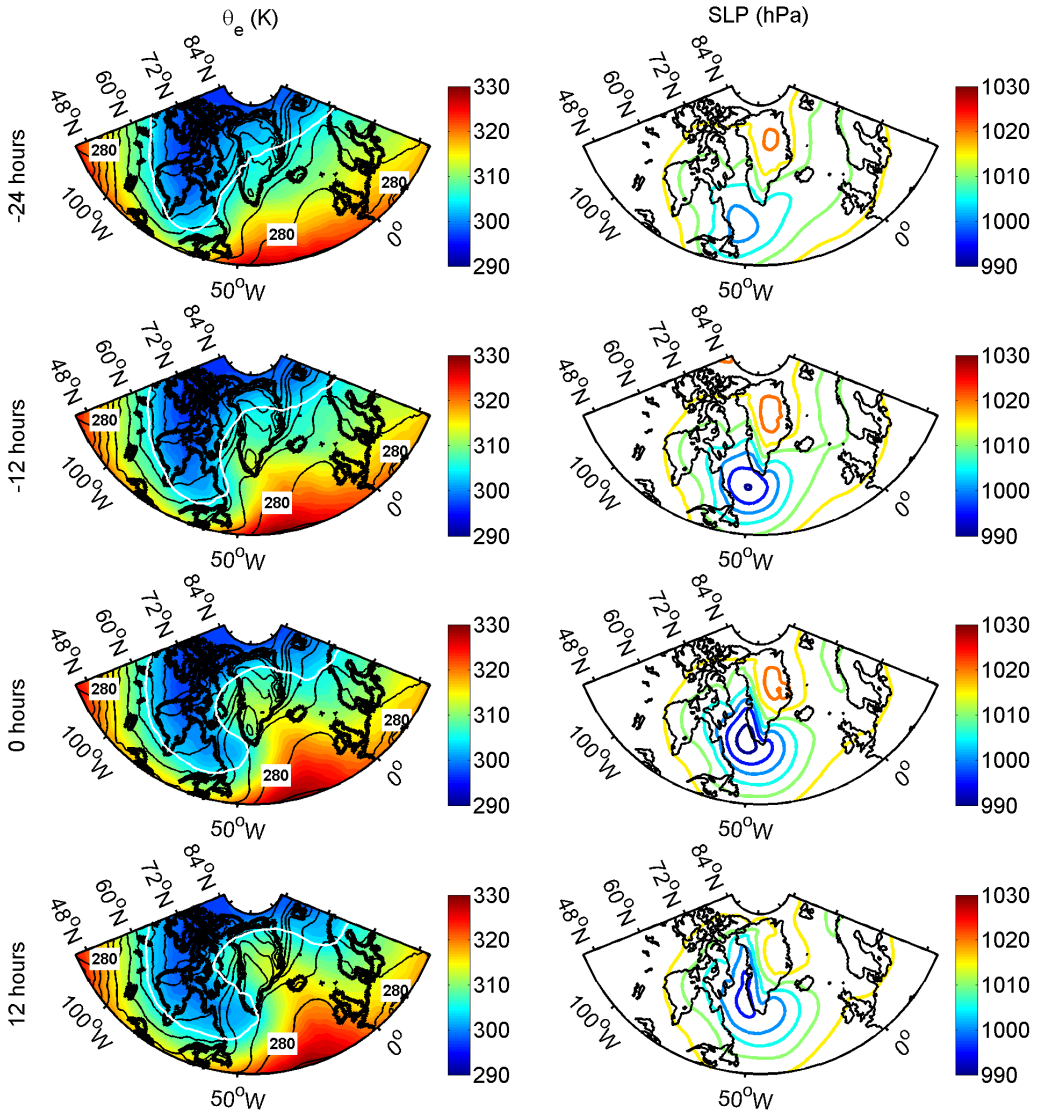

Figure 2-8: Left: Composite evolution of equivalent potential temperature θ_e at the tropopause (shading), defined as the 2 PVU surface, and at the surface (contours) during W events. The white line marks the location of the 305 K isotherm at the tropopause to show the breaking of the Rossby wave. The contour interval of equivalent potential temperature at the surface is 5 K. Right: Composite evolution of SLP during W events. The composites are based on 315 events between 1979 and 2012.

varies by up to 20 °C between fall or spring and winter. Over the ocean southwest of Greenland, it varies by less than 5 °C, and radiosonde profiles suggest that the warmer surface in fall and spring can result in a reduced stability west and northwest of Greenland. The reduced stability, in turn, leads to a deeper penetration of the upper level PV anomaly and helps cyclones to spin up [Moore et al., 1996]. This can explain why SE events are more frequent in fall and spring compared to W events.

When an upper-level PV anomaly crosses high topography, a secondary lee cyclone can form southward at the surface, propagate northward along the coast and superpose with the primary anomaly. The presence of either two separate pressure minima or a very large low pressure anomaly during SE events is supported by weather station Summit and by several stations along the east coast of Greenland (Figure 2-9). As the low pressure anomaly crosses the ice sheet, the wind direction and the temperature change. Simultaneously, a pressure drop is recorded at several locations along the east coast, indicating that a secondary lee cyclone is propagating along the coast. The pressure and temperature evolution over the ice sheet during W events is opposite to that of SE events since the cyclone is on the other side of the coast. Thus, station Summit confirms that the atmospheric setting on top of the ice sheet is affected by both types of wind events, even though the high topography usually represents a barrier to the mean flow associated with an anticyclonic circulation over Greenland.

Topographic forcing

Previous studies have suggested that the high elevation of Greenland plays an important role for the formation and deepening rate of cyclones [Kristjánsson and McInnes, 1999, Skeie et al., 2006, Tsukernik et al., 2007, Kristjánsson et al., 2009]. The influence of high topography on the atmospheric circulation can be described with the topographic Rossby wave model. Following Charney and Eliassen [1949], I use the barotropic vorticity equation $\frac{D_h}{Dt}\left(\frac{\zeta_g+f}{h}\right)=0$, where f is the Coriolis parameter, h

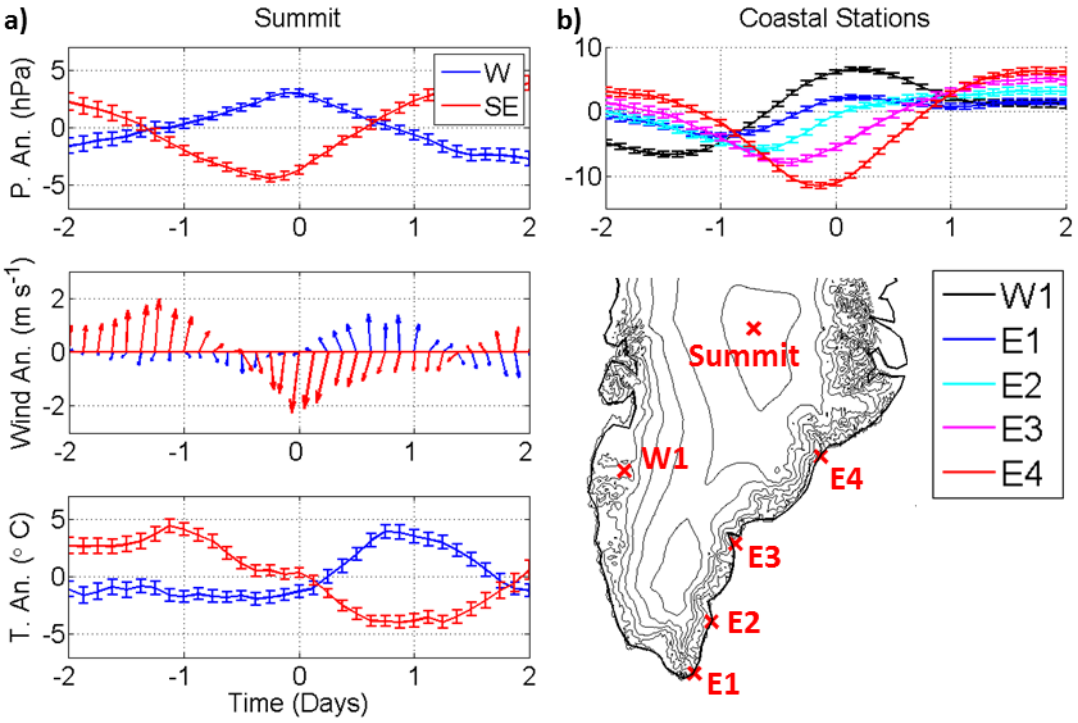

Figure 2-9: (a) Composite evolution of pressure, wind direction and temperature at the GCNet station Summit over the ice sheet during SE and W wind events. (b) Pressure evolution recorded by DMI weather stations along the east coast (shown on the map) during SE events. The Summit station composites are based on approximately 100 events between 1997 and 2010 for each type of event. The SLP composite with the coastal DMI stations is based on more than 200 events for all stations with most stations recording more than 300 of the wind events since 1979. In each case, the error bars represent the standard error of the mean.

is the depth of the fluid, ζ_g is geostrophic vorticity and $\frac{D_h}{Dt}$ is the derivative following horizontal motion. I also assume that the upper boundary is at a fixed height H, and the lower boundary at variable height $h_T(x,y)$, where $|h_T| \ll H$ and $|\zeta_g| \ll f_0$. After linearizing the barotropic vorticity equation, applying the mid-latitude β-plane approximation, and including a linear damping of the relative vorticity $\frac{\zeta_g}{\tau_e}$ (where τ_e represents the spin-down time-scale for synoptic systems), this yields [Holton and Hakim, 2013]:

$$\left(\frac{\partial}{\partial t} + \overline{u}\frac{\partial}{\partial x}\right)\zeta_g + \beta v + \frac{\zeta_g}{\tau_e} = -\frac{f_0}{H}\overline{u}\frac{\partial h_T}{\partial x}, \tag{2.3}$$

where $\overline{u}$ is the mean westerly flow. Next, I represent the geostrophic wind and the vorticity in terms of the perturbation streamfunction Ψ and approximate the smoothed topography with a Fourier series $h_T(x,y) = \sum_k \sum_l \hat{h}_{k,l} \exp(ikx + ily)$, where $\hat{h}_{k,l}$ are the Fourier coefficients. This has as steady-state solution [Charney and Eliassen, 1949, Holton and Hakim, 2013]:

$$\hat{\Psi}_{k,l} = f_0 \hat{h}_{k,l} / \left[H\left(K^2 - K_S^2 - i\varepsilon\right)\right], \tag{2.4}$$

where $K^2 = k^2 + l^2$ is the total horizontal wave number squared, $K_S^2 = \frac{\beta}{\overline{u}}$ represents the wave number of the the free stationary Rossby wave mode and $\varepsilon = \frac{1}{\tau_e}\frac{K^2}{k\overline{u}}$ [Holton and Hakim, 2013]. By Fourier inversion, Equation 2.4 can be solved for the streamfunction. Thus, the amplitude of the wave is particularly large when its scale matches that of the free stationary Rossby wave mode. In this case, it is phase-shifted by one quarter wavelength relative to the mountain crest, consistent with Figures 2-7 and 2-8.

To apply the topographic Rossby wave model to Greenland, I use a mean westerly flow of 10 m s^{-1}, a mean tropopause height H of 8 km and a frictional spin-down time of 1 day which is a typical time scale for both types of wind events (e.g. Figures 2-7, 2-8 or 2-9). Using a mean westerly flow of 15 m s^{-1} or a frictional time scale

of 2 days does not change the results appreciably. Here, I use a frictional time scale of 1 day with regard to the constraint that the cyclones be stationary during this time. The model is simplified as it neglects surface heating and cooling. In addition, the long meridional extent of Greenland questions the validity of using a constant mean westerly flow. Despite the simplicity of the model and these shortcomings when applying it to Greenland, the results indicate that it does reproduce a basic southwest - northeast asymmetry over the southeast coast which is similar to the composite of the western and eastern wind events (compare Figures 2-3 and 2-10d). I note that the asymmetry is not 'perfect' as W and SE events are not exact mirror images of each other. In addition to representing different phases of the topographic Rossby wave, they also have a different orientation as the southwest - northeast direction is more pronounced for W events. The direction or phase of the Rossby wave is likely dictated by the meandering jet stream (i.e. the mean flow) and the location of the PV anomalies [Woollings et al., 2008, 2010, Hannachi et al., 2012].

The topographic Rossby wave model is based on an idealized mean westerly flow and reproduces stationary wave modes. As the westerly flow across Greenland, or similarly the path of the jet stream, is highly variable, the occurrence of these wind events is determined by the large-scale atmospheric variability. Specifically, the results from the previous section suggest that an upper level potential vorticity anomaly could superpose on the topographic Rossby wave, and thereby create deep cyclones and strong wind events. Thus, while the topography influences the location of the synoptic disturbance, the variability of the events is determined by the large-scale atmospheric variability.

To investigate if there is a large-scale atmospheric mode that describes which phase of the topographic Rossby wave is dominant at any given time, I use an empirical orthogonal function (EOF) analysis of daily SLP variability from 1979 to 2012 (for the full years) in ERA-I. (Figure 2-10). The first EOF mode that is obtained is connected to the strength of the Icelandic Low and highly correlated with the North

Atlantic Oscillation (NAO) [Hurrell, 1995]. The second mode reflects the strength of a low pressure anomaly over the Labrador Sea with opposite phases over the eastern and western North Atlantic. It is similar to the Greenland-Scandinavian dipole (e.g. Tsukernik et al. [2010]) and the 'blocking' regime described by Cassou et al. [2004] and Hurrell and Deser [2010]. The third EOF mode resembles the ridge regime in Cassou et al. [2004]. It is also connected to the Greenland blocking as defined by Scherrer et al. [2006] and a northern jet stream location [Woollings et al., 2008, 2010, Hannachi et al., 2012], which is in turn associated with a negative phase of the East Atlantic pattern [Barnston and Livezey, 1987]. This EOF mode shows similarity with the stationary topographic Rossby wave pattern over the southeast Greenland coast, the region of interest in this study. Specifically, in both cases the zero line runs across the southern dome of Greenland where the topography is higher compared to the surrounding area. This emphasizes the role of the topography in directing the cyclone either south or north of the top of the southern dome. The results of this EOF analysis are insensitive to the size of the domain, as long as Greenland is included, and to the time period chosen. Thus, the EOF mode associated with the zero line across southeast Greenland is obtained for all seasons, including summer, even though its amplitude is much reduced in summer.

The southwest - northeast asymmetry of the third EOF mode is also similar to that associated with the eastern and western wind events (Figure 2-10c and Figures 2-7 and 2-8). Specifically, isolines of this mode cross the southeast coast, indicating a geostrophic flow across the coast. Indeed, I find that the winter (DJFM) occurrence of SE (W) events is correlated with the principal component of the third EOF mode with a correlation coefficient of -0.70 (0.50), despite explaining only 13% of the total SLP variance over Greenland. In both cases, the correlation is significant to the 95% interval (determined by testing the null hypothesis). W events are also affected by the second EOF mode, whereas SE events are also affected by the first EOF mode. In addition, the third EOF mode reproduces the seasonality of the wind events in that

seasonal averages of its principal component (PC_3 hereafter) are smaller in spring and fall compared to winter, and a smaller (larger) PC_3 favors the occurrence of SE (W) events. Thus, in the following, I will use the PC_3 to approximate the strength of winds across Greenland's southeast coast, as it is a more quantitative index especially during time periods when the wind events are less frequent, such as summer. Even so, it should be kept in mind that it is not the only mode affecting the strength of these winds as the first two EOFs (which reflect the general strength of atmospheric variability southeast and southwest of Greenland) are also influential.

2.5.4 Downstream effects

Influence of cross-coastal flows on the heat fluxes over the ice sheet and ocean

When the flow across the southeast coast is northwesterly (and the PC_3 is negative), it can be associated with an SE event and drive large heat fluxes over the Irminger Sea [Oltmanns et al., 2014]. I find that prior to the 312 most negative PC_3 events (i.e. the 312 times when the PC_3 is most negative between 1979 and 2012, which had to be separated by at least three days), a geostrophic flow is directed off the Canadian Archipelago across the Labrador Sea, and after these events there is a strengthened northwesterly flow from the Arctic over the Greenland Sea (Figure 2-11). Both flows are connected with the same cyclone. When the winds are directed off the Canadian Archipelago, tip jet events can occur in addition, which are known to drive large heat fluxes over the Irminger Sea [Pickart et al., 2003a, Våge et al., 2011]. The strengthened northerly flow over the Greenland Sea after the PC_3 events is likely associated with enhanced heat fluxes in this region. Thus, by describing the variability of the flow across Greenland's SE coast and generally the flow across the horizontal temperature gradient associated with the Arctic border (also west and north of southeast Greenland), the variability of the third EOF mode is well correlated with the heat fluxes over the Greenland, Irminger and Labrador Sea regions

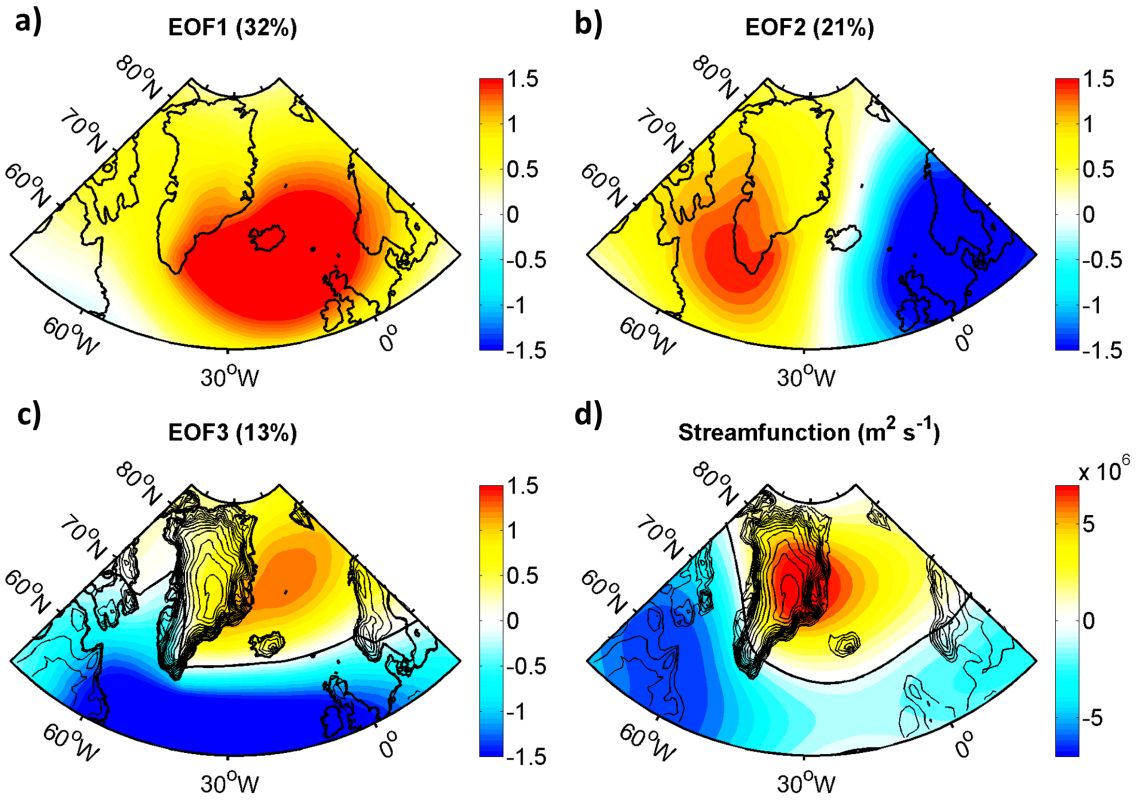

Figure 2-10: (a,b,c) EOF decomposition in ERA-I based on SLP variability from 1979 to 2012. The modes are normalized by their standard deviation, and the title indicates the percentage of the atmospheric variance that is explained by them. Topographic contours are added for the third EOF mode. The black line indicates the zero line of the third EOF mode. It runs across the top of the southern dome of Greenland. If the cyclone is north of that line, the flow across the southeast coast is northwesterly. If it is south, the flow is southeasterly. (d) Perturbation streamfunction (m^2 s^{-2}) derived from the topographic Rossby wave model. Despite its simplicity, the model reproduces a basic southwest-northeast asymmetry over the southeast coast, that is similar to that associated with the third EOF mode and the eastern and western wind events.

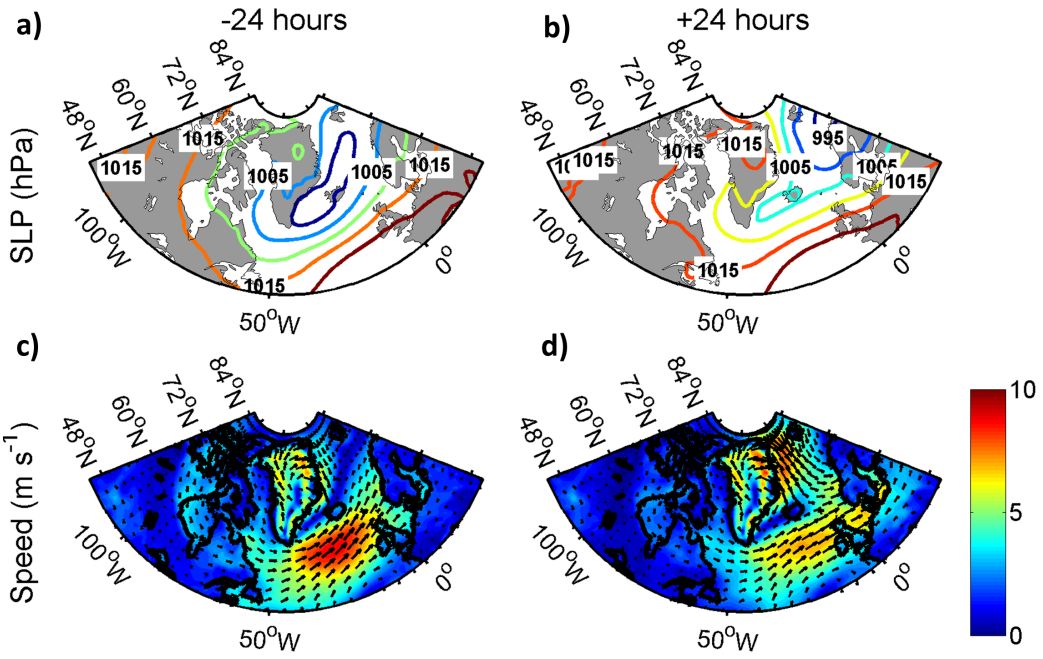

Figure 2-11: Composite evolution of the 312 most negative PC_3 times between 1979 and 2012 in ERA-I. PC_3 refers to the principal component of the third EOF mode (Figure 2-10). Shown are the wind speed and sea level pressure field 24 hours before and after the time when the PC_3 is at its minimum.

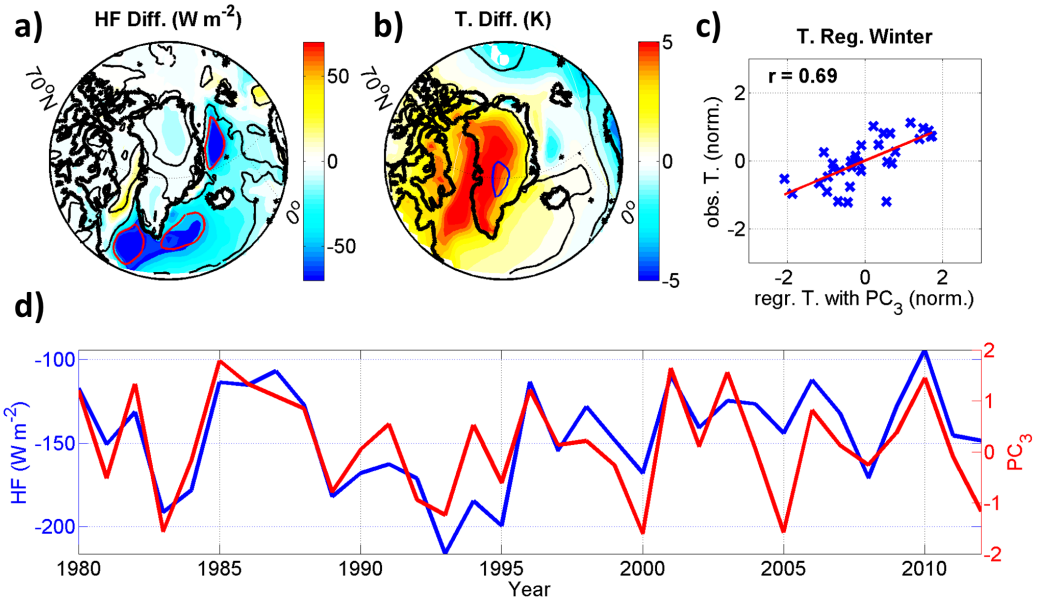

Figure 2-12: (a) Composite difference of the heat flux field (W m^{-2}) between the eight lowest and the eight highest PC_3 winters (DJFM) from 1979 to 2012 where PC_3 refers to the principal component of the third EOF mode (Figure 2-10). The thin black line delineates the regions in which the heat flux difference exceeds the two standard errors associated with the eight highest and the eight lowest PC_3 winters. Negative heat fluxes indicate a heat flux from the surface to the atmosphere. (b) Composite difference of the surface air temperature (K) between the eight highest and the eight lowest PC_3 winters (DJFM) from 1979 to 2012. The blue line delineates the region on which the temperature regression is based. (c) Regression of temperature variability within the region shown in (b) in winter (DJFM) using the PC_3. (d) Inter-annual variability of the mean winter (DJFM) heat fluxes averaged over the Irminger, Labrador and Greenland Sea regions shown in (a) and the (normalized) PC_3.

in winter (DJFM) with a Pearson correlation coefficient of 0.75 (Figure 2-12d). The correlation between the heat fluxes and the PC_3 is significant to the 95% confidence interval. This indicates that strong northwesterly flows across the Arctic border do indeed force heat losses over the ocean convection regions around Greenland.

In the other direction, winds across the southeast coast advect warm air over the ice sheet. As the winds are generally strongest in winter, I expect the turbulent heat fluxes to be largest in winter. Indeed, the correlation between temperature over the ice sheet (which is a more quantitative index than melt extent), and the PC_3 (again

used to approximate the flow across the southeast coast) is $r = 0.69$ in winter (Figure 2-12c). In spring and summer, indirect effects of the atmospheric circulation, related to changes in the albedo and radiation become more important (Figure 2-13c). I find that the correlation of $r = 0.52$ in spring (March through June) is reduced compared to winter (December through March), but it remains significant to the 95% interval. For both seasons I have removed a linear trend from the temperature data. Next, I will investigate the influences of warm winds on the heat balance of the ice sheet. I will start by studying how much anomalous heat can be conducted into deeper layers of the ice sheet during warm winters with frequent and strong onshore winds. Then I will investigate the more generally the atmospheric causes of melting.

Winter heat storage in the ice sheet

In theory, the heat that is transferred through the sensible heat fluxes during winter can be conducted into deeper layers of the snow, which could precondition melting in spring (Equation 2.2). To investigate how much additional heat is stored in the snow in winters when the PC_3 is predominantly positive (and when the flow over south Greenland is mostly southeasterly), I use the one dimensional heat equation $\frac{\partial T}{\partial t} = \alpha \frac{\partial^2 T}{\partial z^2}$, where z is the depth below the surface, T is the snow temperature and t is time. α is defined as $\frac{k}{\rho_{sn} c_{sn}}$, where k is the conductivity of the snow, c_{sn} is the specific heat capacity of snow ($c_{sn} = 2009$ J kg^{-1} K^{-1} [Hock, 2005]), and ρ_{sn} is snow density. Thus, α is a function of depth. Sturm et al. [2010] have used a set of 25,688 snow depth and density measurements for different snow types to derive an empirical relationship between snow depth and density, and based on 488 samples, Sturm et al. [1997] derive an empirical relationship between snow conductivity and snow density. Both relationships have been tested, and the accuracy of the conductivity-density relationship is $\pm 10\%$. The relative error associated with the depth-density relationship is estimated to be less than 0.5%. Thus, I use these relationships to estimate the snow conductivity and density as a function of depth, and solve the heat equation.

Specifically, I model the temperature difference of the snow between the eight most positive and the eight most negative PC_3 winters. I define x on the interval from 0 to D, where D is the total snow depth (which I chose to be 10 m to be well below the penetration depth of seasonal temperature variability). Since the winter (DJFM) mean surface temperature difference between these winters is 5 K (Figure 2-12b), I set 5 K as upper boundary condition. The temperature difference of 5 K between these winters does not need to be the result of warm winds only. Other terms in the surface energy budget, in particular reduced outgoing longwave radiation associated with enhanced cloud cover or atmospheric humidity, can also contribute to the anomalous surface temperature. As initial condition, I set the snow temperature difference to 0 K everywhere. Next, I integrate over the entire winter from December through March and calculate the final heat content $H(t) = \int_D^0 c_{sn}\rho_{sn}Tdz$.

The empirical relationships for snow density and conductivity are based on parameters that vary according to the type of snow considered. Snow types (e.g. 'prairie' or 'alpine') are classified according to properties such as temperature, liquid water and ice content, grain size and texture [Sturm et al., 1995]. 'Maritime' characterizes the most maritime snow class, whereas 'Tundra' corresponds to the most continental snow class. Depending on which snow class I use, the final heat content difference between the warm and the cold winters ranges between $4.5 \cdot 10^6$ J m^{-2} for 'Tundra' and $5.1 \cdot 10^6$ J m^{-2} for 'Maritime' (Figure 2-13). Results from the other snow classes fall within these two. To put this into perspective: The mean total heat flux across the surface over the most part of the ice sheet (obtained from ERA-I) is $\sim$3 W m^{-2} in April (Figure 2-13). Under these conditions, it takes 17 to 20 days to obtain an equivalent amount of energy. Thus, the model suggests that the additional heat stored in the ice sheet during the eight most positive PC_3 winters compared to the eight most negative PC_3 winters can result in an earlier onset of the melt season by 17 to 20 days. I note that there is a large uncertainty associated with the radiative heat fluxes in ERA-I [Chaudhuri et al., 2014], despite the fact that ERA-I is one of the better

performers when different reanalyses are compared [Walsh et al., 2009]. Thus, the time period of 17 to 20 days should be considered as an estimate only.

Melt events

Since most of the melting occurs in summer when the winds are weak, I investigate the atmospheric causes of sudden melt events instead of analyzing the effect of strong onshore winds on melting. Specifically, I use satellite data with a daily resolution [Mote, 2007] to build a composite of melt events which I define using a threshold of 2.2 standard deviations above the running mean with a period of 15 days. The standard deviation is taken over the same period as the running mean. In addition, events have to be separated by at least two days. This results in 304 melt events between 1979 and 2012 (Figure 2-14), and thus the frequency of the events is comparable to that of the wind events. If different averaging periods are chosen the results do not change. The results are also insensitive to the region on which the definition is based such that melting at only the east coast or the west coast results in similar atmospheric settings. The melt events I obtain mostly occur in fall, winter and spring, and are least frequent in summer. They are associated with a temperature anomaly of 10 K over the ice sheet (relative to the monthly mean), with a cyclone southwest of Greenland and an anticyclone northeast of Greenland, as well as with a southeasterly flow across the southeast coast (Figure 2-14). Since the melt extent data is daily and the reanalysis data is 6-hourly, I use the time step within the day at which the temperature over the ice sheet is maximum for the atmospheric composite, as temperature is likely the most relevant quantity for melting. Most of the anomalous melt occurs along the coast in southern Greenland. The atmospheric setting resembles that during SE_{up} events (and to a lesser extent W and SW events) but with reduced amplitude, indicating that the turbulent heat fluxes induced by strong upslope flows across the southeast coast are not the only factor contributing to the melting.

In order to investigate which terms of the surface energy budget contribute to

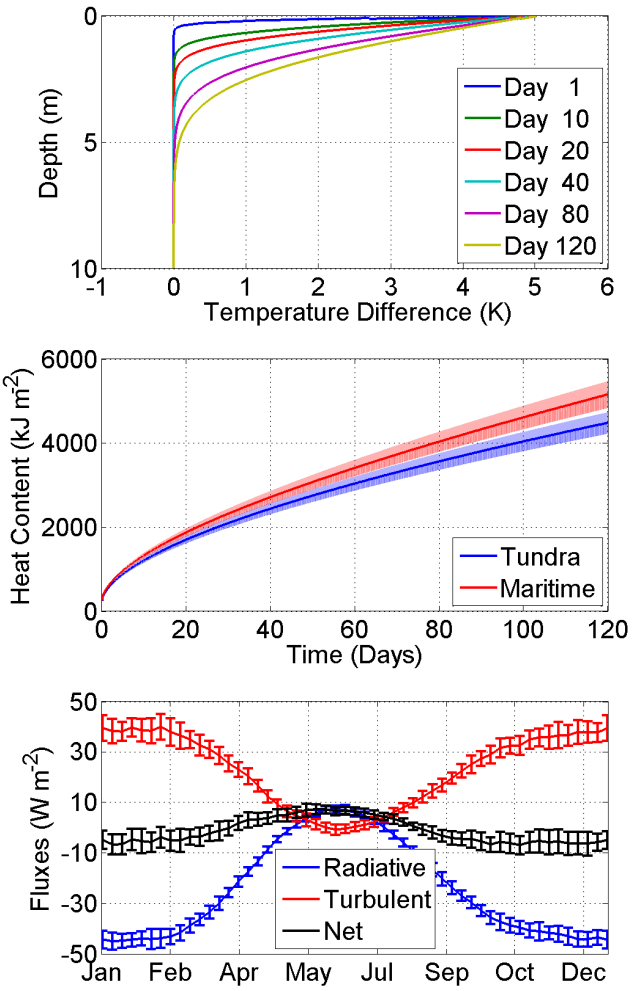

Figure 2-13: (a) Evolution of the snow temperature difference between the eight most positive and the eight most negative PC_3 winters using the heat equation with snow density estimates for the class 'Tundra' in Sturm et al. [2010]. (b) Additional heat content in the eight most positive PC_3 winters relative to the eight most negative PC_3 winters for the snow classes 'Tundra' and 'Maritime', which represent the most continental and the most maritime snow class respectively. The error bars are based on the estimated accuracy of the snow conductivity and density obtained from empirical relationships. (c) Mean seasonal evolution of the ERA-I heat fluxes, averaged over the most part of the ice sheet.

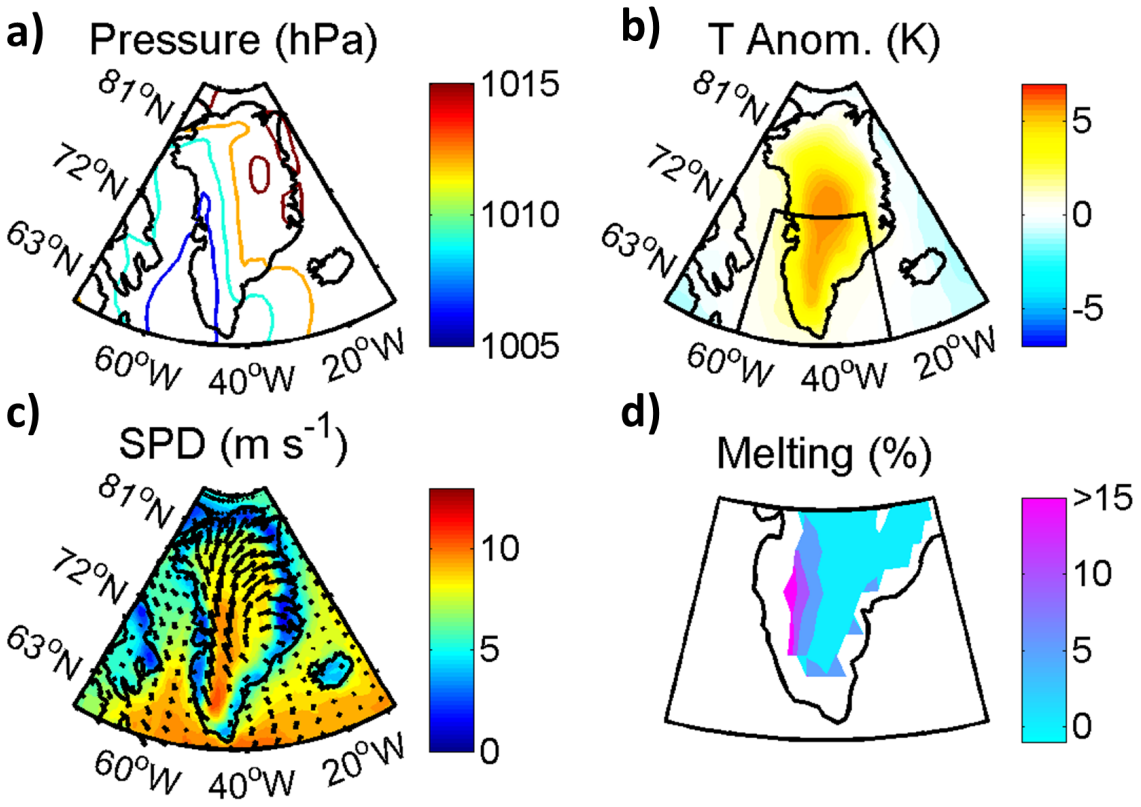

Figure 2-14: (a,b,c) ERA-I composite of the atmospheric setting during 304 melt events between 1979 and 2012, defined as the time when the total melting over the ice sheet exceeds 2.2 running standard deviations above the running mean. Melt events are associated with a warm temperature anomaly (relative to the monthly mean), a cyclone southwest of Greenland, and a southeasterly flow across the southeast coast. (d) Melt extent anomaly (relative to a 15 day running mean), as derived from brightness temperature obtained by satellites [Mote, 2007], within the box shown in c. A melt anomaly of 100% indicates that all of the obtained events at that grid location are associated with anomalous melt, whereas 0% means that no event is associated with anomalous melt at that location. The melt anomaly is largest along the coast in southern Greenland.

the melting, I use atmospheric weather stations over the ice sheet. A composite of temperature during melt events at several weather stations confirms the widespread warming over the ice sheet during melt events (Figure 2-15). The warming is largest at the west coast and over the central ice sheet, and less pronounced at the east coast, likely because of the proximity to the ocean and because the winds are southeasterly. Also, the warming occurs first over the west coast and then over the east coast. Between the two domes of Greenland, station Saddle, which obtains more than 100 melt events, records both an increase in wind speed (with winds coming from the east-southeast) and an increase in absorbed radiation during the melt events, and in theory both of these factors can contribute to the warming (Figure 2-15).

The increase in radiation, in turn, can be due to enhanced absorbed shortwave radiation when the melting lowers the albedo, or it can be due to reduced outgoing longwave radiation when there is an increased cloud cover or atmospheric humidity. Weather stations in Nuuk at the west coast and in Tasiilaq at the east coast observe both a decrease of the albedo of $\sim$0.1 and an increase in cloud cover of $\sim$20% (Figure 2-16) which results in reduced outgoing longwave radiation. There is also a reduction of absorbed shortwave radiation due to the cloud cover, but this reduction is not as large as that of outgoing longwave radiation, which could be due to the decrease in the albedo, such that a larger fraction of the incoming shortwave radiation is absorbed. At the weather station in NUK, for instance, I calculate that the smaller albedo results in an additional 9 W m^{-2} of absorbed shortwave radiation. Thus, the warming over the ice sheet is likely the result of several factors: There is advection of warm air by southeasterly winds. The increased cloud cover (or atmospheric humidity) retains much of the anomalous heat, and especially near the coast, the warming affects the albedo of the snow, which results in more absorbed shortwave radiation.

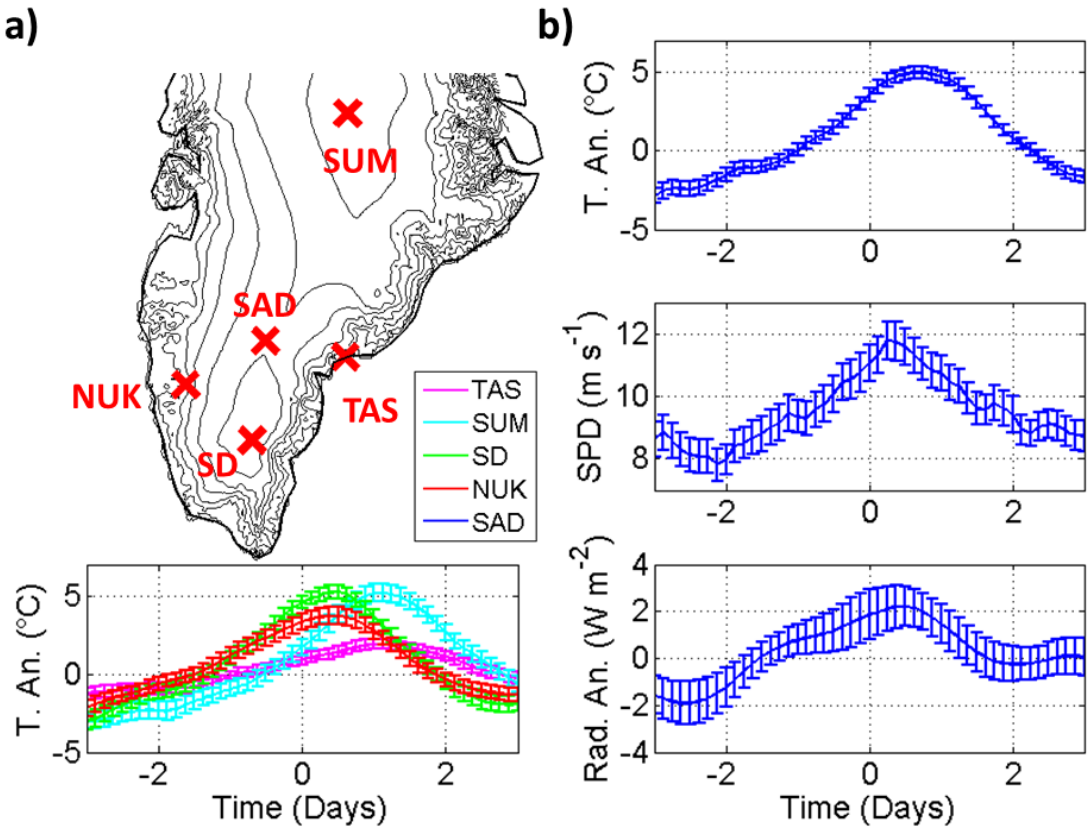

Figure 2-15: (a) Composite of temperature evolution during the melt events at several locations over southern and central Greenland (with the mean temperature during the events subtracted). The composites with the GCNet stations Saddle (Sad), South Dome (SD), and Summit (SUM) are based on more than a 100 melt events. The composites with the PROMICE stations in Nuuk (NUK) and Tasiilaq (TAS) are based on ∼60 melt events. (b) Composites of temperature, wind speed and radiation evolution during the melt events with the Saddle weather station. For temperature and radiation the mean during the events is subtracted. The winds have a southeasterly direction and thus, both the winds and the radiation could contribute to the observed warming.

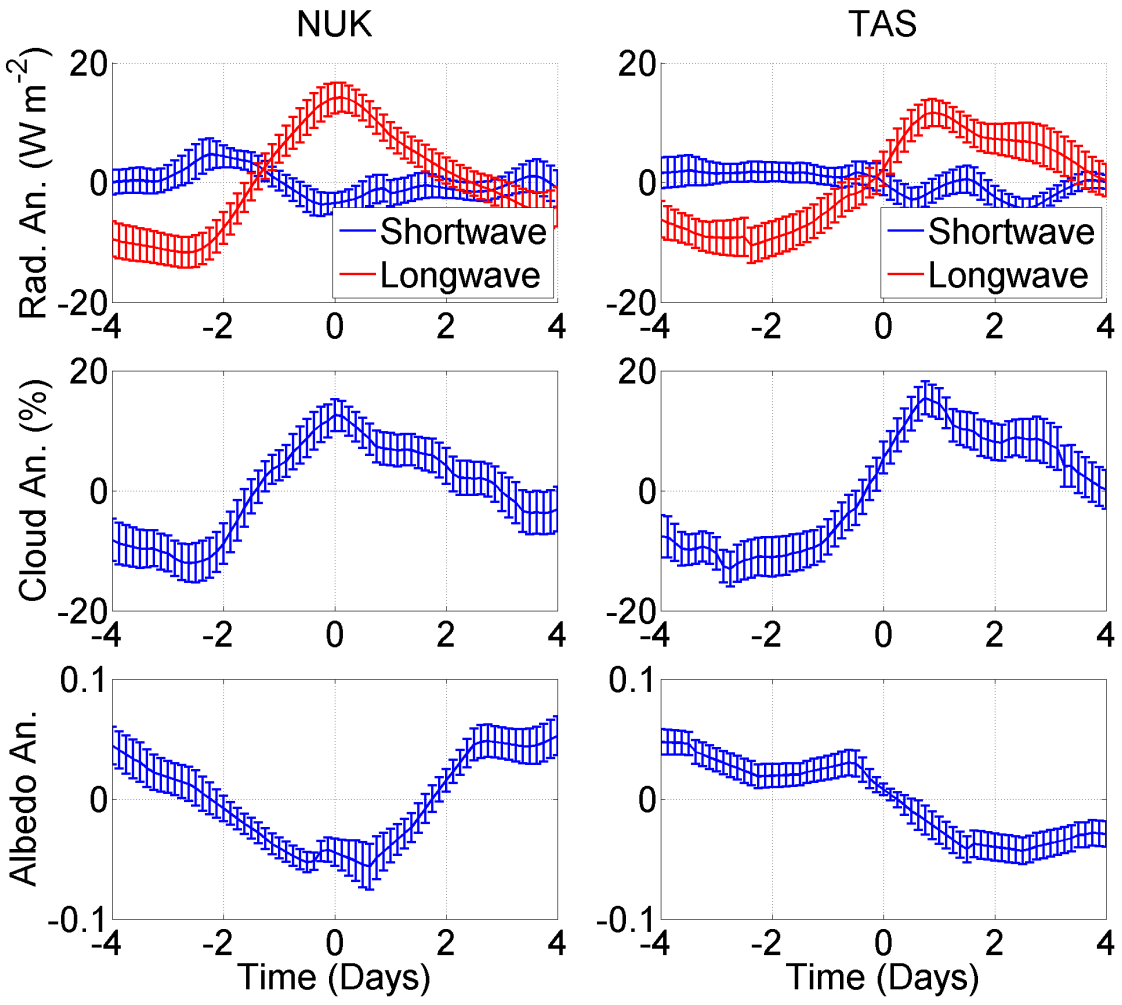

Figure 2-16: Composites of radiation, cloud cover, and albedo evolution during melt events (means subtracted) with PROMICE weather stations in Nuuk (NUK) and Tasiilaq (TAS). Both stations record ∼60 events.

2.6 Summary and Discussion

In this study, I have characterized strong winds across Greenland's coast and analyzed their influence on the heat fluxes over the ocean and the ice sheet. I have found that the strongest winds occur in the south, and winds across the southeast coast achieve the largest surface air temperature changes over the ice sheet of up to ∼10 K in the case of southeasterly flows, and ∼-8 K in the case of northwesterly flows (Figure 2-3). The strong southeasterly and northwesterly flows across the southeast coast are triggered by the interaction of a large-scale vorticity anomaly with the high Greenland topography and represent two (approximately opposite) phases of a stationary topographic Rossby wave. While the topography thus determines the scale of the events, their variability is controlled by the large-scale atmosphere. In order to approximate this variability, I have used an EOF mode based on SLP that is associated with a low pressure anomaly either southeast or northwest of the southern dome, and thus describes the direction of the geostrophic flow across the southeast coast (Figure 2-10).

Northwesterly flows across the southeast coast advect cold air over the Irminger Sea (Figure 2-3). In addition, I have found that they are connected with cold air advection from the Canadian Archipelago over the Labrador Sea, and with cold air advection from northern Greenland and the Arctic Ocean over the Greenland Sea. This can result in enhanced ocean heat losses in these regions, and I find that the interannual variability of the EOF mode, that describes the flow across the southeast coast (PC_3), is correlated with the winter mean heat fluxes over the Greenland, Labrador and Irminger Sea with a correlation coefficient of $r = 0.75$ (Figure 2-12d). Häkkinen et al. [2011] suggested that the heat fluxes over the Irminger Sea are highly anti-correlated with the blocking mode over Greenland [Scherrer et al., 2006], which is connected to the PC_3. Since the advection of cold air across the Arctic border can result in large heat fluxes [Pickart et al., 2003a, Våge et al., 2009, Oltmanns et al., 2014], and is at least partially described by the PC_3, this study provides a physical

explanation for the high correlation found by Häkkinen et al. [2011].

In addition, I have shown that southeasterly flows over southeast Greenland advect warm air from the ocean and upper levels over the ice sheet. Previous studies have suggested that extreme summer melting is preceded by warm air flows across the west coast and attributed them to a strong anticyclone over Greenland [Box et al., 2012, Hanna et al., 2014]. In this study, I have found that the temperature over the ice sheet is also influenced by flows across the southeast coast (Figure 2-3), and that these flows can result in sudden increases of the melt extent, mostly in fall, winter and spring. Composites of these melt events with weather stations suggest that the warming during the events is due to the combined effect of warm air advection across the southeast coast, an increase of the atmospheric moisture content, and a decrease of the surface albedo. The increased moisture content in the atmosphere contributes to the warming because it reduces the amount of outgoing longwave radiation. An enhanced atmospheric moisture content was also found to be influential for extreme melting during the summers in 1889 and 2012 [Neff et al., 2014].

Summer melting over Greenland has previously been quantified with the Greenland Blocking Index (GBI) [Overland et al., 2012, Hanna et al., 2013, 2014]. The GBI is defined slightly differently compared to the blocking index used by Häkkinen et al. [2011], but the two indices are closely related to each other, and to the PC_3: If the GBI is high, the anticyclone over Greenland is strong and blocks the passage of cyclones over Greenland north of the southern dome. Instead, cyclones are more likely to pass Greenland farther south such that the flow across the southeast coast is southeasterly, and warm air is advected onto the ice. Thus, in this study, I have connected these previously identified large-scale modes with the topographically forced wind events and their heat fluxes over the ice sheet and ocean. Even so, I stress that the influence of these southeasterly flows on the ice sheet is small in summer, and that the radiative fluxes associated with the anticyclone are likely more important. Moreover, the GBI includes long-term changes in temperature and reproduces the ob-

served warming trend over Greenland, which is not included in the PC_3. This stresses that warm air advection across the southeast coast is not the only factor determining temperature over the ice sheet, especially in summer when radiative fluxes are more important.

It is known that the atmospheric circulation over Greenland in summer influences the total melting [Fettweis et al., 2011, Hanna et al., 2013]. The fact, that the winter circulation can influence the ice sheet later in the year, has not previously been acknowledged. Yet, the atmospheric variability, the winds, and thus the heat fluxes, are largest in winter, suggesting that the direct influence of the atmospheric circulation on the ice sheet through the turbulent heat fluxes is particularly pronounced in winter. The effect of warm winds in winter can be enhanced by other terms in the radiation budget, such as reduced outgoing longwave radiation due to increased cloud cover associated with the cyclone that triggers the winds. Here, I used the one-dimensional heat equation to estimate how much additional heat can be stored in deeper layers of the ice sheet during warmer winters. I find that the anomalous heat can be conducted to depths greater than 2.5 m, and the associated heat storage can shift the onset of the melt season to an earlier time by up to three weeks. Thus, these results indicate that the atmospheric circulation in winter can precondition melting in the spring, and thereby influence the ice sheet later in the year.

I conclude that strong atmospheric flows across Greenland's coast indeed affect the surface energy balance of the ice sheet and the ocean. Previous studies have emphasized the complexity of atmospheric variability over the North Atlantic and suggested that several modes of variability need to be considered together [Moore et al., 2011, Moore and Renfrew, 2011]. Ocean-atmosphere-cryosphere interactions over Greenland add to the complexity, especially when considering melting. Here, I have shown that melting in the spring can also be affected by the winter atmospheric circulation because the heat capacity of snow adds a memory effect to the climate over the ice sheet and needs to be taken into account.

Chapter 3

Strong downslope wind events in Ammassalik, southeast Greenland

This chapter has been published in a modified form in the Journal of Climate [Oltmanns et al., 2014]. The authors are M. Oltmanns, F. Straneo, G.W.K. Moore, and S.H. Mernild. ©American Meteorological Society. Used with permission.

3.1 Abstract

Ammassalik in southeast Greenland is known for strong wind events that can reach hurricane intensity and cause severe destruction in the local town. While a large-scale overview of strong wind events in this region (the SE events) was provided in Chapter 2, their local characteristics, dynamics and impacts on the nearby fjord and shelf region are mostly unknown.

Here, data from two meteorological stations and the reanalysis product ERA-I are used to identify and characterize in more detail these strong downslope wind events that are especially pronounced at a major East Greenland Fjord, Sermilik Fjord, within Ammassalik. Their local and regional characteristics, dynamics and impacts on the regional sea ice cover and air-sea fluxes are described. Based on a

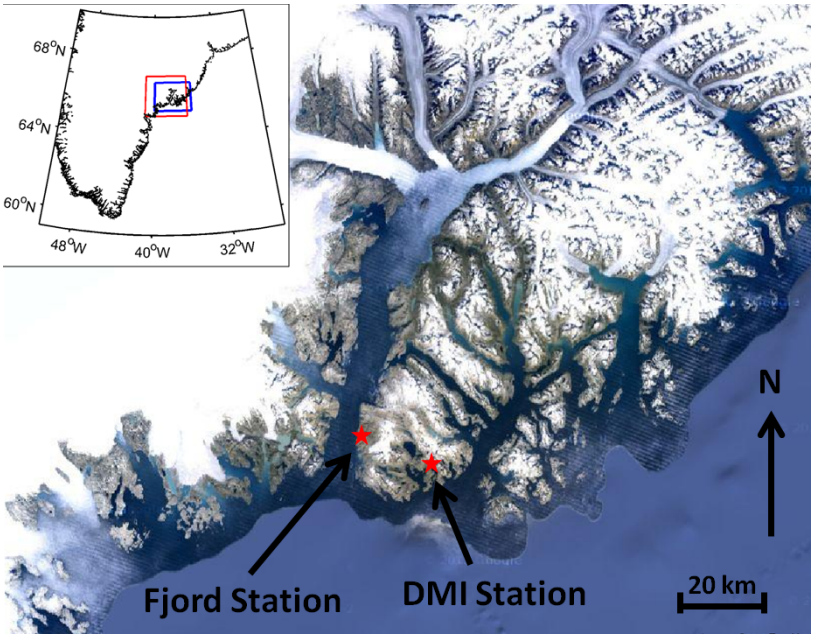

Figure 3-1: Map of the Ammassalik area in southeast Greenland with the locations of the two meteorological stations at and near Sermilik fjord. The satellite image shown (googleearth.com) is from the region indicated by the blue box in the inset. The Ammassalik region, used in the text, is defined as the region within the red box shown in the inset.

composite of the events it is concluded that ERA-I obtains mostly the same events as the weather stations, but that it underestimates the wind speed locally. It is shown that the downslope wind events last for about a day. They are associated with a deep synoptic-scale cyclone between Iceland and Greenland and advect cold dry air down the ice sheet. The downslope flow is accelerated by the gravitational acceleration, flow convergence inside the Ammassalik valley and a synoptic pressure gradient acceleration. Wind events are associated with a large buoyancy loss over the Irminger Sea and it is estimated that they drive one fifth of the net wintertime loss. Also, the extreme winds drive sea ice out of the fjord and away from the shelf.

3.2 Introduction

The Ammassalik region of southeast Greenland is well known for strong winds blowing off the ice sheet, which can be of hurricane intensity and cause severe destruction [Rasmussen, 1989, Born and Boecher, 2000, Mernild et al., 2008]. These winds are called 'piteraqs' and the strongest was observed on February 6, 1970, with estimated wind speeds of 90 m s^{-1} and temperatures of -20 °C [Born and Boecher, 2000]. While similar events occur in other regions along the coast, e.g. in Kangerlussuaq north of Ammassalik [Bromwich et al., 1996], they are most prominent in Ammassalik and thus, piteraq is an Ammassalik term [Born and Boecher, 2000]. It means 'sudden strong and cold wind, directed out of the fjord', where the fjord is Sermilik Fjord, a major East Greenland fjord in Ammassalik (Figure 3-1). In the preceding chapter, I have identified a distinct type of high-speed wind event in southeast Greenland, but the connection between these SE events and the piteraqs reaching hurricane intensity in Ammassalik, is unclear.

Earlier studies have addressed the nature of the strong winds and found that they occur as a combination of different driving forces. The flow originates from the Greenland ice cap where the radiational cooling of the boundary layer results in a katabatic wind that accelerates over the steeper slopes at the coast [Rasmussen, 1989, Parish and Cassano, 2001, Parish and Bromwich, 1987, Schwerdtfeger, 1984, Heinemann, 1999]. The valley in Ammassalik and the steep topography around Sermilik Fjord channel the katabatic flow and intensify the wind speeds [Klein and Heinemann, 2002, Bromwich et al., 1996, Heinemann and Klein, 2002]. This is in agreement with the results from the previous chapter, since I found that SE events are characterized by a spatially confined flow out of the Ammassalik valley, in contrast to downslope wind events at the west coast, where they cover a relatively broad area over the ice sheet. Case studies have indicated that the boundary layer flow is supported by a synoptic-scale cyclone such that the geostrophic flow is in the same direction as the downhill topographic gradient [Mills and Anderson, 2003, Klein and Heinemann,

2002, Heinemann and Klein, 2002], which again agrees with the SE events. Thus, both the synoptic and the topographic support are likely important during strong downslope wind events. Other case studies of downslope storms in Ammassalik indicate the existence of mountain wave breaking [Doyle et al., 2005] and the creation of meso-cyclones [Klein and Heinemann, 2002]. These results suggest the importance of a variety of forcings and dynamical features for the downslope flow during individual storms and the SE events, but to date there has been no generalized study of their local dynamics inside the valley of Ammassalik.

Moreover, in the preceding chapter I have identified the southeast Greenland coast as a key region for ocean-atmosphere interactions. The Irminger Sea, downstream of the valley, is an important ocean convection site [Pickart et al., 2003b, Vage, 2010], and thus part of the Meridional Overturning Circulation [Jungclaus et al., 2005, Stouffer et al., 2006] that influences the climate of northwest Europe [Vellinga and Wood, 2002]. Deep ocean convection is an intermittent phenomenon that is triggered by intense winter storms which force large buoyancy losses [Marshall and Schott, 1999]. Yet, in the preceding chapter, the northwesterly flow across the southeast coast was approximated with a large-scale atmospheric mode to investigate the interannual variability of the heat fluxes over Irminger Sea, and the immediate impact of individual strong downslope wind events is uncertain. While previous studies have argued that tip jets are associated with a large heat loss over the Irminger Sea [Våge et al., 2009, Pickart et al., 2003a], to date, no study has examined the direct impact of strong downslope wind events on ocean convection or the heat loss over the Irminger Sea.

Furthermore, since downslope wind events are directed offshore, they can potentially advect sea ice offshore [Bromwich and Kurtz, 1984] with a possible feedback on the wind intensity due to the resulting air-sea interaction [Gallée, 1997, Pettré et al., 1993]. Indeed, numerical simulations of specific events in Ammassalik have confirmed this feedback [Heinemann, 2003]. Apart from impacting the ecology by creating coastal polynyas, the removal of sea ice away from the coast could lead to

local freshening of the Irminger Sea. The removal of sea ice, moreover, might not be confined to the shelf region but could extend into Sermilik Fjord, with possible effects on Helheim glacier, a large Greenland glacier that drains into Sermilik Fjord. In fact, several authors have found a connection between the movement of outlet glaciers and the existence of a dense sea ice and iceberg cover (ice mélange), which exerts a back pressure on the glacier and inhibits calving [Amundson et al., 2010, Howat et al., 2010, Walter et al., 2012]. Thus, if downslope wind events remove the local sea ice cover in Sermilik Fjord, they could contribute to the destabilization of Helheim glacier.

The questions I will address in this chapter are therefore:

- How does the large-scale wind field in southeast Greenland compare to that in other regions of Greenland?

- What is the connection between the large-scale flow field (and the SE events) and strong downslope wind events in Ammassalik? Specifically, what are the local characteristics of downslope wind events inside the valley and at Sermilik Fjord, and how does ERA-I describe them in comparison to local weather stations?

- What is the vertical extent of the wind events? Do I see evidence for mountain waves in ERA-I?

- What are the dynamics of the events over the coastal slope in Ammassalik? Specifically, how important is the topography relative to the large-scale synoptic forcing?

- What is the immediate impact of individual strong events on the heat and buoyancy fluxes over the Irminger Sea?

- What is the influence of strong downslope wind events on the coastal sea ice cover, especially near the glacier?

To address these questions, I will present a comprehensive study of strong downslope wind events in Ammassalik using the reanalysis ERA-I and two meteorological stations, one inside the valley of Ammassalik and one directly at Sermilik Fjord. While I find that ERA-I underestimates the wind speed observed at the weather stations, it mostly obtains the same wind events as the stations. I am calling them strong downslope wind events (DWE) in the following, as their definition slightly differs from that of the SE events, and the focus here is more on the local downslope flow. However, DWE and SE events are in large part equivalent, and the large-scale characteristics of the DWE agree with those obtained for the SE events.

Based on vertical sections along and across the flow in Ammassalik, I find that DWE are associated with a surface intensified jet, that is strongest within the valley and advects cold and dry air across the coast. By evaluating the momentum balance of the downslope flow, I will further show that DWE are accelerated through channeling inside the valley of Ammassalik, by a synoptic pressure gradient and by the gravitational force. Moreover, I find that individual events can result in heat fluxes of up to 1000 W m^{-2}, and using remote sensing data, I show that they advect sea ice away from the coast and out of the local fjord, with potential implications for Helheim glacier.

3.3 Data

I use three different data sets to identify and characterize DWE. Two of them are meteorological stations, and the other one is the reanalysis product ERA-Interim from the European Centre for Medium-Range Weather Forecasts (ECMWF) which is described in Chapter 2. It has an approximately 80 km resolution at the surface, and I use it to gain insight in the three dimensional structure of the atmospheric flow, to put the local observations from the weather stations in a larger scale context, and to quantify the heat and buoyancy fluxes. To understand how well ERA-I describes

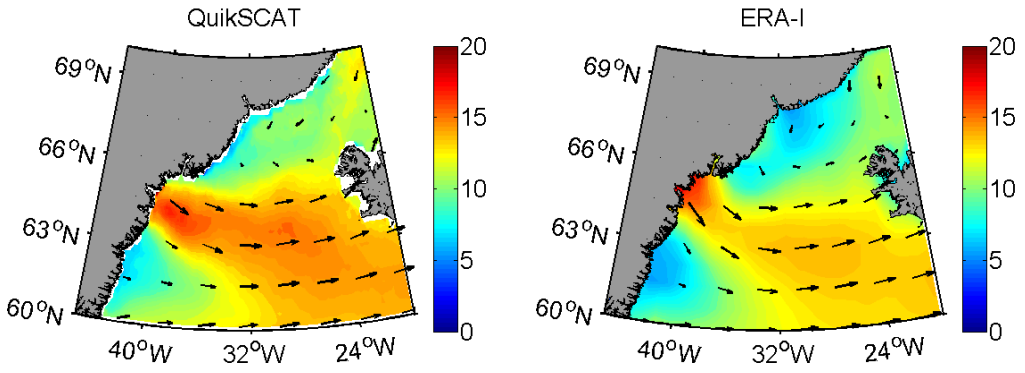

Figure 3-2: Composite of wind speed (m s^{-1}) during the 72 DWE that were identified with ERA-I in the time period when QuikSCAT was operating. Shown are the composites with QuikSCAT and ERA-I. The method used to identify DWE is described in section 3.4.

DWE over the ocean, I compared its output to QuikSCAT satellite data. I used the 2011 reprocessed QuikSCAT ocean wind vectors with an improved geophysical model function [Ricciardulli and Wentz, 2011] that I obtained from Remote Sensing Systems, Santa Rosa, CA, USA. I found that the structure of the wind field during the events was in good agreement but that ERA-I underestimates the wind speeds by $\sim$1 to 2 m s^{-1} in the region of the peak wind speeds (Figure 3-2).

One of the meteorological stations is located on a hill in Sermilik Fjord (Figure 3-1) at 65°40.8' N, 37°55.0' W at a height of 25 m above sea level. Its official name is 'Station Coast'. The station was established by the University of Copenhagen in June 1997 and monitors meteorological conditions at a 3-hourly interval prior to August 21, 2007, and a 10-minute interval thereafter [Mernild et al., 2008]. Since August 8, 2008, there has been a duplicate station in case of failure of the primary. When data from one station are not available, they are replaced by data from the other. No data are available from June 28, 2006, to August 6, 2006, and from May 29, 2007, to August 20, 2007. Every observed time series from the stations was manually analyzed in detail and compared to observations from other stations in the region, to make sure that observational errors were eliminated from the data set. In the following, I will refer to this station as the fjord station.

The other meteorological station is in Tasiilaq, a town near the fjord (Figure 3-1). It has been operated by the Danish Meteorological Institute (DMI) since 1958 and is located at 65°36' N and 37°37' W at 53 m above sea level.[1] Several small shifts of the station location occurred during the period of operation, but I did not find any discontinuities in the data set. Data were recorded at a 3-hourly interval before August 5, 2005, and at a 1-hourly interval thereafter. During this last period, some data gaps exist but in most cases they are limited to a few days. The data are distributed and quality controlled by the DMI [Carstensen and Jorgensen, 2010, Cappelen, 2011]. In the following, I will refer to this station as DMI station.

The three data sets are complementary in a number of ways. The fjord station measures the winds directly inside the fjord valley where downhill winds are focused and the wind speed, likely, highest. The DMI station is only 16 km away from the fjord station but not directly inside the valley. Thus, I expect the winds to reflect more the large-scale topographic gradient. The main advantage of the DMI station data set is its long time span from 1958 onward. The ERA-I product provides information on the vertical extent of the flow and puts the observations from the local weather stations in a large-scale context. While the Sermilik Fjord is not resolved, the larger scale valley of Ammassalik is.

To investigate the impact of the winds on sea ice, I use a sea ice concentration product provided by the National Snow and Ice Data Center (NSIDC). It is obtained from the Advanced Microwave Scanning Radiometer—Earth Observing System (AMSR-E) on board of the NASA Earth Observing System (EOS) Aqua satellite [Cavalieri et al., 2004]. The level 3 gridded 89 GHz brightness temperatures have been processed by the University of Hamburg to calculate sea ice concentration with a resolution of 6.25 km [Spreen et al., 2008]. The record starts in June 2002, ends in September 2011 and has a daily resolution. I use the sea ice concentration for a confined region along the

[1]Before March 31, 1982, it was located at 65°36' N and 37°38' W at 36 m above sea level. After that date it was moved to a 37°37' W at the same latitude but at a height of 50 m above sea level, less than a kilometer away from its original location. On August 15, 2005, it has been raised to 53 m above sea level.

	DMI Station	Fjord Station
Mean Wind Speed (m s^{-1})	2.60±3.48	5.21±3.77
Mean Wind Direction (degree)	305.76±74.67	58.52±53.88
Directional Constancy	0.23	0.74
Shape Parameter	1.22	1.38

Table 3.1: Statistical parameters (mean with standard deviation) of the winds recorded by the meteorological stations from November through April. The mean is taken from 1998-2012 for the fjord station and from 1958-2012 for the DMI station.

southeast Greenland coast (Figure 3-12). Since the presence of sea ice in this region is restricted to the months January through May, I limit the analysis of the impact of DWE on sea ice to this period.

3.4 Method

Southeast Greenland is unique in that it includes the large-scale valley around Ammassalik (Figure 3-3) where the topography is particularly steep and the large-scale flow can be channeled. In order to understand the general forcing of winds in Ammassalik compared to other regions in Greenland, I first investigate the mean 10m-wind field obtained from ERA-I. I focus on the months November through April, as the synoptic variability is largest in winter, and in the previous chapter it was found that SE events are frequent in all seasons but summer. Including more months (e.g. September through May) or fewer months (e.g. December through March) does not change the results appreciably. Specifically, I examine where the mean winds follow the (downslope) topographic gradient, and where they are more strongly influenced by the mean sea level pressure field (Figure 3-3).

Over the ocean, the mean winds closely follow isobars which are largely associated with the Icelandic Low (Figure 3-3). Above Greenland, the mean geopotential is high, giving the wind field an anti-cyclonic orientation. The east Greenland coast (including Ammassalik) separates the low from the high geopotential. In this region, the mean

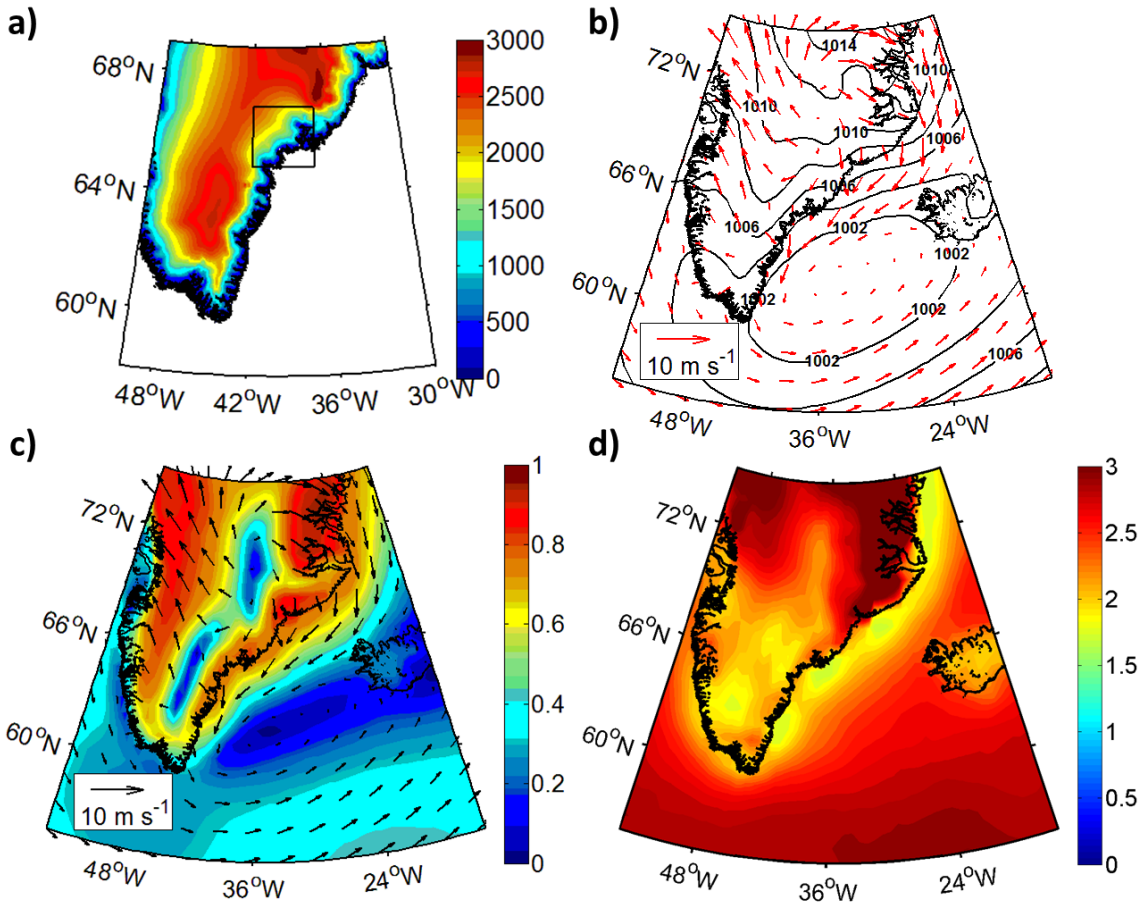

Figure 3-3: a: Surface elevation (m). The black box delineates the region that I refer to as Ammassalik. b: Mean SLP field (hPa) with the mean 10m-surface winds (November through April) from ERA-I. The winds tend to follow isobars, but in Ammassalik they are directed across isobars from high to low pressure and downslope. c: Directional constancy with the mean 10m-surface winds (also from ERA-I). In Ammassalik, as well as in many other coastal regions, downslope winds (with a rightward deflection due to the Coriolis force) are very common. d: Shape parameter from the Weibull distribution. The low shape parameter along the southeast Greenland coast indicates a skewed wind speed distribution with many low wind speeds and a few very high wind speeds.

wind field is not purely geostrophic but slightly distorted as the winds tend to be downslope and down pressure gradient. Also, the directional constancy (defined as the ratio of the speed of the mean winds to the mean wind speed [Moore, 2003, Parish and Cassano, 2003]) is large along the coast, indicating that the winds are directed downslope most of the time. At the DMI station, the directional constancy is considerably smaller ($\sim$0.23), indicating that the wind direction varies on scales (temporal or spatial) not resolved by ERA-I (Table 3.1). The fjord station records a larger directional constancy ($\sim$0.74). A large directional constancy also indicates that the wind direction is predominantly influenced by the topography, whereas a low directional constancy suggests a variable wind field, as typical for regions in which cyclones are frequent. At the DMI station, the mean wind direction is northwesterly and in the fjord station it is northeasterly. The directional constancies and the mean wind directions are likely imposed by the local topographic setting at the location of the respective station.

Wind speed distributions are often described by a Weibull distribution [Hennessey, 1977, Palutikof et al., 1999, Pavia and O'Brien, 1986]. The Weibull distribution is characterized by its shape and its scale parameter. While the scale parameter is proportional to the mean wind speed, the shape parameter determines the shape of the distribution. For instance, a shape parameter of 3.6 indicates a Gaussian distribution. Exponential distributions have a shape parameter of 1, and Rayleigh distributions have one of 2. A shape parameter of less than one indicates a monotonically decreasing distribution. Figure 3-3 displays the shape parameter for the wind distribution in Greenland. It is comparatively small over southern Greenland compared to northern Greenland, with minima along the southeast and east coast, including southwest of the Ammassalik valley. Small shape parameters indicate that the wind speed distribution is skewed and has a long tail, such that there are frequent low-speed winds and sometimes very high-speed winds. The large variability of the wind speed, that is typically associated with small shape parameters, requires some larger scale

	Fjord	DMI	ERA-I
Time Span	1998–2010	1958–2010	1979–2010
Direction Condition, clockwise (degree)	none	270–20	270–20
Speed Condition (m s^{-1})	>17.4	>14	>10
Mean number of events per year	7.8±3.1	7.6±3.2	6.9±2.9

Table 3.2: Definitions of DWE in the three different data sets. Other definitions give qualitatively the same results.

atmospheric variability and cannot be attributed to the topographic forcing alone. Small shape parameters were also found in Coats Land, Antarctica [Renfrew and Anderson, 2002]. For this region, it was found that winds are predominantly katabatic 40% to 50% of the time, while at other times the flow was due to other driving forces such as a synoptic-scale low pressure system [Renfrew and Anderson, 2002]. A summary of some statistical parameters describing the wintertime winds in the different data sets is given in Table 3.1. The shape parameter of the mean winds is even smaller in the other two data sets (1.23 in the DMI station and 1.26 in the fjord station), indicating that the skewness of the wind distribution is even more pronounced. It is the long tail of high-speed winds, that I investigate in the rest of this study.

To build a composite of DWE, I followed the general criterion that they be downslope and strong. Due to the different locations and characteristics of the three data sets, the specific definitions in each of them are, however, slightly different (Table 3.2). The identification of the wind events in ERA-I is based on the DMI station location. This does not coincide with the location where ERA-I records the fastest winds during DWE, but using this location results in a better agreement in terms of the obtained wind events. However, alternative locations in Ammassalik give qualitatively the same results.

At the fjord station, wind speeds above 5 m s^{-1} are usually only reached by winds in the along-fjord direction. Winds from other directions are blocked by the

mountains surrounding the fjord. To capture only the strongest winds, I define an event as having a speed larger than the mean plus four standard deviations. For the time period from 1998 to 2010, this speed condition is 17.4 m s^{-1}. Requiring the events to be at least 48 hours apart so as not to count an event twice, this results in an average of 7.8 events per winter. The speed limit is arbitrary, but alternative definitions do not change the results qualitatively, only the number of obtained events differs.

In the other two data sets, the strongest winds have two preferred directions. Of the two, downslope winds are parallel to the topographic gradient in Ammassalik. Based on previous studies, I identified the winds with the other direction as barrier winds which are directed along the coast [Moore and Renfrew, 2005, Petersen et al., 2009, Harden et al., 2011]. In addition, I confirmed that most of the DWE identified in the fjord data have the downhill direction in the other two data sets. Downslope winds at the DMI station are southeastward (between 300 and 360 degree in geographical coordinates), even though the winds have a clear north-to-south orientation in the data from the fjord station. It is likely that the difference in direction of 0° to 60° is due to differences in the local topographic gradient between the fjord and the DMI station area.

In order to separate the downslope winds from the barrier winds, I apply a speed and a direction condition to the winds in ERA-I and the DMI station data. Wind directions need to be between 270° and 20° (clockwise). The number of events obtained this way is not sensitive to the direction condition because they naturally fall into a very narrow direction range. Thus, a direction condition between 300° and 360° (or 180° to 20° which just filters out the barrier winds) gives qualitatively similar results. The condition on speed, which is 10 m s^{-1} in ERA-I and 14 m s^{-1} in the DMI station, affects the number of DWE obtained more strongly. I chose the above limits so that, I obtain approximately the same number of DWE in the common time period which is about seven events per year. The comparatively smaller speed limit

in ERA-I is likely related to the coarse resolution of the model. As I show below, the DWE captured with these slightly different definitions have similar composites and share about 70% of the obtained events. The wind events that are obtained by the fjord station only, are recorded by the DMI station and ERA-I as either downslope winds that are not fast enough to fulfill the condition on wind speed or as very strong barrier winds. Moreover, the DWE obtained by ERA-I are also connected with the SE events investigated in the previous chapter. Despite their different definition 78% of the DWE recorded by ERA-I correspond to SE events, suggesting that they are in large part equivalent.

3.5 Results

3.5.1 Characteristics

The seasonal distribution of events obtained is similar in all three data sets (Figure 3-4). The bulk of the events occurs between October and April with peaks in November and February/March, and a large interannual variability (Figure 3-4). I use all of the obtained DWE to build a composite of wind speed, sea level pressure and temperature in each data set (except for sea level pressure from the fjord station where it is not measured). Whenever I refer to wintertime wind events or winter climatology I define wintertime as the months November through April. Figure 3-5 shows the evolution of these surface fields from one day before the time of maximum wind speed until one day afterwards. The origin (0 h) is defined as the time of maximum wind speed and negative time means time before the wind speed reaches its maximum. To derive the anomaly (of temperature and pressure), I subtract the mean during the event. The peak intensity of the wind speed is largest in the fjord station and smallest in ERA-I (Figure 3-5). The time between the initial increase in wind speed and the return to low wind speed is about 20 to 30 hours in all three data sets. Wind speeds above 10 m s^{-1} are sustained for about 10 hours. As the

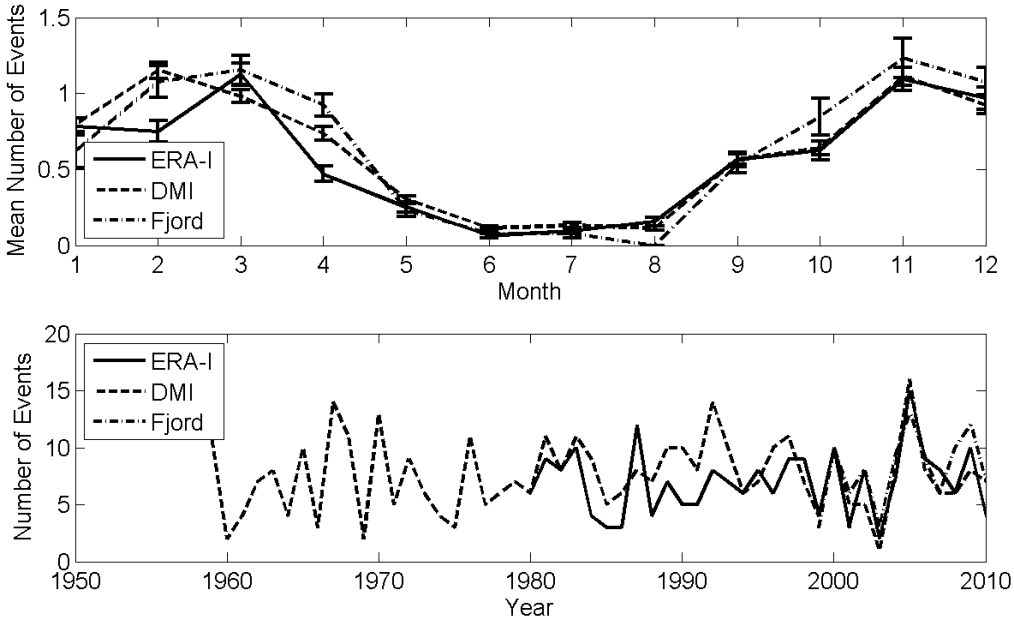

Figure 3-4: Mean number of events per month (top) and number of events per year (bottom) obtained with the two meteorological stations and ERA-I. Error bars are represented by the standard error of the mean. DWE occur mainly in the winter months and have a large interannual variability. Note, that I defined a year to extend from July to June so as not to split the winters.

wind speed increases, both the temperature and the pressure drop. The temperature minimum is reached slightly after the time of maximum wind speed has passed while the minimum in pressure occurs before the maximum wind speed is reached. Not shown is the relative humidity evolution recorded by the DMI station, but its curve resembles the temperature curve closely with a relative humidity drop of 20%. Also not shown is the DMI station cloud cover evolution. I find that 40 hours before the event the sky has a cloud cover of almost 80%. During the event the sky clears up by more than 40%. About ten hours after the event, the cloud cover starts to increase again. The climatological winter mean cloud cover is 70%.

A composite of the large-scale wind velocity distribution using ERA-I shows the strong winds of $\sim$20 m s^{-1} occur inside the valley of Ammassalik, where the flow converges (Figure 3-6). I note that ERA-I records the maximum wind speed not directly at the fjord, where the two stations are. The wind speed remains large as the flow crosses the coastline and still reaches $\sim$15 m s^{-1} over a large part of the Irminger Sea. The corresponding sea level pressure field indicates that the flow is supported by a synoptic-scale geostrophic flow associated with a cyclone located between Iceland and east Greenland (Figure 3-6), which is in agreement with the results from the previous chapter. Also shown is the ERA-I boundary layer height, defined as the level where the Richardson number reaches a critical value $Ri_{cr} = 0.25$ [ECMWF, 2010]. DWE, and the associated cyclone, are associated with a significant thickening of the boundary layer over the ocean and over Iceland. The boundary layer height is a diagnostic for the impact that the air-sea interaction is having on the lower troposphere, and a deep boundary layer can indicate a large heat flux from the ocean to the atmosphere. The 2m-air temperature field (Figure 3-6) reveals that the air over large parts of the Greenland ice sheet, and especially in the region from where the winds originate, is significantly colder during wintertime DWE compared to the winter climatology. To ensure that these results are not subjective to the specific definition of the DWE, I built these composites in ERA-I with slightly different definitions and

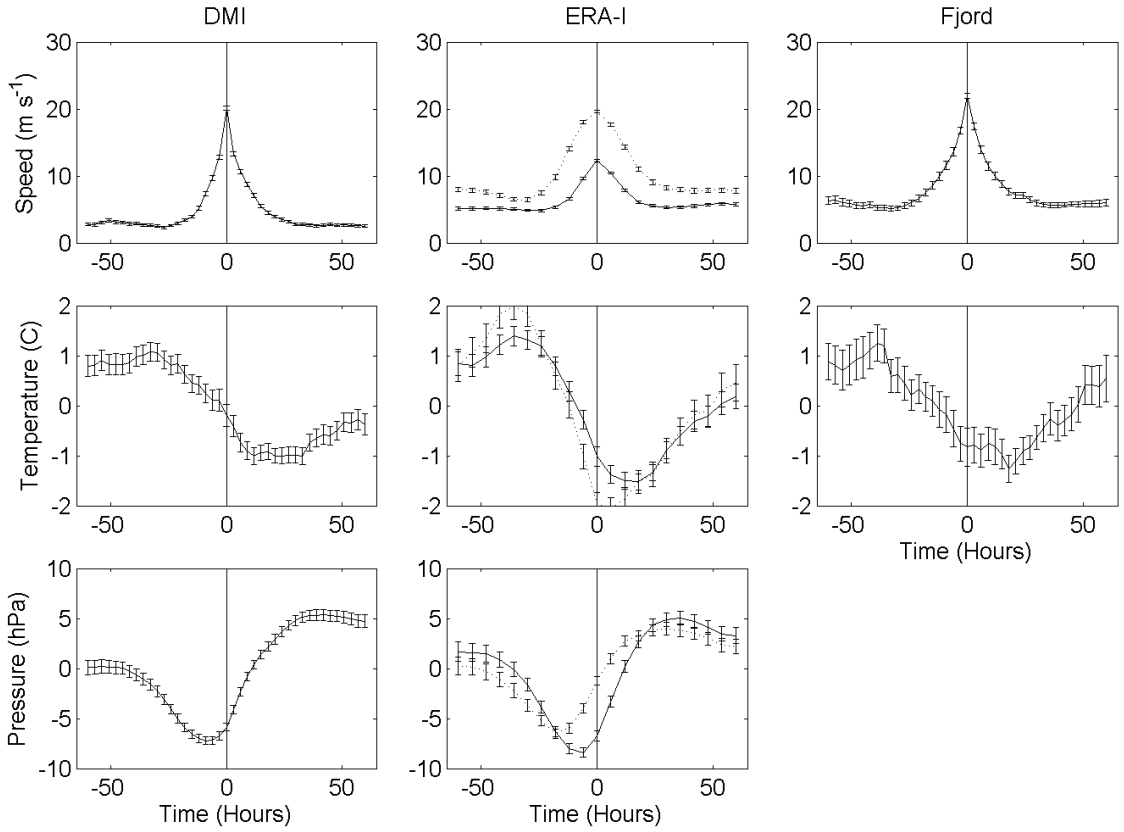

Figure 3-5: Composite of speed, temperature and pressure evolution in the DMI data, the fjord data and in ERA-I. Negative time means time before the time of maximum wind speed. Error bars are represented by the standard error of the mean. The solid line in the ERA-I panel is based on the DMI station location. The dotted line is based on the location where the wind speed in ERA-I is strongest, which corresponds to the cross-section of the two sections shown in Figure 3-6. Down-slope wind events feature a distinct drop in pressure and temperature.

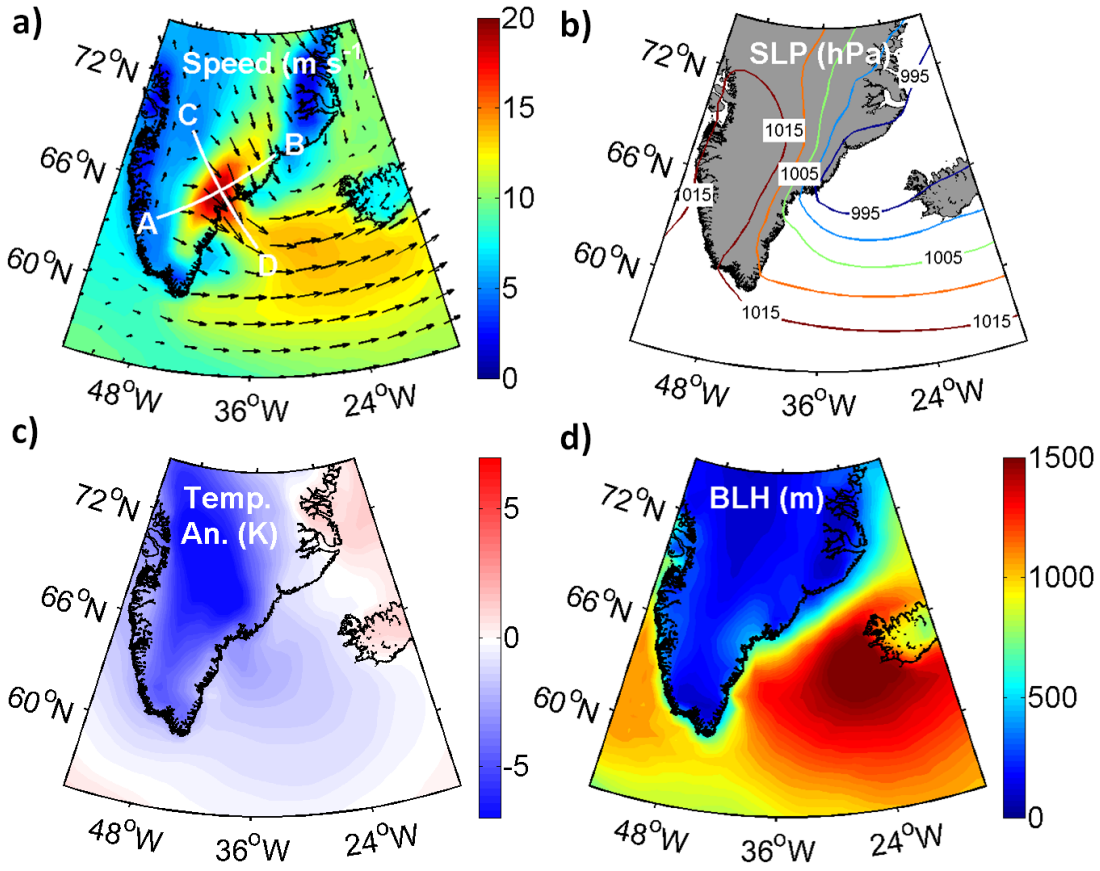

Figure 3-6: Composite of the ERA-I wind speed (a), and sea level pressure (b), temperature anomaly (c) and boundary layer height (d) during DWE. The temperature anomaly is the difference of the composite of the wintertime (November through April) events to the winter climatology. The lines in the wind speed composite mark the sections shown in Figure 3-7.

with the DWE identified with the DMI station or the fjord station. I found in each case that the composites do not change appreciably.

Vertical sections from ERA-I across and along the composite flow (see Figure 3-6 for section location) reveal that it consists of a broad jet with speeds of up to 25 m s^{-1}, a width of approximately 300 km and a height of about 2500 m (Figure 3-7). The jet closely follows the topography as it flows downhill and spills over the ocean. The potential temperature profiles indicate that the air is strongly stratified and the relative humidity sections show that the jet carries air that is largely under-saturated

with respect to water vapor. The along-section of specific humidity suggests that the air over the ice sheet is much drier compared to the air over the ocean. As the air passes over the ocean, its temperature and specific humidity content increase, which is likely a result of the air-sea fluxes (Figure 3-7).

3.5.2 Dynamics

To quantify the forcing of the flow, I set up the momentum budget along a linearized composite streamline section obtained from the ERA-I 10m-surface winds during DWE (Figure 3-8), where 'linearized' here means that the section has no curvature. The streamline section includes the location of the maximum wind speed in ERA-I. I find that it adequately represents surface winds of different events and that it coincides with the direction of the downslope topographic gradient. Following Mahrt [1982], I partition the temperature, pressure and density field into a basic state component and a component that is due to the gravity current. Next, I assume that the pressure and temperature perturbations associated with the gravity current are much smaller compared to those associated with the basic state, and I neglect the influence of moisture on the buoyancy, which is reasonable for most gravity flows [Mahrt, 1982]. Under these assumptions, and using the hydrostatic and the Boussinesq approximation, the momentum equation along the streamline section in the downslope direction x can be written as [Van den Broeke et al., 2002, Van den Broeke and Van Lipzig, 2003, van Angelen et al., 2011]:

$$\begin{aligned} \frac{\partial u'}{\partial t} + u'\frac{\partial u'}{\partial x}\,|_{z'}\cos(\alpha) + v\frac{\partial u'}{\partial y} + w'\frac{\partial u'}{\partial z'} - fv + F_{Res} = \\ \frac{g}{\theta_0}\theta\sin(\alpha) - \cos(\alpha)\,\frac{g}{\theta_0}\frac{\partial\hat{\theta}}{\partial x}\,|_{z'} - \frac{1}{\rho_0}\frac{\partial p_{amb}}{\partial x}\,|_{z}, \end{aligned} \tag{3.1}$$

$$F_t + F_{NL} + F_C + F_{Res} = F_G + F_T + F_S. \tag{3.2}$$

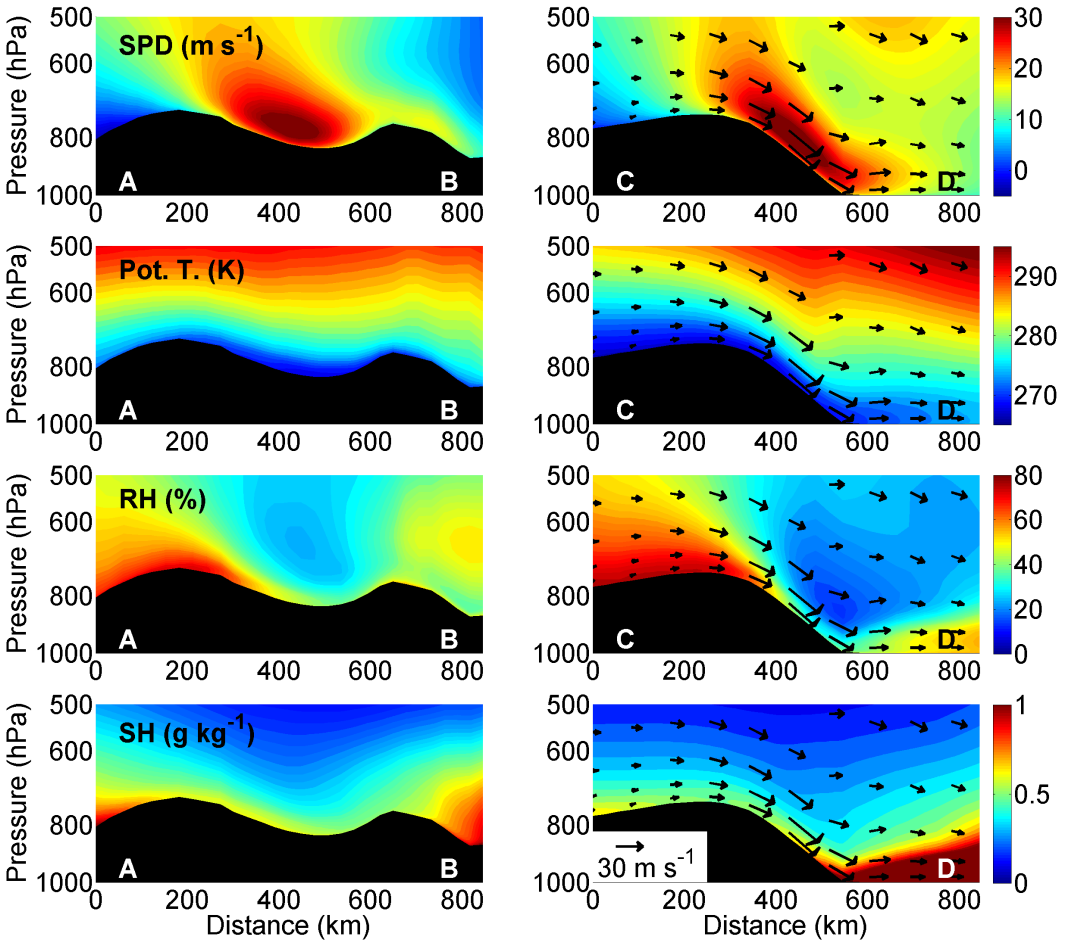

Figure 3-7: Sections along and across the downslope flow obtained from ERA-I. The section end points AB and CD are shown in Figure 3-6 The winds follow the topography closely. They are dry and cold but become moister and warmer as they cross the coastline.

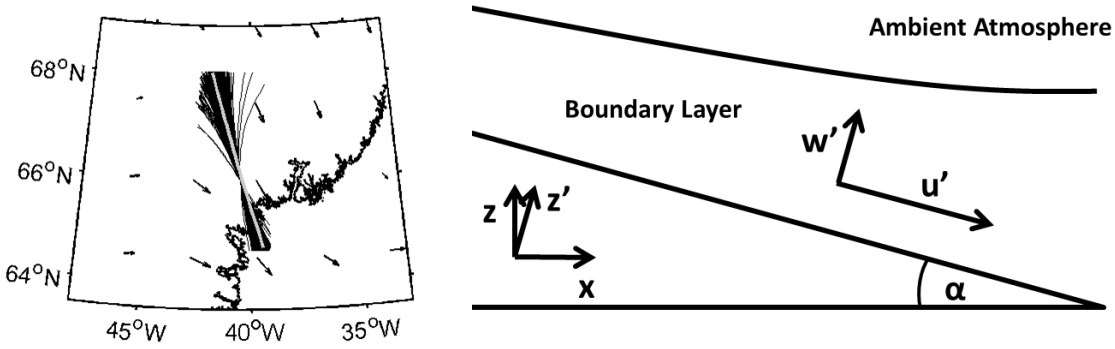

Figure 3-8: Left: Streamlines of the 10m-surface winds during DWE in ERA-I; the gray line represents the linearized mean on which the momentum analysis is based on. Right: Profile of the flow in the coordinate system used in the momentum analysis.

Here z' is the vertical coordinate perpendicular to the slope (positive upward), w' is the velocity perpendicular to the slope, u' the downslope velocity, v is velocity in the cross-slope direction y, t is time, θ_0 is the ambient (or basic state) potential temperature, θ is the temperature deficit, ρ_0 is density, p_{amb} is the pressure in the ambient atmosphere corresponding to θ_0, f is the Coriolis parameter, g is gravity, and α is the positive angle of the slope with respect to the horizontal (Figure 3-8). I define the temperature deficit as the difference between the temperature that the ambient atmosphere would have at the same height and that of the boundary layer (Figure 3-9). A positive temperature deficit means that the boundary layer temperature is colder than that of the ambient atmosphere. I calculate it by linearly extrapolating the potential temperature profile above some height (well above the temperature deficit layer) downwards to the surface. I carefully investigated the potential temperature profile along the section to make sure that the chosen level of 2000 m above the topography is reasonable. Small changes of this level affect the results only marginally. $\hat{\theta}(z)$ is the vertically integrated temperature deficit from z to z_t where the temperature deficit vanishes:

$$\hat{\theta}(z) = \int_{z}^{z_t} \theta dz. \tag{3.3}$$

On the left hand side of equation (3.2) are the local acceleration F_t, nonlinear advection F_{NL}, the Coriolis force F_C and a residual force F_{Res}. Following Van den Broeke et al. [2002], I call these forces 'passive' since they only exist in the presence of atmospheric motion [van Angelen et al., 2011]. F_{Res} includes friction and small-scale processes that are parametrized in the underlying model. On the right hand side of equation (3.2) are the active forces that drive the flow. These include the synoptic or ambient pressure gradient force F_S, the thermal force F_T and the gravitational force F_G. The ambient pressure gradient results from the synoptic-scale cyclone and also includes the horizontal pressure drag that is typically associated with flow over topography. The gravitational acceleration arises because of the presence of the potential temperature deficit over sloping topography, whereas the thermal acceleration is due to inhomogeneities of the temperature deficit along the direction of the flow. It is also responsible for the sea breeze circulation and exists even when the slope is absent. An increase (decrease) in the potential temperature deficit implies a local deceleration (acceleration) of the surface flow.

Above the temperature deficit layer, the ambient pressure gradient F_S corresponds to the full pressure gradient. Within the temperature deficit layer, it is obtained by integrating the ambient potential temperature gradient downwards [Van den Broeke et al., 2002, van Angelen et al., 2011]:

$$\frac{1}{\rho}\frac{\partial p_{amb}}{\partial x}\,|_z = \frac{1}{\rho}\frac{\partial p\,(z_t)}{\partial x}\,|_z + R_g \int_{\ln p(z)}^{\ln p(z_t)} \left(\frac{p}{p_0}\right)^{\frac{R_g}{c_p}} \frac{\partial \theta_0}{\partial x}\,|_p \, d\ln p, \tag{3.4}$$

$$\frac{1}{\rho}\frac{\partial p_{amb}}{\partial y}\,|_z = \frac{1}{\rho}\frac{\partial p\,(z_t)}{\partial y}\,|_z + R_g \int_{\ln p(z)}^{\ln p(z_t)} \left(\frac{p}{p_0}\right)^{\frac{R_g}{c_p}} \frac{\partial \theta_0}{\partial y}\,|_p \, d\ln p, \tag{3.5}$$

where again hydrostatic balance has been used, R_g is the gas constant and c_p the heat capacity at constant pressure. Here, I use a z_t of 2000 m above the topography. If I chose z_t to be 1700 m or 2300 m, the results do not change appreciably. I compute

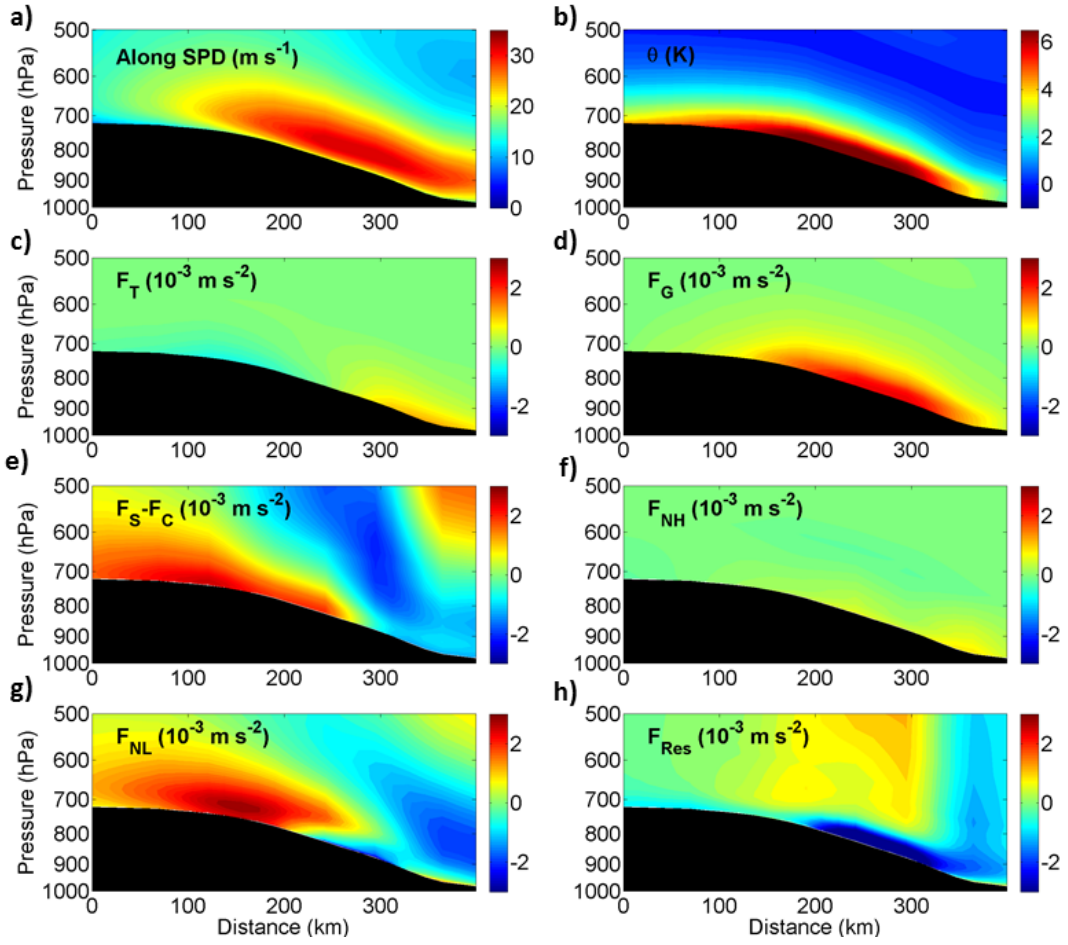

Figure 3-9: Composite analysis of the momentum balance during DWE in ERA-I along the section shown in Figure 3-8. (a) Flow component along the section. (b) Temperature deficit of the boundary layer with respect to the ambient atmosphere; a positive temperature perturbation indicates that the air is colder than that of the ambient atmosphere. (c), (d) and (e) show the thermal force F_T, the gravitational force F_G and the ambient pressure gradient force with the Coriolis force subtracted $F_S - F_C$. (f) The force resulting from non-hydrostatic effects F_{NH} is small compared to the ambient and gravitational force, indicating that it plays a minor role during the events, and that the splitting of the total pressure gradient is reasonable. (g) and (h) show the nonlinear advection and the residual which likely results from friction and some parametrized gravity wave drag.

the three active forces, the local acceleration, the Coriolis force and the nonlinear force individually for each DWE in ERA-I and then take the composite (Figure 3-9). I cannot close the momentum budget in ERA-I, since I cannot estimate the small-scale turbulence that is parametrized in the underlying model and so I have to infer the residual force from the other terms. Over the upper part of the slope, F_S is the dominant accelerating force, but towards the end of the slope it is decelerating the flow. F_G is large and positive over the central part of the streamline section, where the slope is steepest and the temperature deficit is largest. At the end slope, near the coast, the thermal force is also weakly accelerating the flow. The local acceleration is more than one order of magnitude smaller than the other terms, which is likely due to the coarse temporal resolution of the ERA-I output. Evaluating the local acceleration with the station data, I still find that it is one order of magnitude smaller than the other terms. The advective terms (F_{NL}) show that the flow is accelerating over the upper and central part of the slope and decelerating near the coast. The cross-slope component of F_{NL} (not shown) is comparable to the along-slope component, which confirms that the channeling in the valley is important (as indicated by Figure 3-6). The magnitude of the residual force is largest at the surface, where friction is impeding the flow. Above the surface, it is acclerating the flow over the central part of the slope, and decelerating it near the end, suggesting that unresolved turbulent processes are important for the flow field in these regions [Van den Broeke et al., 2002, Outten et al., 2009].

Under non-hydrostatic conditions, the total pressure gradient force F_P includes an additional term due to non-hydrostatic effects F_{NH}. I cannot calculate this term directly, so I infer its magnitude from the residual after splitting the total pressure gradient: $F_{NH} = F_P - F_G - F_S - F_T$ [Cassano and Parish, 2000]. Cassano and Parish [2000] found that this term is insensitive to model resolutions ranging from 100 km to 5 km, which suggests that ERA-I provides a reasonable estimate. I find that the magnitude of F_{NH} is small compared to the dominant terms (Figure 3-9), indicating

that non-hydrostatic effects play a minor role during downslope wind events and that the estimate of F_S is realistic. Since F_T has a similar magnitude compared to F_{NH}, it needs to be interpreted with care. Even so, a positive thermal acceleration near the coast is consistent with previous studies (e.g. Heinemann [2003]).

In addition, there could be momentum transport in internal gravity waves [Gill, 1982, Durran, 1990]. Indeed, Doyle et al. [2005] observed large-amplitude mountain wave breaking in Ammassalik during a DWE on 29 January 1997 that was also obtained with ERA-I. During this event, I observe downward trending potential temperature isopleths from the interior towards the sea in ERA-I (not shown), indicating a katabatic condition and evanescent mountain waves. This suggests that ERA-I does not resolve the complete wave dynamics, and it is possible that some gravity wave drag is parametrized in F_{Res}.

3.5.3 Impacts

Downstream buoyancy flux

The buoyancy loss at the surface of the ocean that occurs during intense winter storms is a major driver of deep and intermediate ocean convection [Marshall and Schott, 1999, Sathiyamoorthy and Moore, 2002]. DWE advect cold, dry air over the ocean and, as such, are likely associated with large heat and ocean buoyancy fluxes. To examine their impact I investigate the buoyancy flux associated with these events.

The buoyancy flux B is the sum of a thermal and a saline contribution, where the thermal contribution includes the radiative and turbulent heat fluxes Q and the saline contribution is tied to changes in surface water density due to precipitation or evaporation [Gill, 1982]:

$$B = \frac{g\alpha}{\rho_0 C_p} Q + \frac{g\beta S}{\rho_0} (P - E),$$
$$Q = (Q_S + Q_L + Q_{SW} + Q_{LW}).$$

Here, α and β are the thermal and haline expansion coefficients for sea water respectively, C_p is its specific heat, g is the gravitational acceleration, ρ_0 is a reference density, and P and E are precipitation and evaporation. Q_S is the sensible heat flux, Q_L is the latent heat flux, Q_{SW} is the heat flux due to the net shortwave radiation and Q_{LW} is due to the net longwave radiation. All of these variables are obtained from ERA-I and used to evaluate the buoyancy flux associated with DWE. I am using a sign convention such that a positive heat flux corresponds to a heat gain of the ocean and a negative buoyancy flux corresponds to a densification of the water at the ocean surface.

Since deep and intermediate ocean convection is known to be intermittent and tied to the occurrence of intense atmospheric forcing, I start by investigating the turbulent fluxes, the total heat flux and the buoyancy flux for one of the stronger events which took place on 28 December 2004. During this event, ERA-I shows maximum surface wind speeds of 25.9 m s^{-1} and a total heat flux of up to -1000 W m^{-2} over a large part of the Irminger Sea (Figure 3-10). Both the sensible and the latent heat fluxes contribute to the total heat fluxes with up to -500 W m^{-2}. While the sensible heat flux is strongest close to the coast and then decreases south of Iceland over the Irminger Sea, the latent heat flux remains high over a very large area.

A composite of the heat and buoyancy fluxes during the wintertime (November through April) DWE shows a similar structure but with reduced amplitude (Figure 3-11). I find that the majority of the buoyancy loss over the Irminger Sea during the wind events is caused by the turbulent heat fluxes. Near the coast, there is a small negative contribution to the buoyancy flux from the outgoing longwave radiation and a small positive contribution from the incoming solar radiation. I note that there is a large uncertainty associated with the radiative heat fluxes of reanalyses in the Arctic [Walsh et al., 2009, Chaudhuri et al., 2014], but it is likely that they play a minor role during DWE compared to the turbulent fluxes.

Mean turbulent heat fluxes during DWE are $\sim$-400 W m^{-2} which is of the same

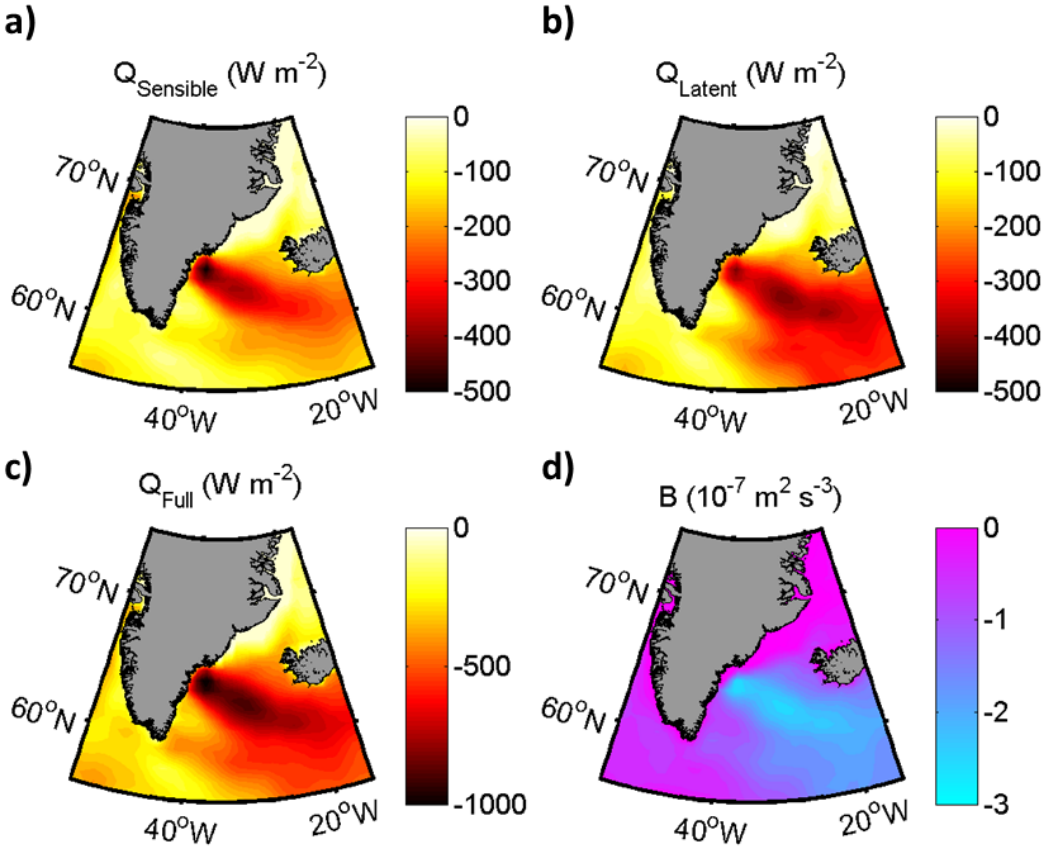

Figure 3-10: Snapshot of the sensible (a), latent (b) and total (c) heat fluxes from ERA-I for an individual DWE that occurred on 28 December 2004. The sensible and latent heat fluxes are the major contributors to the buoyancy loss (d) during this wind event.

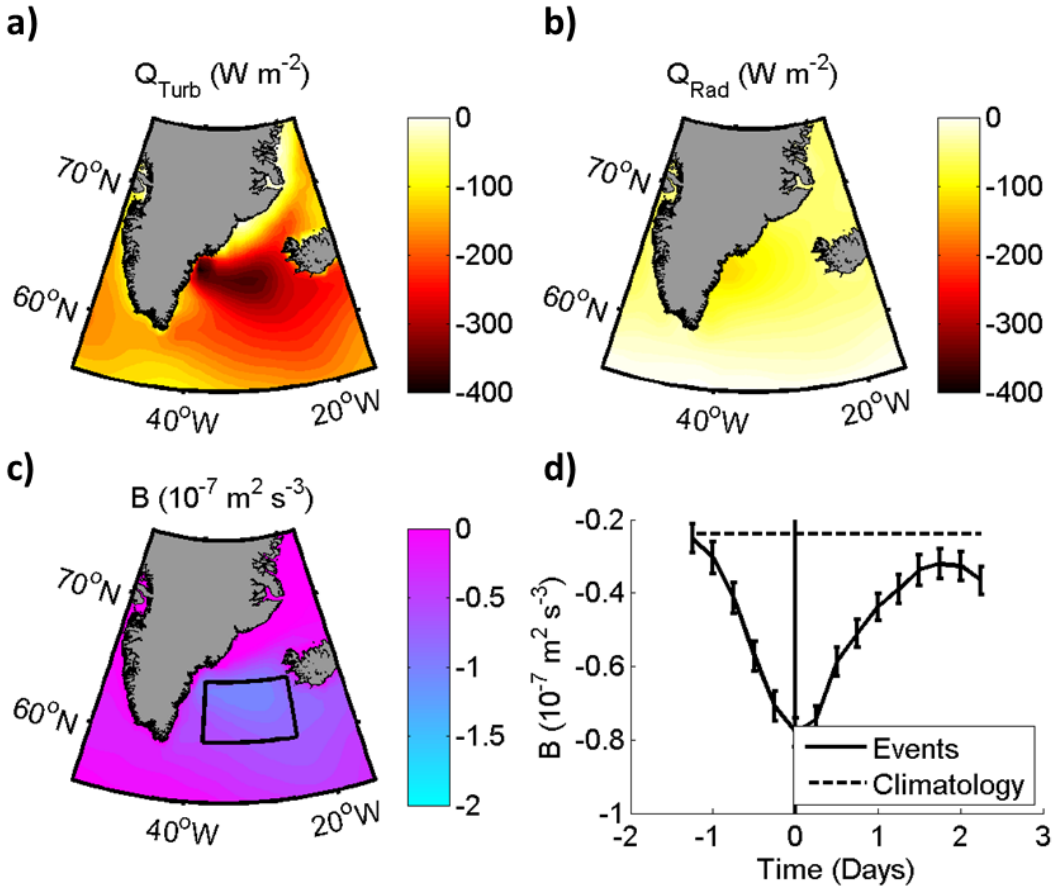

Figure 3-11: Composite of the turbulent (a) and radiative heat fluxes (b) of the wintertime (November through April) DWE. Again the turbulent heat fluxes are the major contributors to the buoyancy loss (c) of the wintertime DWE in ERA-I. (d) Composite of the ERA-I buoyancy flux evolution associated with all wintertime DWE over the Irminger Sea box shown in (c). 0 days indicates the time of the maximum wind speed. The climatological mean (November through April) is shown for reference. The duration of the enhanced buoyancy loss is almost three days.

order of magnitude as the turbulent heat fluxes that occur during tip jet events [Våge et al., 2009, Vage, 2010, Pickart et al., 2003a]. However, the region of maximum heat loss during tip jets is shifted southward compared to that during DWE as is the cyclone that is forcing DWE. I note that the two types of wind events can potentially be forced by the same synoptic system. Indeed, assuming that tip jets occur before DWE and allowing for a time lag of 2 days, I find that 31% of DWE are preceded by a tip jet (using the tip jet climatology from [Våge et al., 2009]).

To quantify the buoyancy loss associated with DWE, I use the box shown in Figure 3-11c. It covers a large part of the northern Irminger Sea, extends eastward over the Reykjanes Ridge and includes the northern most part of the Irminger Gyre in which convection is known to occur, as well as a part of the Irminger Current that is connected to the Gyre (e.g. Våge et al. [2011], Lavender et al. [2000]). The area captures a large signal of DWE but excludes most of the signal due to tip jets. Within this area, I find that the buoyancy flux associated with a DWE lasts for almost three days (Figure 3-11d). To estimate the buoyancy loss due to all 166 wintertime DWE ($\mathcal{B}_{DWE}$) I integrate the buoyancy flux from 30 hours before each event (i.e. the time of maximum wind speed) until 38 hours after each event over the box and sum all the events. Then, I compare it to the total wintertime buoyancy loss over the 32 years over the same area ($\mathcal{B}_{Clim}$):

$$\frac{\mathcal{B}_{DWE}}{\mathcal{B}_{Clim}} \approx 19\%.$$

Thus, summing the contributions from all DWE, I find that these wind events account for one fifth of the net buoyancy loss during winter even though they only span 9% of the time. I note that the buoyancy flux during DWE is due both to the downslope wind and the connected low pressure system with the associated winds.

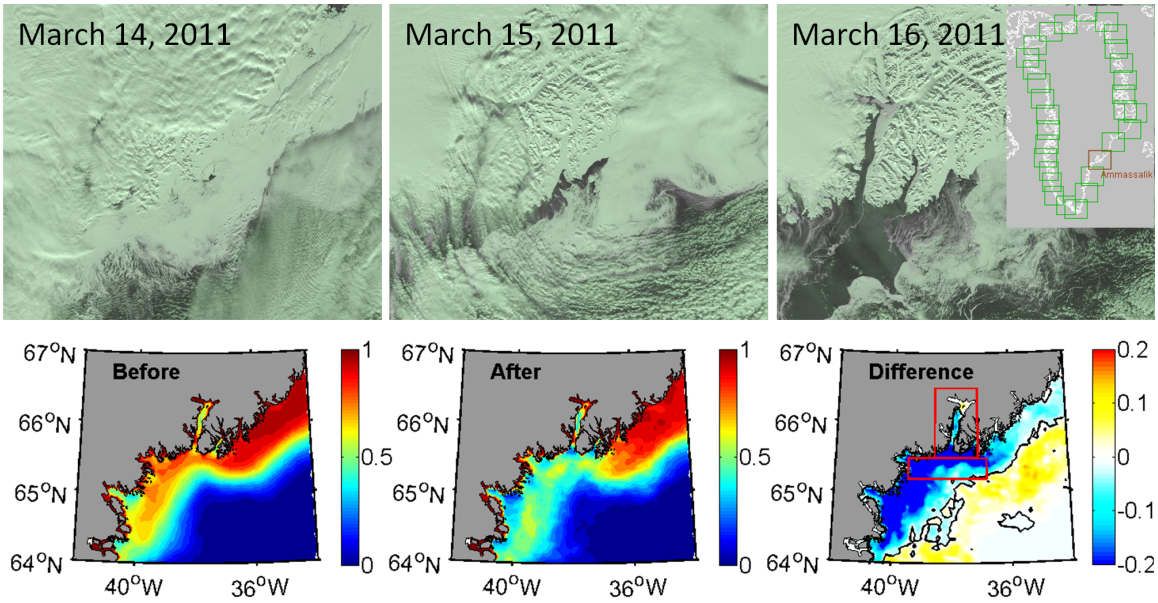

Figure 3-12: Top: Satellite images of a specific event in the visible range (MODIS) show how the ice is advected out of the fjord and away from the coast during the wind event. Bottom: Composite of satellite-derived (AMSR-E) mean sea ice concentration averaged during the week before the event, the day after the event, and the difference. Note the different color bar for the difference.

Impact on sea ice

To investigate the impact of DWE on the regional sea ice cover, I visually inspect MODIS visible images during individual events and analyze AMSR-E data for a composite of wind events. MODIS satellite images indicate that, during individual DWE, the sea ice is advected away from the coast, and the entire fjord - including the ice mélange - is cleared (e.g. Figure 3-12). Since cloud cover renders a thorough analysis using the visible wave band difficult, I use the AMSR-E sea ice concentration product (which is based on the 89 GHz channel) to determine the wind impact on the ice. Comparison of the sea ice during individual events shows that the AMSR-E satellite product is in good agreement with the MODIS satellite images.

Further analysis of the AMSR-E sea ice product shows that sea ice is normally present along the southeast Greenland coast between January and May. During these months and in the period from 2003 to 2010 (when AMSR-E is operating), I identify

32 DWE from the fjord station data. I study the impact of these events on the sea ice cover by comparing the mean sea ice distribution averaged during the week before the event with the sea ice distribution from the day after the event (Figure 3-12). The comparison clearly shows that during DWE ice is advected away from the coast. To quantify the sea ice reduction, I calculate the mean ice concentration before and after the wind event both inside the fjord and in a confined region of the surrounding shelf (regions shown in Figure 3-12). I find that, on the day after the wind events, the ice concentration inside the fjord is reduced by 29% while on the shelf it is reduced by 26%.

3.6 Discussion and Conclusions

I have built a composite of DWE, and thereby generalized previous case studies of individual events (e.g. Mills and Anderson [2003], Klein and Heinemann [2002], Heinemann and Klein [2002]). Most of the DWE investigated here correspond to SE events from the previous chapter. In the previous chapter, I have investigated the large-scale characteristics and dynamics of the wind events. In this chapter, I have described their local characteristics and dynamics, as well as their direct impacts. The identification and description of DWE is based on three different data sets, including two meteorological stations and the reanalysis product ERA-I. Despite the different characteristics of the data sets, the results agree well. DWE predominantly occur in winter and manifest themselves as strong winds in Ammassalik, including Sermilik Fjord. The large-scale flow converges inside the Ammassalik valley and forms a broad jet with peak wind speeds above 25 m s^{-1} and a height of 2500 m (in ERA-I). At the surface inside Sermilik Fjord, the fjord station records the fastest winds with speeds above 20 m s^{-1}. This could be an indication of the importance of the local topographic setting not fully resolved by ERA-I.

Moreover, I see evidence for a pronounced gravitational acceleration of the flow

in all three data sets. There is a distinct surface air temperature drop inside Sermilik Fjord indicating that cold (i.e. dense) air has been advected downslope, as is typical for katabatic flows. Also, vertical profiles from ERA-I show that the air over the ice sheet is strongly stratified, cold and dry, and the large temperature deficit over the ice sheet results in a strong gravitational acceleration. Another indication of the heat loss of the surface air and the stabilization of the boundary layer is the decrease in cloud cover during DWE recorded at the DMI station. The importance of the gravitational acceleration is further confirmed by an analysis of the momentum budget for a section along the downslope flow in ERA-I, as over the central part of the slope, the gravitational acceleration is one of the dominant driving forces.

All three data sets further show evidence of a larger scale synoptic forcing. Both meteorological stations record a drop in pressure prior to the wind event, and ERA-I sees a synoptic-scale cyclone between Iceland and Greenland such that the large-scale geostrophic flow is approximately in the same direction as the downhill topographic gradient. While the ambient pressure gradient accelerates the downslope flow over the upper slope, the flow becomes super-geostrophic near the coast, where the ambient pressure gradient is decelerating the flow. This deceleration is typical for flow over topography, which results in a horizontal pressure drag that first accelerates the near surface flow, but then decelerates it near the end of the slope where the isotherms rise again [Durran, 2003]. Near the surface, an additional deceleration likely results from the narrowing of the valley towards the coast, forcing the flow to move upwards.

Previous studies (e.g. Durran [1990]) suggest that downslope wind storms can be forced by mountain waves or a combination of katabatic flows and mountain waves [Poulos et al., 2000, 2007]. Gravity waves were also observed during a katabatic wind event in West Greenland [Heinemann, 1999] and Doyle et al. [2005] observed large-amplitude wave breaking during an individual DWE in Ammassalik. While ERA-I does resolve waves, these are mostly evanescent (both in the composite and in the event studied by Doyle et al. [2005]), which suggests that ERA-I only partially

resolves the wave dynamics of DWE. Thus, while ERA-I provides a realistic large-scale description of the events, further studies are needed to investigate the small-scale dynamics associated with DWE in more detail.

During DWE cold, dry air that found above the ice sheet spills over the ocean which results in a significant deepening of the boundary layer of the atmosphere and in a large buoyancy loss of the surface ocean. I estimate that the buoyancy loss due to the wintertime DWE and the associated cyclone is one fifth of the total wintertime buoyancy loss over a large part of the Irminger Sea. Mean heat fluxes during DWE, $\sim$-400 W m^{-2}, are comparable to those occurring during tip jet events, but they cover a different part of the Irminger Sea which is further north [Pickart et al., 2003a, Våge et al., 2009]. Peak heat fluxes can amount to -1000 W m^{-2}. For comparison with other convection regions Moore et al. [2002] find peak fluxes of about -500 W m^{-2} in the Weddell Polynya in Antarctica. Petersen and Renfrew [2009] use direct observations to calculate heat fluxes over Denmark Strait and the Irminger Sea during high wind speed conditions. They estimate the total heat flux to amount to -600 W m^{-2}, which is still less than what I find during extreme DWE. Moreover, the heat fluxes during DWE cover a wide area, even reaching south of Iceland. This is likely due to the large zonal extent of the cyclones at these latitudes. Most of the buoyancy loss occurs over the Irminger Current which flows around the Irminger Gyre where deep convection occurs (e.g. Våge et al. [2011], Pickart et al. [2003b], de Jong et al. [2012]). Thus, DWE have a large potential for preconditioning or driving convection.

Finally, I find that DWE significantly reduce the coastal sea ice cover (Figure 3-12). I estimate a 29% reduction of sea ice inside Sermilik Fjord and a 26% reduction on the surrounding shelf compared to the mean sea ice concentration the week before the event. The advection of sea ice offshore likely results in a faster melting of the sea ice due to the warm water in the interior Irminger Sea [Sutherland et al., 2013] and thus to a local freshening of the Irminger Sea. Considering that DWE could occur all along the East Greenland coast, their combined offshore advection of sea ice could

be substantial [Dodd et al., 2012]. It is possible that this offshore advection of sea ice could result in a significant freshwater transport into the interior. Assessing its magnitude is not trivial because of the lack of ice thickness data but should be the focus of future studies.

In addition, the removal of sea ice affects the energy balance of the surface water since sea ice has insulating properties and influences the amount of sunlight reaching the water surface. The removal of ice from Sermilik Fjord may explain why the sea ice cover in Sermilik Fjord is often mobile, even in winter. Further, it has been found that a dense ice cover (sea ice and icebergs) near outlet glaciers is important for the glacier stability [Amundson et al., 2010] and that reductions in the ice cover correlate with the glacier's retreat [Howat et al., 2010, Walter et al., 2012]. Thus, DWE in Ammassalik and Sermilik Fjord could have an impact on the stability of Helheim Glacier.

Chapter 4

The role of wave dynamics and small-scale topography for downslope wind events in southeast Greenland

A modified version of this chapter is currently in press in the Journal of the Atmospheric Sciences. The authors are M. Oltmanns, F. Straneo, H. Seo and G. W. K. Moore. ©American Meteorological Society. Used with permission.

4.1 Abstract

In Ammassalik, in southeast Greenland, downslope winds can reach hurricane intensity and represent a hazard for the local population and environment. They advect cold air down the ice sheet and over the Irminger Sea where they drive large ocean-atmosphere heat fluxes over an important ocean convection region. Earlier studies have found them to be associated with a strong katabatic acceleration over the steep coastal slopes, flow convergence inside the valley of Ammassalik, and — in one instance — mountain wave breaking. Yet, for the general occurrence of strong downslope wind events, the importance of mesoscale processes is largely unknown.

Here, two wind events, one weak, one strong, are simulated with the atmospheric weather research and forecasting (WRF) model with different model and topography resolutions, ranging from 1.67 km to 60 km. For both events, but especially the strong one, it is found that lower resolutions underestimate the wind speed because they misrepresent the steepness of the topography and do not account for the underlying wave dynamics. If a 5 km instead of a 60 km model resolution in Ammassalik is used, the flow associated with the strong wind event is faster by up to 20 m s^{-1}. The effects extend far downstream over the Irminger Sea resulting in a diverging spatial distribution and temporal evolution of the heat fluxes. Local differences in the heat fluxes amount to 20% with potential implications for ocean convection.

4.2 Introduction

Downslope winds in southeast Greenland can reach hurricane intensity, posing a threat to the local population and environment [Rasmussen, 1989, Born and Boecher, 2000, Klein and Heinemann, 2002, Heinemann and Klein, 2002, Mernild et al., 2008]. They are especially pronounced within the valley of Ammassalik where the large-scale synoptic flow is funneled by the topography. The wind events advect cold dry air over the ocean and are associated with a large heat loss over the Irminger Sea, an important ocean convection region. In the preceding chapter, I constructed a composite of strong downslope wind events (DWE) using the ERA-Interim reanalysis (ERA-I) from the European Center for Medium-Range Weather Forecasts (ECMWF) and local weather stations. Compared to the weather stations, ERA-I underestimated the local wind speed of DWE, never reaching the hurricane intensity that is sometimes observed in the local town [Rasmussen, 1989, Born and Boecher, 2000, Mernild et al., 2008]. This suggests that the reanalysis does not resolve the full dynamics underlying these winds events. The notion that a higher model resolution is necessary to accurately simulate wind speed is in line with previous studies of tip jets and barrier winds in southeast

Greenland [DuVivier and Cassano, 2013]. Thus, in this chapter I will investigate the small-scale dynamics of strong downslope wind events across the southeast coast.

One possible mechanism by which downslope winds can be extremely accelerated is due to mountain waves [Smith, 1985, Durran, 1986, Bacmeister and Pierrehumbert, 1988]. These develop when stratified air is forced over a topographic barrier. According to the Eliassen-Palm theorem mountain waves are associated with a downward momentum flux that is transferred to the topography by the cross-mountain pressure drag [Eliassen and Palm, 1961, Durran, 2003]. When they attain sufficiently large amplitude they can break and overturn. This results in a strongly divergent momentum flux profile such that there is a significant deceleration of the mean flow in the wave breaking region and acceleration of the downslope flow below. Indeed, during one DWE in Ammassalik, dropwindsondes and aircraft measurements depict the breaking of a large-amplitude mountain wave [Doyle et al., 2005]. While ERA-I did reproduce this wind event, it did not resolve the mountain wave. This suggests that model resolution affects the ability to resolve some of the leading order dynamics and thereby influences the magnitude of the simulated wind speed.

Mountain waves and mountain wave breaking are not only associated with downslope wind storms, but can influence atmospheric dynamics on many scales, including the general atmospheric circulation and climate [Fritts and Alexander, 2003]. The effects of wave drag and fluxes on the momentum balance play an important role in determining the structure of the large-scale flow in the troposphere and lower stratosphere [McFarlane, 1987]. Furthermore, the large vertical momentum fluxes and turbulence facilitate the vertical mixing of water vapor, aerosols and chemical species [Dörnbrack and Dürbeck, 1998], thus affecting the chemical properties of the atmosphere. In addition, the clear air turbulence that develops in regions of mountain wave breaking represents a significant hazard to aviation [Ralph et al., 1997, Clark et al., 2000]. Encounters of aircraft turbulence were associated with mountain waves also over west Greenland [Lane et al., 2009]. These potentially important con-

sequences motivate examining mountain wave breaking with the general occurrence of DWE in Ammassalik.

In this chapter, I will investigate the role played by processes that are unresolved by the 80 km grid spacing of the reanalysis and how they interact with other terms in the momentum balance. Specifically, I simulate two DWE, one weak, one strong, with the weather research and forecasting (WRF) model using different model and topography resolutions to study the small-scale dynamics in Ammassalik and their effects on larger scales. Here, and in the following, I use the term 'small-scale' to characterize processes that are resolved using a grid spacing between 5 km and 20 km. In numerical models, the energy in the highest resolved wave numbers tends to be overly damped. Therefore, the model's effective resolution is defined as the scale at which the model's kinetic energy spectrum decays relative to the observed spectrum [Skamarock, 2004]. Previous stimulations with the WRF model have shown that the effective resolution is $\sim$7 times the grid spacing [Skamarock, 2004], and thus I expect a model with a grid spacing of 5 km (60 km) to resolve processes on scales of 35 km (420 km) which lie within the meso-β (meso-α) scale [Orlanski, 1975].

The questions that I will address in this chapter are therefore:

- What are the small-scale dynamics that can create winds of hurricane intensity in Ammassalik?

- How important is the resolution of the model and that of the topography to capture these dynamics?

- What are the large-scale conditions that result in strong wind events? Specifically, do the small-scale dynamics amplify only strong large-scale flows or also weaker ones?

- How far does the influence of the small-scale dynamics extend on the large scale (e.g. with regard to the heat fluxes)?

The chapter is separated into four parts. First, I describe the characteristics of the two wind events and investigate how they are represented by different model resolutions. In the second part, I study the dynamics by comparing individual driving forces in the momentum balance and assess the role played by small-scale momentum fluxes. I also consider the case in which the model is run at high resolution but with a smoothed topography. The results indicate that the lower resolutions underestimate the wind speed because they do not account for the underlying wave dynamics that contribute to accelerate the downslope flow. When the topography is smoothed, the cross-mountain pressure drag associated with the mountain wave is reduced resulting in a smaller downward momentum flux and overall lower wind speeds even if the model resolution is unchanged. In the third part, I analyze interactions between the mountain wave and the gravitational acceleration and study how they are affected by model resolution. Finally, I look at the evolution of the downslope flow and investigate what the impact of using a higher model resolution for the downslope wind events is on the larger scales of motions. I show that the downstream wind field is affected by small-scale processes within the Ammassalik valley. The effects extend further out over the Irminger Sea with consequences for the distribution and magnitude of the ocean-atmosphere heat fluxes and thus — potentially — ocean convection.

4.3 Background

Physically, mountain wave induced wind storms can be understood in terms of hydraulic theory. On the upstream side of the mountain, the flow is accelerated because of the pressure gradient acceleration associated with the mountain wave. When the wave breaks on the downslope side of the mountain, a hydraulic jump-like phenomenon occurs and the flow transitions from a wave dominant (or subcritical) regime to a supercritical regime. In the supercritical regime, the flow is further accelerated by the gravitational acceleration [Durran, 1990]. In hydraulic theory, the

Froude number $Fr = \frac{u}{\sqrt{gD}}$ describes the regime of a fluid with depth D and velocity u. g is the gravitational acceleration. Froude numbers above (below) 1 correspond to the supercritical (subcritical) regime. For a continuously stratified atmosphere, a Froude number analog $Fr = \frac{u}{NH}$ is often defined to classify atmospheric flows. In this case, H is the mountain height, N is the Brunt-Väisälä frequency, and u a suitably defined upstream wind speed.

Mountain waves and gravity flows are not independent phenomena as they can interact with each other. Based on idealized simulations, Poulos et al. [2000] find that radiative cooling can enhance the mountain wave flow speed in the lee for Froude numbers up to 0.75. For Froude numbers above $\sim$0.5 the gravity current can be scoured such that the mountain wave flow penetrates to the surface while for Froude numbers less than $\sim$0.5 the katabatic flow and the mountain wave couple, resulting in a complex mutually interdependent evolution [Poulos et al., 2000, 2007]. While mountain waves can influence the intensity, depth and local variability of katabatic winds through turbulence and dynamic pressure perturbations [Mursch-Radlgruber, 1995, Jin et al., 1996, Poulos et al., 2000], the stability and reduced turbulence of a lower stratified layer can in turn affect the dynamics of mountain waves [Scorer, 1967, Poulos et al., 2000]. Thus, the effects of potentially unresolved mountain wave processes in ERA-I during DWE could amplify through interactions with the gravity current.

4.4 Data and Method

In order to compare the effect of using different resolutions, I simulate two wind events with the WRF model (Version 3.5) [Michalakes et al., 2004, Skamarock et al., 2005], one of which is weak and the other one strong compared to the composite of DWE described in the previous chapter. The wind events, also seen by local weather stations, were mainly identified with a condition on wind speed. Both events

are associated with a wind and sea level pressure field whose general structure is representative of the composite. The strong wind event occurred on 3 February 1999 with maximum surface wind speeds of 28 m s^{-1} at 18:00 UTC in ERA-I, and the weak one occurred on 9 April 2007 with maximum surface wind speeds of 21 m s^{-1} at 6:00 UTC in ERA-I (Figure 4-1). ERA-I obtained these wind speeds inside the valley of Ammassalik near the coast, but not directly at the weather station location where wind speeds of 32.5 m s^{-1} and 16.5 m s^{-1} were observed during the strong and weak wind event respectively (see Figure 4-1 for station location). Both wind events are simulated on a 60 km resolution domain (WRF60) with two nests, one with a 20 km resolution (WRF20), and one with a 5 km resolution (WRF5), leaving all other model parameters unchanged (Figure 4-1).

I run three simulations. In the first case, I use one-way nesting, which allows to compare the effect of using four different resolutions within the inner most domain boundaries. In the second case, I use two-way nesting such that feedbacks from the WRF5 and WRF20 domains are allowed. In the third case, the nesting is again one-way and I use a topography with a resolution of 60 km also in the WRF5 and WRF20 domains. It is obtained by linearly interpolating the 60 km resolution topography in WRF60 to the additional grid points in the 20 km and 5 km domains. In each simulation, I use 30 vertical sigma levels, the highest being at 50 hPa. The level distribution (shown in Figure 4-3) is surface intensified to yield a good vertical resolution near the surface. Physics parameterizations are specified in Table 4.1. They were chosen based on current knowledge of their efficiency and accuracy as well as their suitability under snow and ice conditions [Janjic et al., 2011]. The simulations are run for 24 hours, starting 12 hours before the time of maximum wind speed in ERA-I. ERA-I provides the boundary and initial conditions. Due to the short simulation period of 24 hours, the initial conditions are the dominant factor influencing the dynamics and internal model variability is less important. If I start the simulations six hours earlier or use different aspect ratios for the domains, the results do not change appreciably.

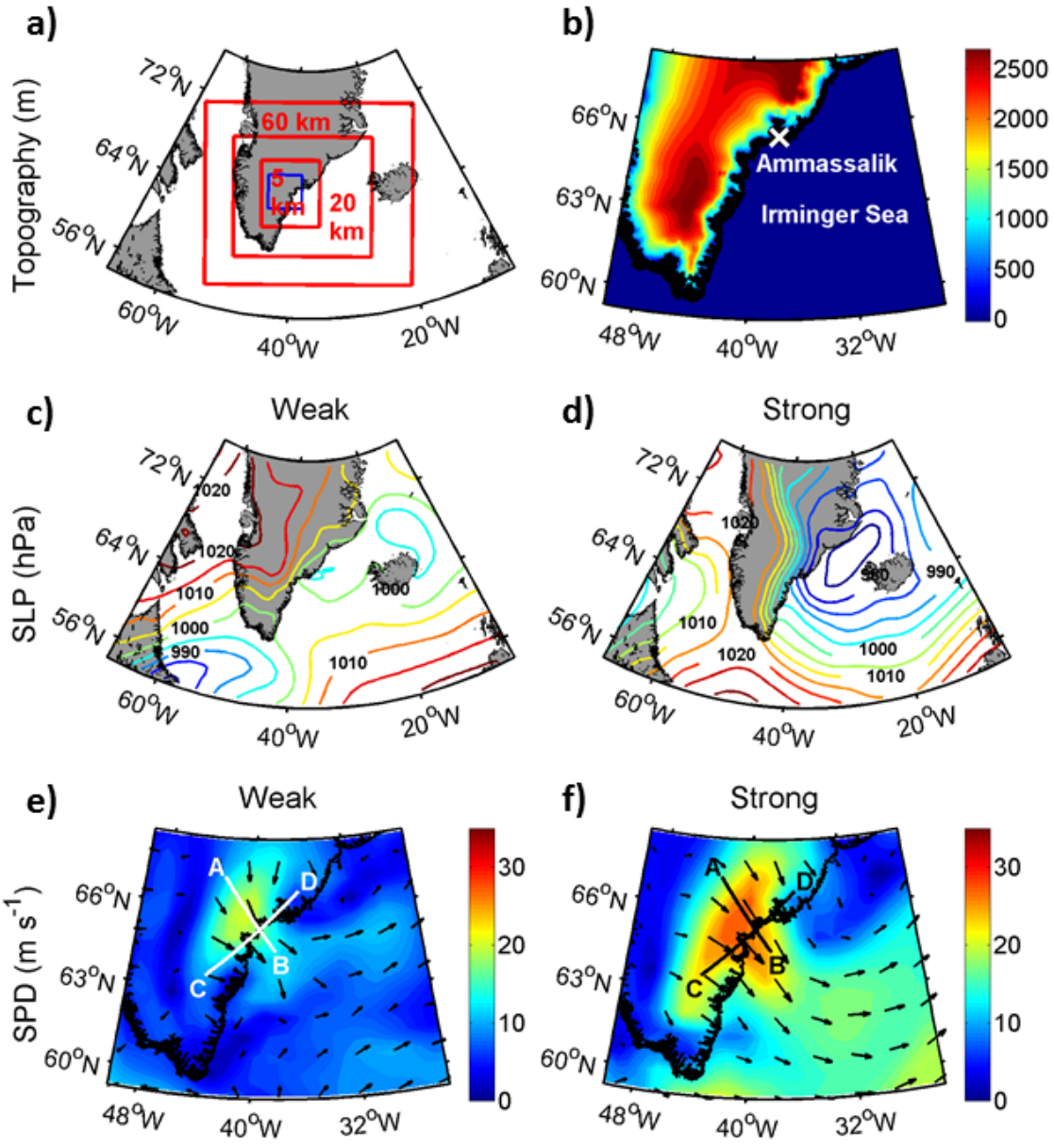

Figure 4-1: a) WRF simulation domains: The blue line delineates the 1.67 km resolution domain; b) Topography (m) in southeast Greenland including the valley of Ammassalik. The white cross indicates the location of the DMI station location; (c,d) SLP (hPa) and (e,f) wind speed (m s^{-1}) for the weak event in ERA-I on 9 April 2007 and the strong wind event on 3 February 1999 respectively. The lines mark the sections shown in Figures 4-3 and 4-4.

Variable	Scheme
Micro-Physics	WRF-Single-Moment-Microphysics scheme class 3 (WSM3) [Hong et al., 2004]
Longwave Radiation	Rapid Radiation Transfer Model (RRTM) [Mlawer et al., 1997]
Shortwave Radiation	Dudhia scheme [Dudhia, 1989]
Surface Layer	Revised MM5 Monin-Obukhov scheme [Jiménez et al., 2012]
Land-Surface Model	Unified Noah land-surface model [Chen and Dudhia, 2001]
Boundary-Layer	YSU PBL scheme [Hong et al., 2006]
Cumulus Parametrization	Kain-Fritsch cumulus convection scheme [Kain and Fritsch, 1990]

Table 4.1: WRF model physics specifications that are used for the three simulations.

As a 5 km horizontal resolution could potentially misrepresent non-hydrostatic waves and alias energy into larger-scale hydrostatic waves [Reinecke and Durran, 2009], an additional simulation was carried out with a third nest with a horizontal grid spacing of 1.67 km (WRF1.7) and 45 vertical levels. Most of the analysis is based on the WRF60 and WRF5 domains. The 1.67 km resolution domain extends over the central part of the Ammassalik valley and was only used for comparison with the WRF5 domain to assess the importance of smaller scale non-hydrostatic waves that can be unresolved in WRF5.

The reanalysis product ERA-I [Dee et al., 2011] from the European Center for Medium-Range Weather Forecasts (ECMWF) has been described in detail in chapter 2. The data have a 6 hourly temporal resolution, 60 vertical levels in the model's terrain following vertical coordinate and a horizontal resolution of approximately 80 km at the surface. A comparison between ERA-I and the 2011 reprocessed QuikSCAT ocean wind vectors with an improved geophysical model function [Ricciardulli and Wentz, 2011] during DWEs from 2000 to 2009, in the previous chapter, showed that ERA-I captures the structure of the wind field well but underestimates the wind speeds by $\sim$1 to 2 m s^{-1} over the ocean in the region of the peak wind speeds. This

is expected as DWE have a comparably small scale and very high wind speeds, two conditions in which reanalyses often have problems [Renfrew et al., 2009b]. One potential explanation for the different wind speeds is the coarse resolution of the reanalysis. Thus, in the following I will investigate how strongly model resolution affects the simulation of DWE.

4.5 Results

4.5.1 Characteristics

To test the influence of model resolution on the wind event characteristics, I first investigate the surface wind field in WRF60, WRF20 and WRF5 in the one-way nesting simulation at the time when they record the maximum wind speed. For this purpose, I determine the location of the maximum wind speed in the three domains, only requiring it to be within the boundaries of WRF5 and north of 64°N, and analyze the wind speed evolution at this location (Figure 4-2). For both events, the location where the maximum wind speed occurs is similar in WRF5, WRF20 and WRF60 (Figure 4-2). The higher the resolution is, the closer this location is to the coast. Compared to the lower resolution domains, WRF5 has a finer structure (Figure 4-2). The largest differences are seen near the coast in the southern part of the valley and in the outflow region. The outflow onto the shelf is narrower in WRF5 with two distinct minima in wind speed next to it. Thus, the differences in the obtained wind speed between the domains occur not only over land, where the topographic resolution likely has a strong influence on the surface winds, but are carried downstream over the ocean. The differences are more pronounced for the strong wind event, but they also exist for the weak one.

Next, I compare the evolution of the wind field in the different domains at the location where they obtain the maximum wind speed. For the strong event, WRF5 obtains wind speeds that are $\sim$5 m s^{-1} higher than in WRF20 and $\sim$10 m s^{-1} higher

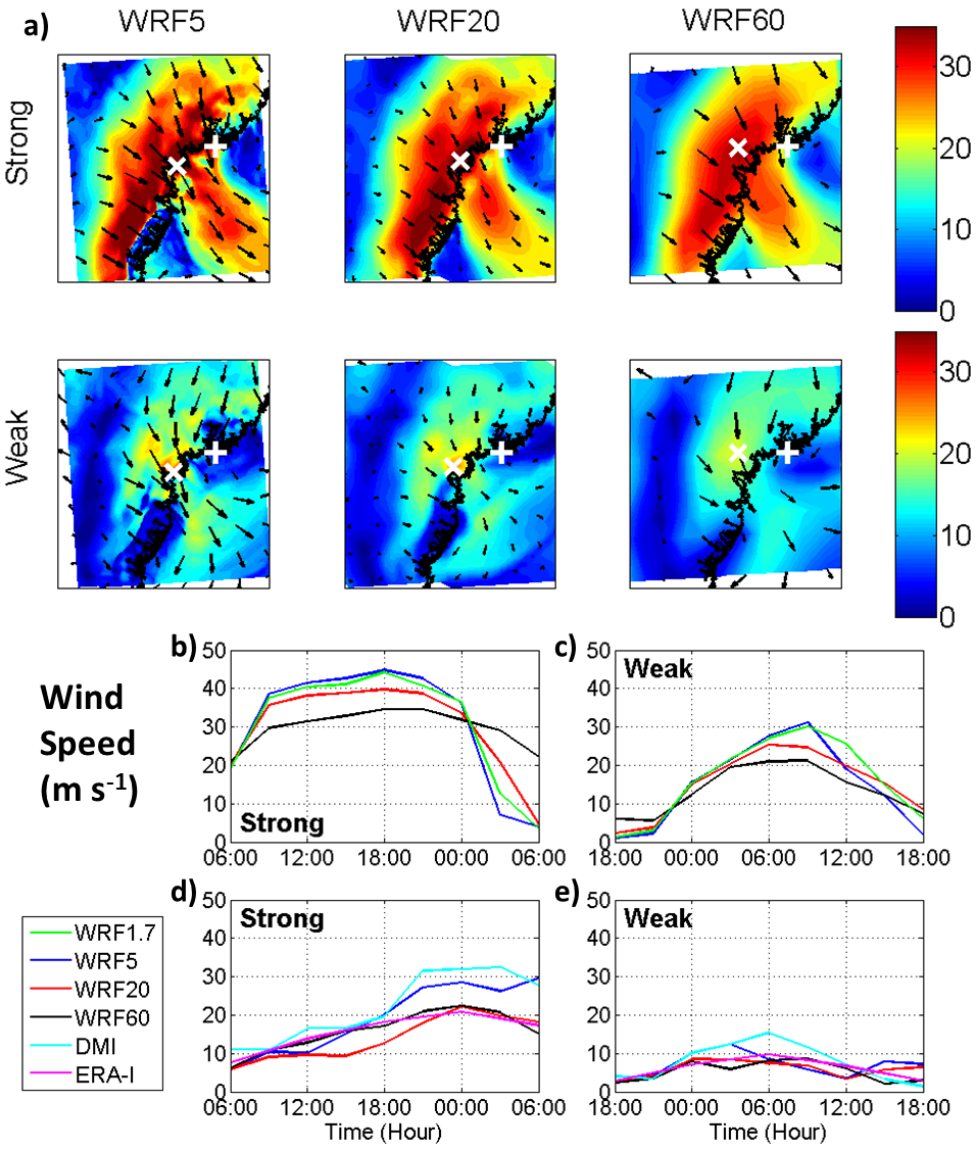

Figure 4-2: (a) Surface wind speeds in the 5 km resolution domain (WRF5), 20 km resolution domain (WRF20), and 60 km resolution domain (WRF60) for the strong (top) and the weak (bottom) wind events (Figure 4-1) at the time when each of these products records the maximum wind speed. The white cross indicates the location where the maximum wind speed occurs in the respective simulation and the white plus marks the location of the DMI station location. (b,c) Comparison of the wind speed evolution in WRF60, WRF20 and WRF5 at their locations of maximum wind speed, and the wind speed evolution in the 1.67 km resolution domain (WRF1.7) at the location where WRF5 obtains the maximum wind speed. (d,e) Comparison of the wind speed evolution in WRF5, WRF20 and WRF60 with the observed wind speed at the DMI station location.

than in WRF60. For the weak wind event, WRF5 also obtains higher wind speeds, but the difference with WRF20 and WRF60 is smaller. The fastest winds reach speeds of 45 m s^{-1} during the strong event and 30 m s^{-1} during the weak event. Also, WRF5 obtains a more rapid initial increase of the wind speed during the strong wind event and a more rapid decrease after the maximum wind speed has been reached. Thus, the wind speed time series in WRF60 has a broader and flatter temporal evolution compared to WRF5, which could be related to both an overall different wind speed evolution and the slight shift in location of maximum wind speed (Figure 4-2).

I also compare the surface wind fields between WRF1.7 and WRF5 at the time when WRF5 obtains the maximum wind speed (not shown). Within the WRF1.7 domain, the distribution and magnitude of the surface wind speed is almost identical to WRF5. The largest differences occur at confined locations in the outflow region at the coast and are of the order of 2 m s^{-1} for the strong event and 3 m s^{-1} for the weak event. For both events, the wind speed evolution in WRF1.7 and WRF5 at the location where WRF5 obtains the maximum wind speed agree very well (Figure 4-2), and the locations where the maximum wind speeds are obtained are close to each other.

At the location of the DMI weather station (just outside the WRF1.7 domain, see Figures 4-1 (b) or 4-2 for station location), WRF5 agrees best with the observed wind speed, especially during the strong wind event (Figure 4-2). For the weak event, WRF5, WRF20 and WRF60 obtain similar wind speeds. All three domains capture the low-frequency evolution of the wind event, but record a faster wind speed drop off than is observed. A possible reason for the discrepancy between the model and the observations is the sharp gradient in the wind speed field near the station location such that a slight variation in the temporal evolution of the front can result in very different wind speeds at the weather station. Other reasons could include inaccuracies in the boundary conditions — despite the fact that the weather station data is assimilated in the reanalysis — errors resulting from the interpolation to the

station location, and a misrepresentation of the complex topography in this region. In the following, I will mostly show results from the strong wind event. For the weak event, the winds and its underlying driving forces are reduced, but the differences between WRF5, WRF20 and WRF60 remain.

Vertical sections along and across the flow confirm that the wind speed is larger the higher the resolution is (Figures 4-3 and 4-4). WRF5 resolves two distinct regions of steep topography at the southwestern side of the valley, each associated with a wind speed maximum of up to 60 m s^{-1} that intermingle in the coarser resolution domains (Figure 4-3). The cross-sectional flow (represented by the arrows in Figure 4-3) is entering the valley at both sides near the surface which is likely due to channeling by the topography. There is more vertical and horizontal wind shear in the wind field in WRF5 and a highly variable potential temperature field across the valley compared to the coarser resolutions. In WRF20 this variability is strongly reduced and WRF60 almost does not see it at all. The differences between the domains are largest inside and along the edges of the valley with differences of 10 to 20 m s^{-1}. They do not only occur near the surface where the different resolutions result in different representations of the topography, but they also extend up higher into the troposphere. If the model is run with a 60 km resolution topography everywhere, the wind speed in WRF5 is still higher compared to WRF60, but reduced compared to the WRF5 domain with the 5 km topography, especially near the surface. The potential temperature field in WRF5 with the 60 km resolution topography (WRF5-Topo60 hereafter) is closer to the one in WRF60 than to the one in WRF5 with the 5 km topography. This shows that both small-scale topography and atmospheric structure play an important role during the wind events.

Using a higher resolution has a large effect on the slope along the valley, especially close to the coast (Figure 4-4). The biggest differences in the wind speed between WRF5, WRF20 and WRF60 amount to $\sim$20 m s^{-1} and occur near the surface where the slope is steepest. The potential temperature field in WRF5 suggests that the

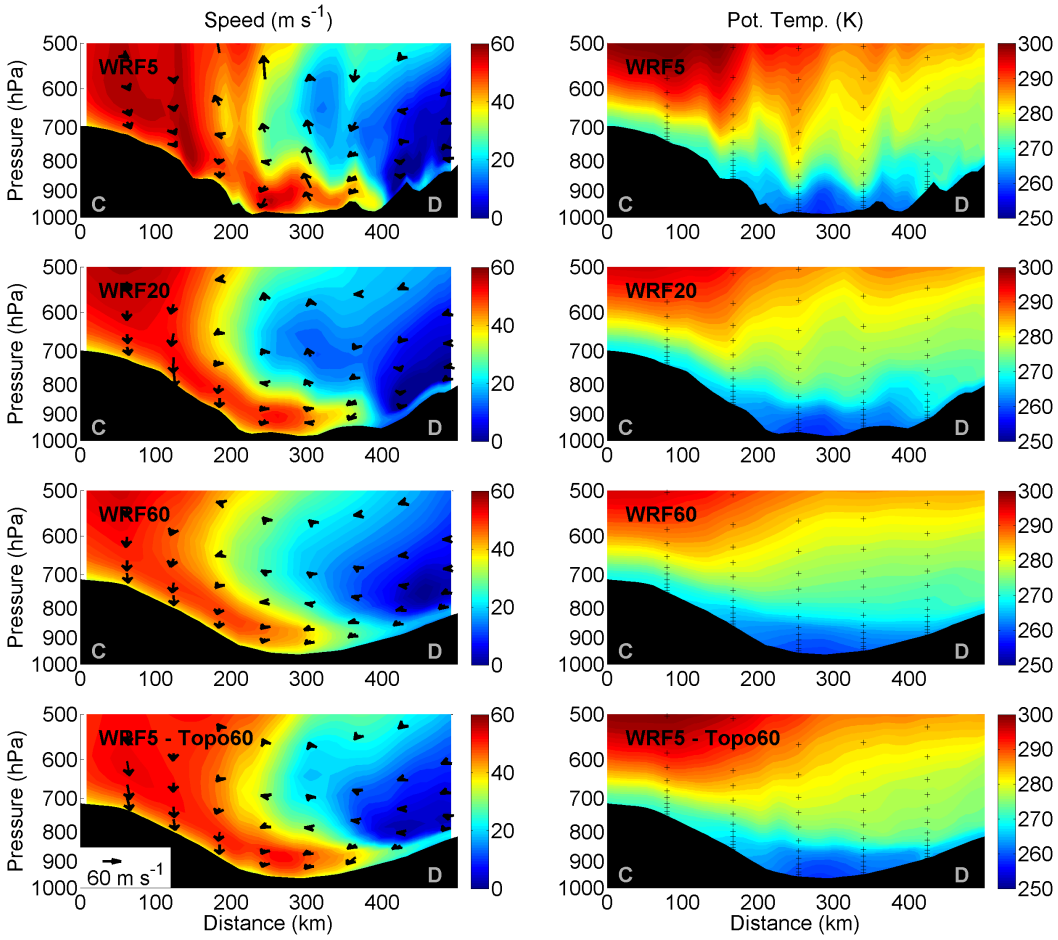

Figure 4-3: Comparison of the flow field and potential temperature in the 5 km (WRF5), 20 km (WRF20) and 60 km resolution domains (WRF60) across the section CD in Figure 4-1. The filled contours show the component of the flow across the section whereas the arrows represent the flow along this cross section. Only a few arrows are shown. The reference arrow is representative of the horizontal direction only. The vertical direction is rescaled according to the axis limits. WRF5-Topo60 indicates the case where the model resolution is 5 km and the topographic resolution is 60 km. Black crosses overlaid on the temperature field indicate the positions of the vertical model levels at selected locations across the valley.

high wind speeds over the slope are associated with a steep mountain wave that is underrepresented in WRF20 and largely smoothed out in WRF60 (Figure 4-4). In the WRF5-Topo60 case the wind speeds are still higher compared to WRF60, but again they are smaller compared to WRF5 with the 5 km topography, and the wave in the potential temperature field is smoothed.

A comparison between WRF1.7 and WRF5 shows, that the representation of the topography is similar in both domains, and over the slope the wind speed and potential temperature profile in WRF5 and WRF1.7 agree well. The obtained isentropic slopes are very similar, and the mountain wave over the slope has approximately the same wave length of $\sim$50 km. The largest differences between WRF1.7 and WRF5 occur downstream of the coastline, where WRF1.7 resolves larger vertical velocities that are associated with a series of lee waves that are smoothed in WRF5. Such lee waves are a typical signature of downslope wind storms with a lower stable layer. They radiate energy away when the surface flow recovers towards ambient conditions [Durran, 1990].

For the weak event, the overall wind speeds are smaller, but the profiles show the same graduation in wind speed and isentropic slopes between WRF5, WRF5-Topo60, WRF20 and WRF60. This suggests the existence of dynamical differences both between different resolution domains, and between the smoothed and regular topography simulations. I will investigate these differences in the next section.

4.5.2 Momentum balance

To study the dynamical differences, I evaluate each term in the momentum balance for the downslope flow and investigate how it is affected by model resolution. To a good approximation, the atmospheric lapse rate is linear between 2500 and 6000 m height. Below about 2000 m, the temperature gradient is larger and the near surface air is significantly colder than above. Thus, I split the temperature into an ambient part θ_0, which is obtained by linearly extrapolating the temperature

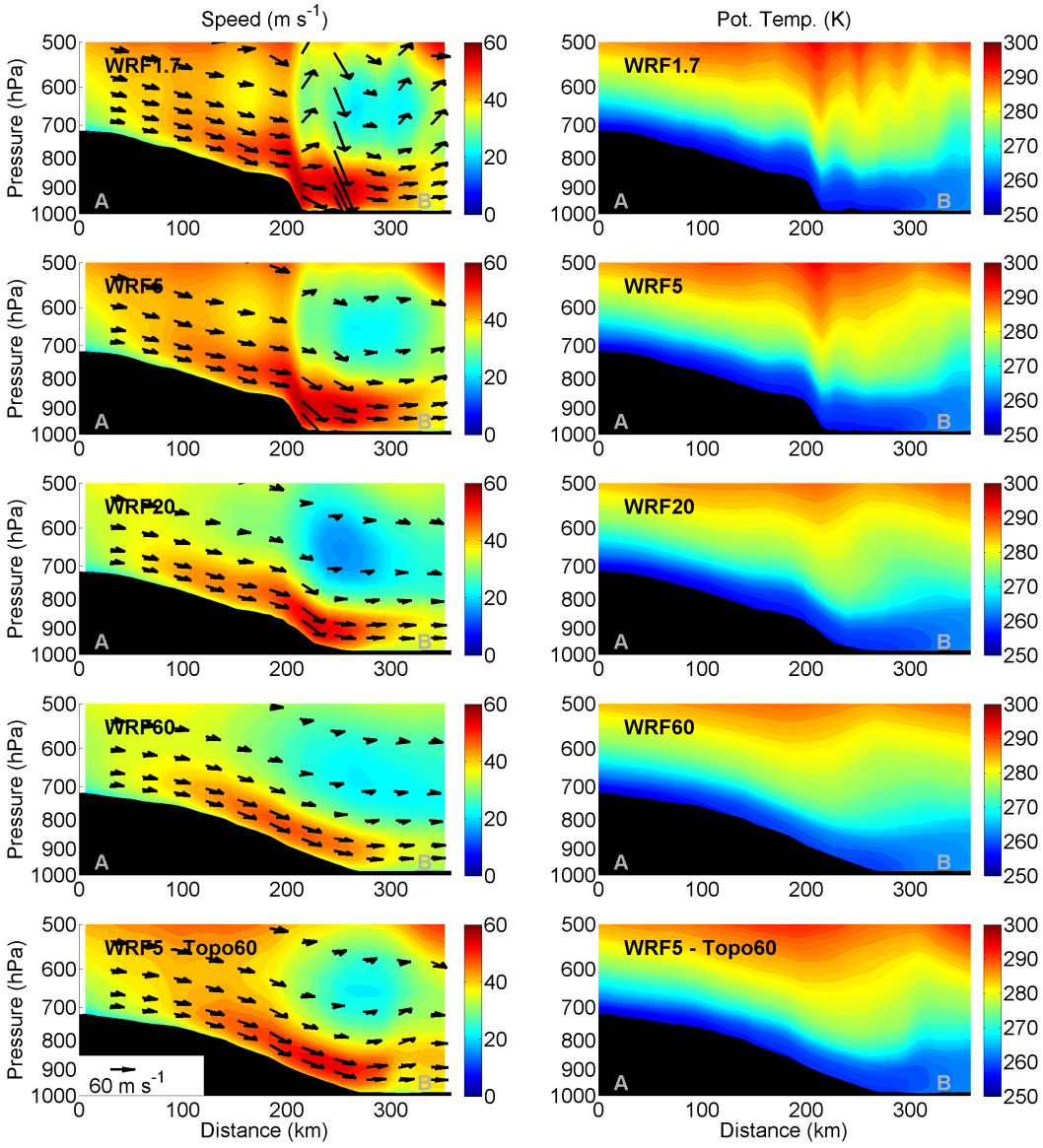

Figure 4-4: Comparison of the flow field and potential temperature in the 1.67 km (WRF1.7) 5 km (WRF5), 20 km (WRF20) and 60 km resolution domains (WRF60) along the section AB in Figure 4-1. Shown is the component of the flow along the section. The reference arrow is representative of the horizontal direction only. The vertical direction is rescaled according to the axis limits. WRF5-Topo60 indicates the case where the model resolution is 5 km and the topographic resolution is 60 km.

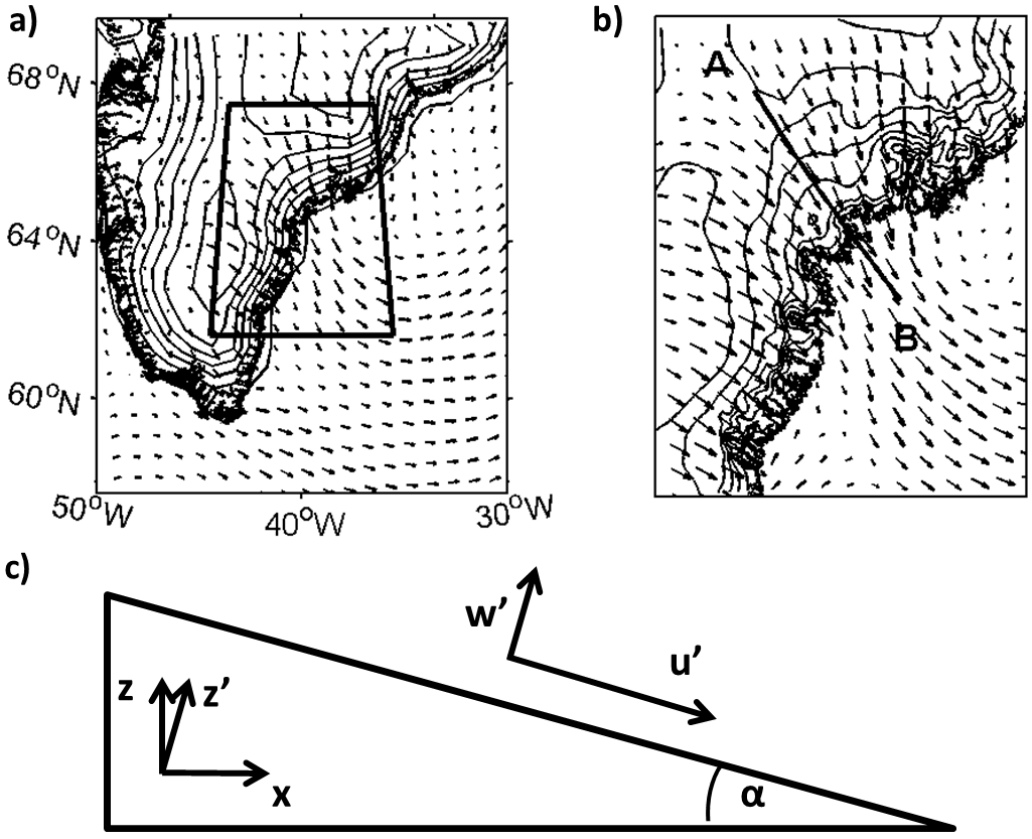

Figure 4-5: Topography in the WRF60 (a), and the WRF5 domain (b) with surface velocity vectors overlaid. Only a few arrows are shown. The contour interval is 400 m. c) Schematic of the coordinate system used for the analysis of the momentum balance (Figure 4-6).

between 2500 m and 6000 m to the surface, and a temperature deficit part θ, which is defined as the deviation from the linear temperature lapse rate such that a positive temperature deficit indicates that the air in this layer is colder than the ambient air at the same height. Using higher bounds for the definition does not change the results. This procedure has also been applied by other studies on katabatic winds [Mahrt, 1982, Parish and Cassano, 2001, 2003, van Angelen et al., 2011] and I verified that that the splitting is meaningful for each time step and model domain by confirming that the temperature lapse rate is approximately linear above 2500 m. An example of this splitting can be seen in Figures 4-9 (a) and 4-10 (a) for different time steps. I analyze the momentum balance along the same section AB that is shown in Figures 4-1 and 4-5. This section goes right through the valley where the wind speed is maximum and the slope steepest and thus, I expect this section to show the largest differences between the resolutions. As in Chapter 3, I assume that the temperature and pressure perturbations associated with the temperature deficit layer are much smaller compared to those associated with the ambient atmosphere ($\theta \ll \theta_0$ and $p \ll p_{amb}$, where p is the pressure due to the temperature deficit and p_{amb} is the pressure in the ambient atmosphere corresponding to θ_0). In addition, I use the hydrostatic and the Boussinesq approximation. Under these approximations, the momentum balance in the downslope direction x and in the model's vertical coordinate (Figure 4-5) can be expressed as:

$$\begin{aligned} &\frac{\partial u'}{\partial t} + u'\frac{\partial u'}{\partial x}\,|_{z'}\cos(\alpha) + v\frac{\partial u'}{\partial y} + w'\frac{\partial u'}{\partial z'} - fv = \\ &\frac{g}{\theta_0}\theta\sin(\alpha) - \cos(\alpha)\,\frac{g}{\theta_0}\frac{\partial \hat{\theta}}{\partial x}\,|_{z'} - \frac{1}{\rho_0}\frac{\partial p_{amb}}{\partial x}\,|_z + F_{Res}, \end{aligned} \tag{4.1}$$

$$F_t + F_{NL} + F_C = F_G + F_T + F_S + F_{Res}. \tag{4.2}$$

ρ_0 is density, f is the Coriolis parameter, g is gravity and α is the positive angle of

the slope with respect to the horizontal. $\hat{\theta}(z)$ is the vertically integrated temperature deficit from z to some arbitrary height z_t, which is chosen above the boundary layer where the temperature deficit vanishes:

$$\hat{\theta}(z) = \int_{z}^{z_t} \theta dz. \tag{4.3}$$

In Equation 4.2 the total horizontal pressure gradient force (F_P) is split into an ambient pressure gradient acceleration F_S, the gravitational acceleration F_G, and the thermal acceleration F_T. The splitting between F_T and F_G arises from the rotation of the coordinate system in the downslope direction. The gravitational acceleration represents the acceleration due to the presence of a temperature deficit layer over sloping terrain. The ambient pressure gradient acceleration describes the acceleration due to pressure gradients in the ambient atmosphere, thus ignoring the deficit layer. Mountain wave effects are included mostly in this term. The thermal acceleration is due to temperature variations within the deficit layer. It is comparable to the coastal sea-breeze effect [Estoque, 1961, Simpson, 1994] and exists even in the absence of the slope.

I calculate F_S, F_T, the local acceleration F_t, nonlinear advection F_{NL} and F_G explicitly at 21:00 UTC and infer sub-gridscale dynamics (F_{Res}) from the residual. The ambient pressure gradient acceleration within the boundary layer can be calculated using hydrostatic balance and integrating the ambient potential temperature gradient downwards [Cassano and Parish, 2000, Van den Broeke et al., 2002, van Angelen et al., 2011]. I verified that the flow is in hydrostatic balance by evaluating the vertical momentum equation for the ambient and the full atmosphere in each domain along the section AB. Even in WRF1.7, the hydrostatic terms are approximately one order of magnitude larger than their difference and several orders of magnitude larger than the advective terms and local acceleration. Thus:

$$\frac{1}{\rho}\frac{\partial p_{amb}}{\partial x}\mid_z = \frac{1}{\rho}\frac{\partial p\,(z_t)}{\partial x}\mid_z + R_g \int_{\ln p(z)}^{\ln p(z_t)} \left(\frac{p}{p_0}\right)^{\frac{R_g}{c_p}} \frac{\partial \theta_0}{\partial x}\mid_p d\ln p, \tag{4.4}$$

$$\frac{1}{\rho}\frac{\partial p_{amb}}{\partial y}\mid_z = \frac{1}{\rho}\frac{\partial p\,(z_t)}{\partial y}\mid_z + R_g \int_{\ln p(z)}^{\ln p(z_t)} \left(\frac{p}{p_0}\right)^{\frac{R_g}{c_p}} \frac{\partial \theta_0}{\partial y}\mid_p d\ln p, \tag{4.5}$$

where R_g is the gas constant and c_p is the heat capacity at constant pressure. Under non-hydrostatic conditions, the total horizontal pressure gradient within the temperature deficit layer would consist of an additional term due to non-hydrostatic pressure effects $F_{NH} = F_P - F_T - F_G - F_S$ which can also include inaccuracies resulting from the differentiation in F_P. I find that this term is approximately one order of magnitude smaller than F_S and F_G, which is consistent with the results from the previous chapter. Moreover, it is insensitive to resolution which agrees with previous studies on downslope winds [Cassano and Parish, 2000]. In order to compare the forces in WRF5 and WRF60 on the same scales, and to remove the high-frequency variability associated with the mountain wave in WRF5, I smooth them over a distance of 120 km. Other filter sizes give the same result as long as they smooth out local variability associated with the wave in WRF5. The forces are shown in Figure $4-6$ apart from the local acceleration which is negligible.

Qualitatively, the obtained forces during both events agree with the ones obtained from ERA-I during the composite of DWE in the previous chapter, indicating that the events are representative of the composite. I find that all forces have a larger magnitude in WRF5 compared to WRF60. The biggest differences occur in the dominant terms F_G, F_S and F_{NL}. F_S is initially accelerating the wind but as the flow approaches the coast, it inhibits the surface flow. Both the acceleration and the deceleration are more pronounced in WRF5 than in WRF60 with differences above 20%. The difference in the magnitude of F_G is similarly large. In both domains, it is the largest accelerating force over the central part of the slope. F_{NL} is mostly responding

to the other forces. It can be split into a horizontal along-slope, a horizontal cross-slope and a vertical component. The horizontal components are large and positive at the surface of the slope and negative above, whereas the vertical component is negative at the surface and positive above (Figure 4-8). This is in line with previous studies which suggest that the horizontal momentum flux of the intense surface flow is balanced by vertical advection of momentum [Durran, 1986, Bacmeister and Pierrehumbert, 1988]. In these studies, however, the horizontal momentum advection includes mostly the along-slope component. For both wind events here, I note that the cross-slope horizontal component is similarly large (Figure 4-7), likely because of confluence of the flow inside the valley. This stresses the importance of 3D effects for the wind events.

F_{Res} has a similar magnitude in WRF5 and WRF60. It includes effects of subgrid-scale turbulence that are parametrized in the model, numerical inaccuracies resulting from the differentiation, as well as the local tendency of the momentum which is not fully included in the local acceleration due to the coarse temporal sampling of three hours. Since F_{Res} has a similar magnitude in WRF5 and WRF60, there is little or no parametrization of the nonlinear effects on scales between 5 and 60 km. Thus, there is no gravity wave drag parametrization which is currently not supported for simulations of this duration and resolution in the WRF model. Close to the surface, where friction is important, F_{Res} is strongly decelerating the flow. Above the surface, it is negligible except over the steepest part of the slope above the surface layer where it is accelerating the flow. Since this region corresponds to a local minimum in wind speed (Figure 4-4) the acceleration could result from drag by the faster flow around it. The local acceleration (not shown) and the thermal acceleration are relatively unimportant compared to the other forces, both in WRF5 and WRF60. For the WRF5-Topo60 case (not shown), the magnitude of the forces is larger compared to WRF60 (especially for F_G, F_S and F_{NL}) and smaller compared to WRF5.

Previous studies have explained strong surface wind speeds by large vertical mo-

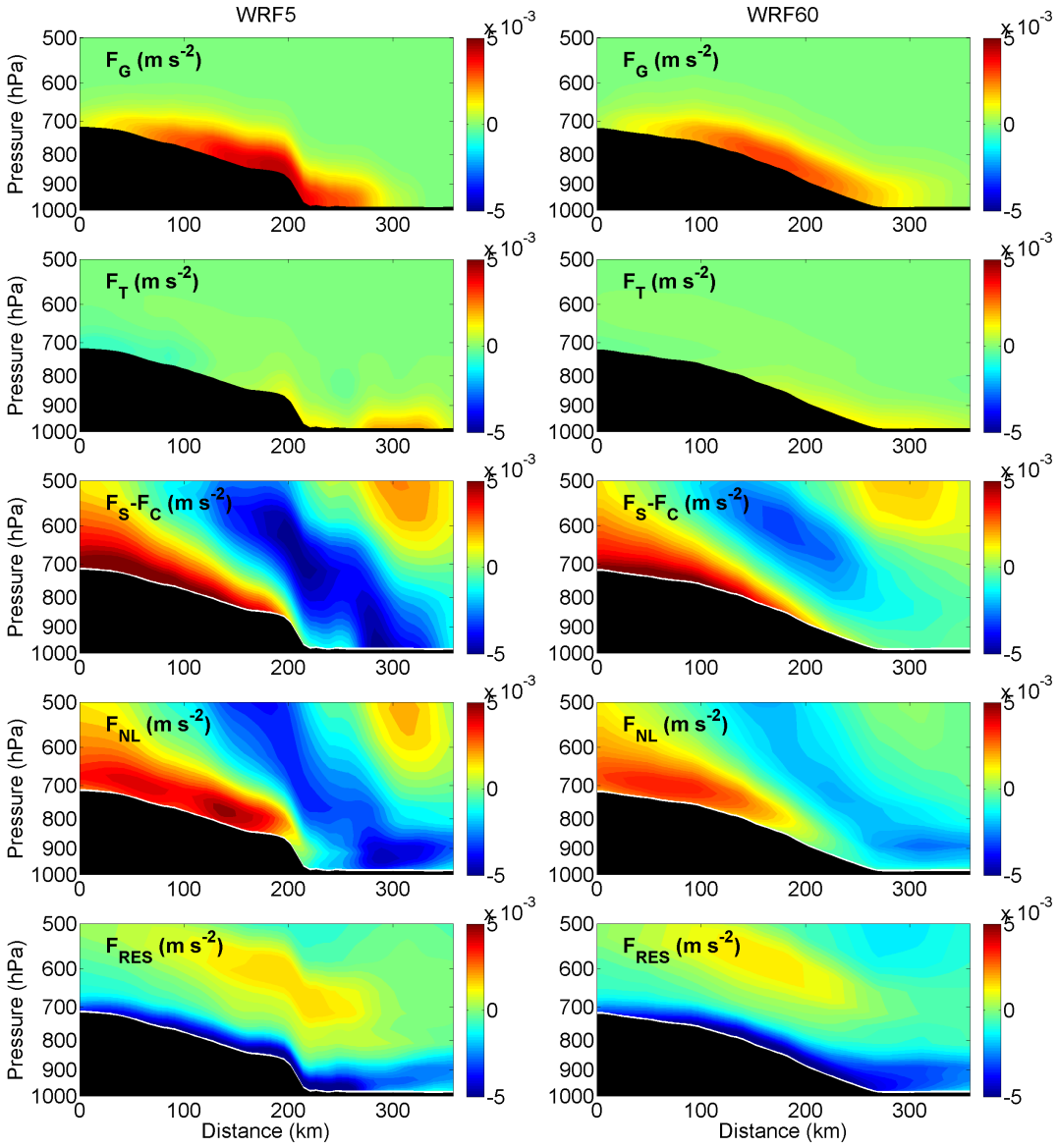

Figure 4-6: Accelerations during the strong event in WRF5 and WRF60 along the section AB shown in Figure 4-1. Shown are the gravitational acceleration F_G, thermal acceleration F_T, ambient pressure gradient and Coriolis acceleration $F_S - F_C$, nonlinear advection F_{NL} and the residual F_{Res} at 21:00 UTC. F_{NL} appears on the left-hand side of Equation 4.2 and is mostly balancing the pressure gradient terms. The forces are smoothed over 120 km to eliminate the small-scale variability associated with the mountain wave and to compare WRF5 and WRF60 on the same scale.

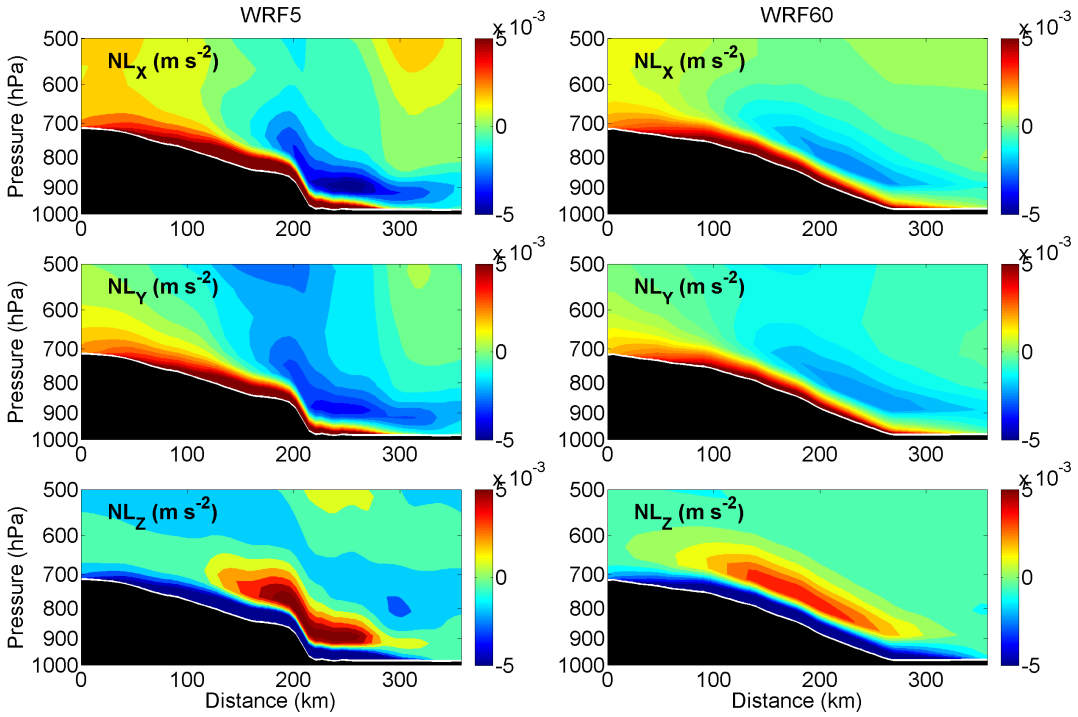

Figure 4-7: Along-slope NL_X, cross-slope NL_Y and vertical component NL_Z of the nonlinear advection term for the strong event at 21:00 UTC in WRF5 and WRF60 along the section AB shown in Figure 4-1. The advection terms are smoothed over 120 km to eliminate the small-scale variability associated with the mountain wave and to compare WRF5 and WRF60 on the same scale.

mentum fluxes associated with mountain waves [Durran, 1986, Bacmeister and Pierrehumbert, 1988, Durran, 2003]. To directly assess the importance of momentum fluxes on the scales not resolved in WRF60, I decompose the (unrotated) flow into a mean and a wave component: $u = \overline{u} + u^*$ and similarly for w. I define the mean as a running mean over 120 km on the model levels and the wave component as deviations of the flow from the mean. Thus, by definition, the wave component in WRF60 is negligible. In WRF5, WRF60 and WRF5-Topo60 momentum converges over the slope above the surface (Figure 4-8). In WRF5 the wave component of the vertical momentum flux ($NL'_Z = \overline{w^* \frac{\partial u^*}{\partial z}}$) can be almost twice as large as the mean component ($\overline{NL_Z} = \overline{w} \frac{\partial \overline{u}}{\partial z}$). The mean component of the vertical momentum flux in WRF5 also has a larger magnitude than the total vertical momentum flux in WRF60, and thus these wave processes have a large impact on the mean flow. In the WRF5-Topo60 case, the magnitude of the total vertical momentum flux is reduced compared to WRF5, but larger compared to WRF60. The wave component is very small despite the 5 km model resolution, emphasizing the role of the topography in setting the scale of the dynamics (Figure 4-8).

4.5.3 Mountain wave - gravity current interaction

The results from the previous section indicate that the driving forces of the downslope flow have a different magnitude in WRF5 and WRF60 even on scales greater than 120 km (Figure 4-6). Apart from the differences in the nonlinear advection, the largest differences between the domains occur in the ambient pressure gradient and the gravitational acceleration. Given the importance of the steep slope for the cross-mountain pressure drag, the different representation of F_S in WRF5 and WRF60 is expected. F_G on the other hand depends only on the height difference of the two end points of the part of the slope over which it is averaged as well as the temperature deficit. Both quantities are not directly affected by the resolution when averaged over the slope. Thus, the only way by which F_G can attain a different magnitude in

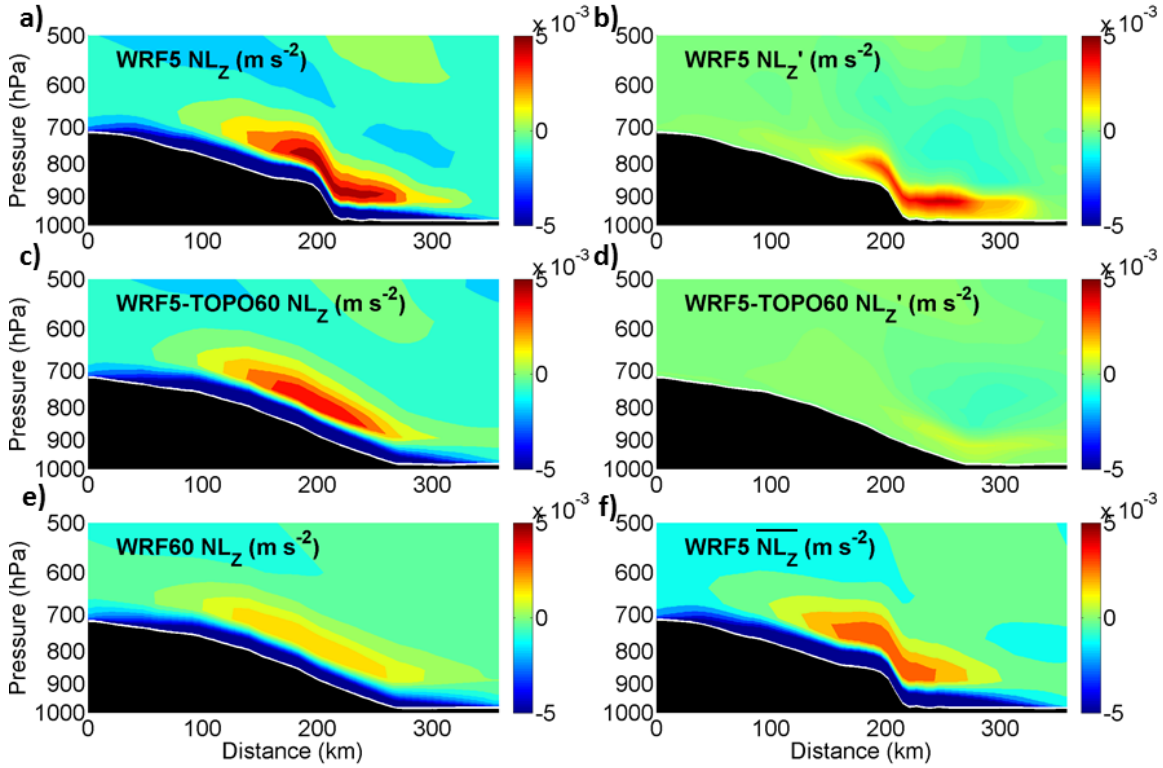

Figure 4-8: Mean and wave parts of the vertical component of the momentum flux along section AB (Figure 4-1) at 21:00 UTC. a,c,e) Total vertical momentum flux in WRF5, WRF5-Topo60 and WRF60 respectively; b,d) Wave component of the vertical momentum flux ($\overline{w^* \frac{\partial u^*}{\partial z}}$) in WRF5 and WRF5-Topo60 respectively; f) Mean component of the vertical momentum flux in WRF5 ($\overline{w} \frac{\partial \overline{u}}{\partial z}$).

WRF5 and WRF60 is by nonlinear effects when the temperature deficit is increased at exactly those locations where the slope is steeper in the higher resolution domain, and by feedbacks with the other forces e.g. when a faster flow results in more cold air advection which in turn intensifies the temperature deficit and F_G.

Interactions between gravitationally driven flows and mountain waves have been studied by Poulos et al. [2000, 2007] for different Froude number regimes. Using an upstream wind speed of 30 m s^{-1} for the strong wind event, a stability of $N = 0.02$ s^{-1} and a mountain height of 3000 m, the Froude number is close to 0.5 for the strong wind event. For the weak wind event, the upstream wind speed is $\sim$20 m s^{-1} and N is comparable to the strong wind event, resulting in a Froude number of $\sim$0.33. The higher Froude number for the strong wind event is associated with a mountain wave separation point that is shifted downhill. The mountain wave separation point delimits the region where the mountain wave dominates the flow. According to Poulos et al. [2000, 2007] the coupling of the katabatic wind with the mountain wave downstream of the separation point can deepen the temperature deficit layer by turbulence relative to the case without mountain waves. Indeed, for both wind events, I find very deep deficit layers of more than 1000 m (e.g. Figure 4-9). Another effect of mountain waves on katabatic flows arises from pressure perturbations that are induced by the gravity waves above the temperature deficit layer [Poulos et al., 2000, 2007]. I find this is true for both wind events, as the temperature deficit is not distributed evenly over the slope. In WRF5 the temperature deficit increases more quickly over the steeper parts of the slope which results in a larger gravitational acceleration in WRF5 compared to WRF60 and the difference increases with time as more cold air is advected onto the slope (Figure 4-9). Thus, the mountain wave - katabatic wind interaction leads to a stronger gravitational acceleration in WRF5 compared to WRF60.

Poulos et al. [2007] suggested that mountain waves and katabatic winds can sometimes become indistinguishable and inseparable. Despite the close interaction between

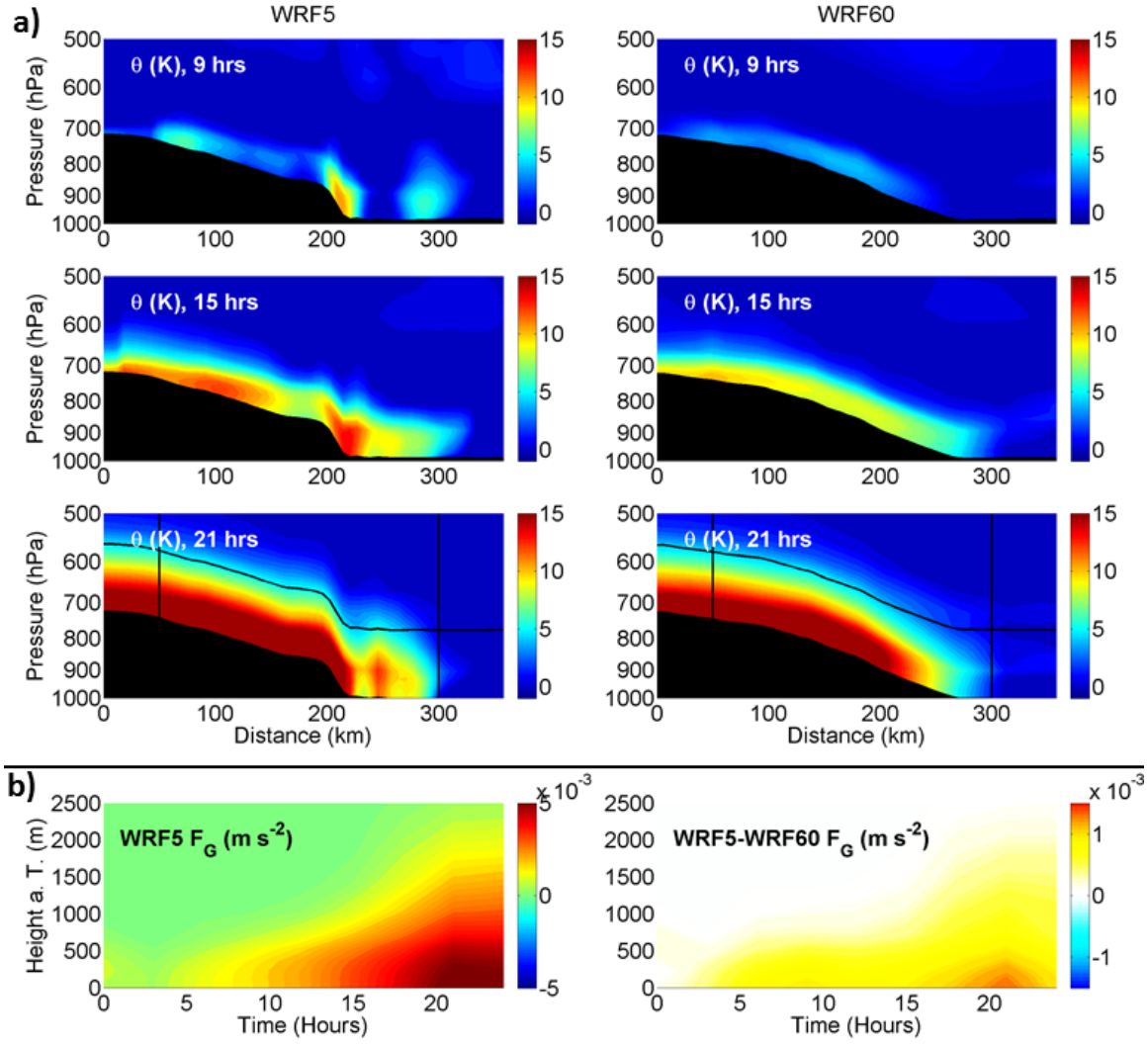

Figure 4-9: a) Evolution of the temperature deficit along section AB (Figure 4-1) at three different time steps during the simulation of the strong wind event for WRF5 and WRF60. In WRF5 the temperature deficit intensifies faster, especially over the steeper parts of the slope which results in a larger gravitational acceleration. The lines at 21 hrs delineate the location of the ten lowest model levels and region between 50 and 300 km that is used for the averaging in Figure 4-11. b) Evolution of the gravitational acceleration averaged between 50 and 300 km in WRF5 and the difference between WRF5 and WRF60. The difference increases with time.

them, I still note that the splitting of the total pressure gradient force into F_G and F_S is meaningful at each time step. As the simulation of the strong wind event progresses, a cold air pool forms at the end of the slope which extends deep into the atmosphere. Thereby, F_S decreases and is decelerating the flow at the end of the slope. The region where F_S is negative, shifts further upslope as more cold air is advected downslope. Thus, there is a negative feedback between the stronger flow and the decreasing ambient pressure gradient force (Figure 4-10) and this feedback is more pronounced in WRF5. In summary, for the strong wind event the temperature profile develops first large vertical gradients when the deficit layer intensifies and then large horizontal gradients. The former process accelerates the flow as described by F_G and the latter decelerates the flow as described by F_S.

For the weak event, the gravitational acceleration is initially larger than the ambient pressure gradient acceleration. Since the Froude number is smaller, the katabatic component of the flow is more pronounced [Poulos et al., 2000]. While the downslope wind speed increases, a wave develops over the slope but it is shallower compared to the strong wind event and the separation point is shifted upslope. The development of the wave is associated with an increase of the ambient pressure gradient acceleration. Meanwhile, the temperature deficit layer mixes with ambient air and the stratification and thus F_G decrease (not shown). To summarize the evolution of the differences in WRF5 and WRF60 for the strong and the weak wind events, I average the forces over the ten lowest model levels between the distances of 50 and 300 km over the slope (see Figures 4-9 and 4-10). The results are insensitive to the vertical extent of the lower layer and the distance over which I average. For the strong wind event, the magnitude of the forces is larger compared to the weak wind event and the evolution diverges between WRF5 and WRF60. For the weak event, the differences between WRF and WRF60 remain small (Figure 4-11).

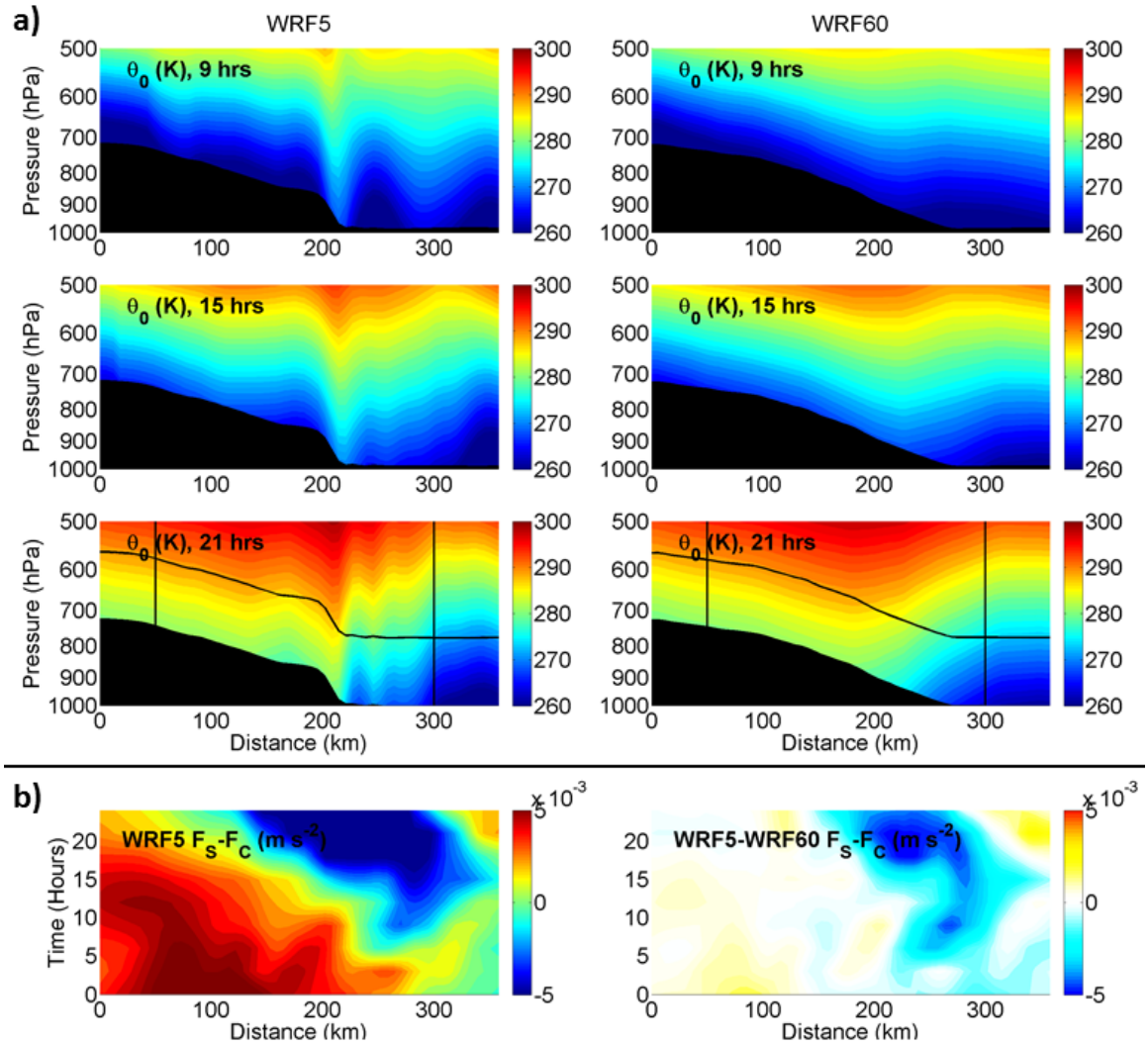

Figure 4-10: a) Evolution of the ambient temperature along section AB (Figure 4-1) at three different time steps during the simulation of the strong wind event for WRF5 and WRF60. The advection of strongly stratified air over the ocean results in a decelerating horizontal pressure gradient in WRF5 and WRF60 which is more pronounced in WRF5. The lines at 21 hrs delineate the location of the ten lowest model levels and region between 50 and 300 km that is used for the averaging in Figure 4-11. b) Evolution of the ambient pressure gradient acceleration averaged over the 10 lowest model levels in WRF and the difference between WRF5 and WRF60. Note that the axes are different from the ones in Figure 4-9 b. The decelerating effect of the pressure gradient force is seen further upslope with time and intensifies.

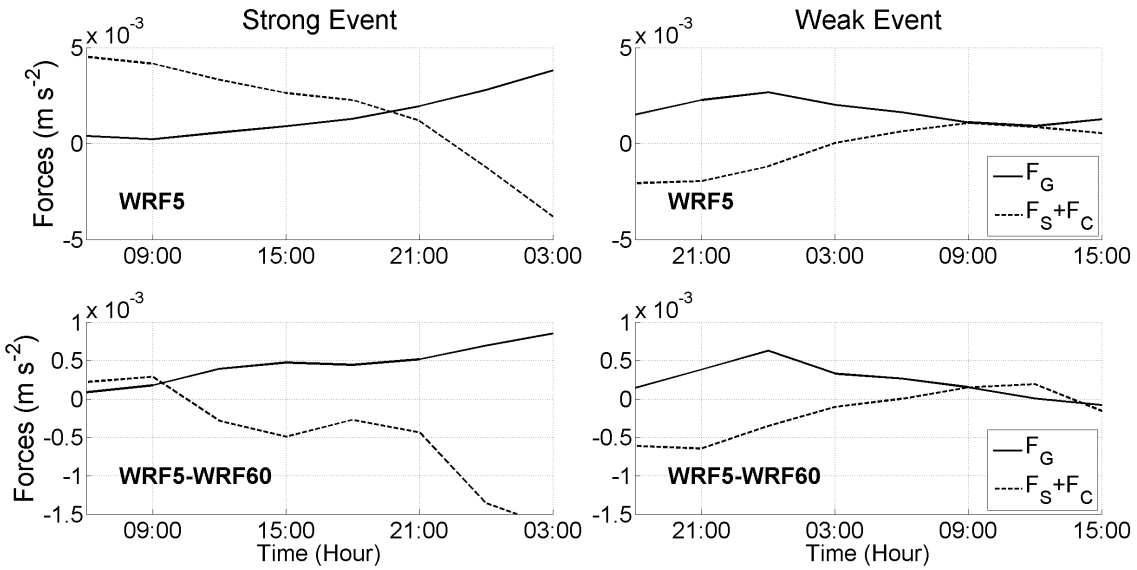

Figure 4-11: Evolution of the ambient pressure gradient and Coriolis acceleration and the gravitational acceleration averaged over the 10 lowest model levels and the region between 20 and 300 km over the slope along section AB in Figure 4-1. The region over which is averaged is shown in Figures 4-9 and 4-10. Shown are the evolutions for the strong and the weak wind event in WRF5 and WRF60, as well as their differences (WRF5 - WRF60).

4.5.4 Effects on larger scales

Next, I investigate how far downstream the effects of using a higher resolution extend, and compare the evolution of the surface pressure, temperature, wind speed and total turbulent heat fluxes in the simulations with the one- and the two-way nesting. Thus, I compare these fields in WRF60 from the simulation when feedbacks from WRF5 and WRF20 are included with the one from the simulation that does not allow for feedbacks (Figure 4-12). I do not expect the simulations to diverge due to intrinsic model variability since they are still strongly controlled by the initial conditions within the simulation period of 24 hours. Again, for the strong wind event the differences are more pronounced compared to the weak one (not shown) and they quickly increase with time. If feedbacks are included, the pressure is lower in the outflow region of the Ammassalik valley and higher northeast of it over the Irminger Sea. Near the East Greenland coast this results in a narrowing of the shape of the low pressure system. In addition, the surface air in the outflow region of the valley (Figure 4-2) is colder by $\sim$2 K, and the winds are faster by $\sim$5 m s^{-1} downstream of Ammassalik. This has consequences for the turbulent heat fluxes which amount to 1000 W m^{-2} and are up to 200 W m^{-2} larger in the region of the highest wind speeds and up to 200 W m^{-2} weaker south of this region. Positive heat fluxes indicate that heat is transferred from the ocean to the atmosphere. Thus, differences between the one- and the two-way nesting simulations are not confined to the valley in Ammassalik, but extend downstream over the Irminger Sea where they result in a different spatial distribution and temporal evolution of the heat fluxes.

4.6 Discussion and conclusion

In this chapter, I have investigated the role of small-scale dynamics and steep topography for strong downslope wind events (DWE) in southeast Greenland and their downstream effects. Specifically, I have simulated a strong and a weak wind

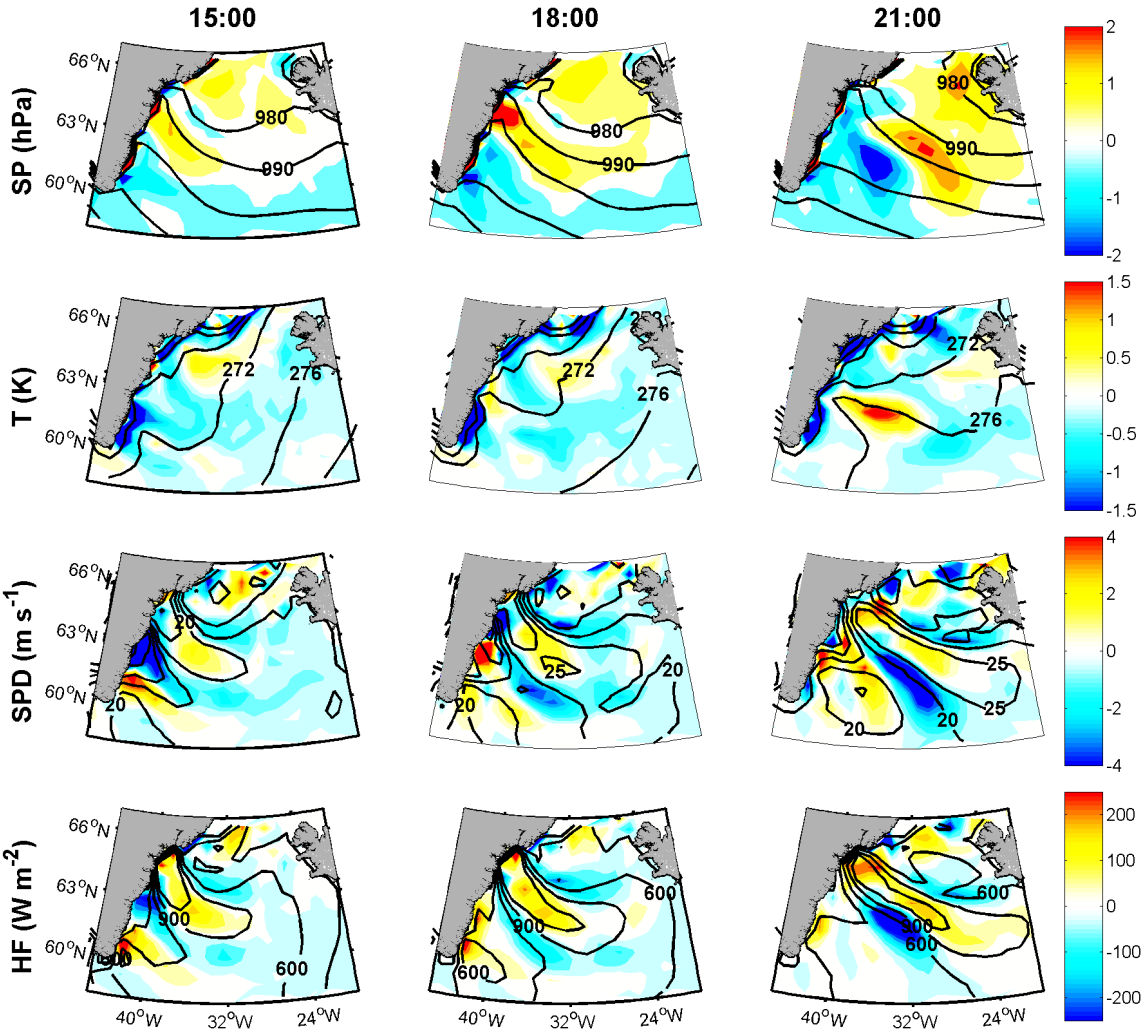

Figure 4-12: Black contour lines: Evolution of the surface pressure, temperature, wind speed and heat fluxes for the strong event in WRF60 from the simulation with the two-way nesting. Contour lines are every 10 hPa, 4 K, 5 m s^{-1} and 300 W m^{-2} respectively. Filled contours: Differences between the simulations with the one- and two-way nesting. Positive values indicate that that the displayed quantity is higher in the simulation that allows for feedbacks from the inner domains compared to the one without feedbacks. Positive heat fluxes represent a heat flux from the ocean to the atmosphere.

event with the WRF model in a 60 km (WRF60), a 20 km (WRF20) and a 5 km (WRF5) resolution domain with a smoothed and a regular topography. I have found that these different resolutions result in different representations of the wind field and its underlying dynamics. The differences are present for both events, but they are larger for the strong one. Since the boundary and initial conditions for the two events from ERA-I, as well as the obtained forces, are representative of the composite, the sensitivity to model resolution is likely a common feature of DWE. If the model is run on a 5 km resolution grid but with a 60 km resolution topography, there are still significant differences even though their overall magnitude is reduced. Thus, both a high resolution model and high resolution topography are needed to simulate the full extent of DWE.

The largest differences between the WRF5, WRF20 and WRF60 domain occur at the southwestern side of the valley near the surface and over the slope inside the valley (Figure 4-3). The first could be attributed to a stronger pressure gradient build-up when the flow is dammed against the barrier, similar to barrier winds at the coast [Moore and Renfrew, 2005, Petersen et al., 2009, Harden et al., 2011], but here the barrier is represented by the southwestern side of the valley and rotation is likely less important due to the smaller scale. There is a sharp turning of the isobars inside the valley (Figure 4-1). Over the upper part of the slope the pressure gradient is accelerating the flow, whereas it is decelerating the flow over the lower part (Figure 4-6). Thus, the coarser representation of the topography and smaller pressure gradients in the lower resolution domains are associated with a weaker flow near the southwestern side of the valley and a reduced horizontal and vertical wind shear. When the model is run on a 5 km resolution grid but with a 60 km resolution topography, the flow field is similar to the one in the WRF60 domain which emphasizes the role of the topography.

In addition, there is a steep mountain wave in WRF5 with the regular topography near the end of the slope where the wind speeds are particularly strong (Figure 4-4).

Previous studies suggest that mountain waves are associated with a large vertical momentum flux that accelerates the surface winds [Durran, 1986, Bacmeister and Pierrehumbert, 1988, Durran, 2003]. WRF60 does not resolve the full extent of the vertical momentum transfer. If the 60 km resolution topography is used, the vertical momentum flux in WRF5 is reduced, but still larger compared to WRF60 (Figure 4-8). The differences between WRF5 with the smoothed and regular topography are solely due to the resolution of the topography. They likely arise because the vertical momentum flux due to the cross mountain pressure drag is sensitive to the terrain slope [Doyle et al., 2005]. The fact that the magnitude of the vertical momentum flux in WRF5 with the 60 km resolution topography is still larger than in WRF60 emphasizes the role of small-scale model dynamics. I conclude that surface wind speeds over the slope are sensitive to both model and topography resolution, but also that these two are connected. A high model resolution is needed in order to simulate the wave dynamics, but the strength of the wave dynamics depends on the terrain slope.

Since the cross mountain pressure drag is sensitive to the terrain slope, differences in the obtained magnitude of the ambient pressure gradient F_S are expected. The fact that the gravitational acceleration F_G also attains a different magnitude in WRF5 and WRF60 could be explained by interactions between F_G and F_S, especially during the strong wind event. Specifically, horizontal pressure gradient perturbations induced by the mountain wave intensify the temperature deficit at exactly those locations where the slope is steepest, thus resulting in a larger gravitational acceleration in WRF5 compared to WRF60 (Figure 4-9). Simultaneously, the downslope advection of stratified air leads to a cold air pool at the end of the slope, likely because the air accumulates at the narrow valley outlet (Figure 4-10). This is associated with a decrease of F_S that is larger in WRF5 and could result in a different wind speed evolution in WRF5, WRF20 and WRF60 (Figures 4-2 and 4-12). Currently, the WRF model does not support a gravity wave parametrization for simulations of

this duration and resolution, though these results suggest that future releases might benefit from it. Since the wave drag can interact with the gravitational acceleration, any parametrization would have to take this interaction into account.

The different evolution of the wind event in WRF5 and WRF60 is more pronounced for the strong wind event than for the weak one. As Poulos et al. [2000] suggest, this could be explained by the smaller Froude number for the weak wind event which indicates that the katabatic component of the flow is more pronounced. Since the gravitational acceleration is less sensitive to resolution when averaged over the slope, the evolution of the weak wind event is more similar in WRF5 and WRF60.

Even a 5 km resolution could potentially misrepresent non-hydrostatic gravity waves, and alias energy into longer wave-length hydrostatic waves [Reinecke and Durran, 2009]. Thus, I compared the flow and potential temperature field from WRF5 to an additional domain with a horizontal grid spacing of 1.67 km and 45 vertical levels (WRF1.7). I find that the surface and near surface winds in WRF5 and WRF1.7 are in good agreement (Figures 4-2 and 4-4), and that WRF5 captures the steepness of the topography. The largest differences between the two domains occur downstream of the coast, where WRF1.7 resolves a series of lee waves that are smoothed in WRF5. Since these lee waves do not affect the near surface wind field over the slope, I conclude that the 5 km resolution is adequate for the analysis in this study. Moreover, the wind speed in WRF5 is in good agreement with observations from a local weather station (Figure 4-2), indicating that the effect of non-hydrostatic waves is limited near the surface and that the valley is wide enough to force primarily longer wavelength hydrostatic waves. For steeper topography, faster flows and higher Froude numbers, non-hydrostatic effects can become more important [Ulrich, 1991] and a separation of the pressure gradient force might not be meaningful anymore. To simulate wind events under such conditions, an even higher resolution is recommended.

The effects of resolving small-scale processes over the slope extend downstream over the Irminger Sea (Figure 4-12). Thus, the faster downslope winds in WRF5 for

the strong wind event do not only influence the local population and environment in Ammassalik, but have further reaching climatic consequences. If feedbacks from WRF5 and WRF20 are included in WRF60, even large-scale fields such as surface pressure and temperature are affected. It is possible that the faster decrease of the ambient pressure gradient also affects the larger-scale pressure distribution. This could result in a diverging evolution of the synoptic situation. Additional studies are required to investigate how sensitive the large-scale evolution is to small-scale processes over steep topography.

Moreover, depending on whether the nesting in Ammassalik is one- or two-way, the downstream wind field and heat fluxes over the Irminger Sea have both a different distribution and magnitude with differences of up to $\sim$200 W m^{-2}. Since the turbulent heat fluxes depend on both wind speed and the air-sea temperature difference, the discrepancy between the simulations is likely a consequence of the faster and colder air in the WRF5 domain. This suggests that the differences arising from the narrower and more intense outflow region from the valley extend beyond the WRF5 domain boundaries, and that the temperature and wind speed differences concur in their effect on the latent and sensible heat fluxes. Convection in the ocean depends on the air sea heat exchange [Marshall and Schott, 1999], and changes in the spatial distribution of the heat fluxes could result in shifts of the atmospheric forcing region relative to the ocean convection centers. Thus, including or neglecting small-scale processes in the Ammassalik valley in the model could have implications for the model's ability to correctly force deep water formation.

Chapter 5

Conclusion

This thesis was motivated by the bigger question of what the role of strong atmospheric flows across Greenland's coast is for the surface energy balance over the ice sheet and the heat fluxes over the subpolar North Atlantic and Nordic Seas. To tackle this question, I started by carrying out the first comprehensive study of the large-scale characteristics, dynamics, and influences of strong cross-coastal wind events over Greenland. I showed that high-speed offshore winds are associated with large ocean heat losses over major ocean convection regions and that onshore winds can result in melting over the ice sheet or precondition melting later in the year. I found that both types of wind events result from the interaction of large-scale atmospheric flows with the high Greenland topography, and was able to connect previously identified large-scale climate modes with the occurrence of these wind events and thus their influences on the ice and ocean.

Amongst the downslope wind events that I investigated in Chapter 2, those in southeast Greenland are unique. In this region, the flow, that originates in the far north, is funneled from the vast ice sheet into the narrow valley of Ammassalik, where it can reach hurricane intensity. This suggests that the cold air, which formed over the northern ice sheet, is suddenly released during the wind events and spills out over the ocean, where the cold and strong winds drive large heat fluxes. Thus, in Chapter 3, I

focused on these unique wind events and studied their local characteristics, dynamics and impacts in more detail. Thereby I showed that the local topographic forcing of the valley and the large-scale synoptic forcing of the atmosphere reinforce each other to create these high-speed wind events that have significant impacts on the coastal sea ice cover and on the heat losses over the Irminger Sea.

By comparing weather station observations of the wind events in Ammassalik with the reanalysis used in Chapters 2 and 3, I found that — even though the reanalysis provided a reliable large-scale description of the wind events — it underestimated the local wind speed inside the valley, suggesting that it did not resolve relevant dynamics of the wind events. Therefore, in Chapter 4, I simulated the wind events with a higher resolution atmospheric model. I showed that both a high model resolution and a high topographic resolution are needed to simulate the large-amplitude mountain wave and the associated vertical momentum flux that accelerates the downslope flow over the steep slope in Ammassalik. Using a different resolution locally in the valley has consequences for the distribution and evolution of the heat fluxes over a large area of the Irminger Sea even far downstream of Ammassalik.

Thus, this study suggests that wind events across the coast (specifically the southeast coast) have important consequences for the surface energy balance of the ice sheet and the subpolar North Atlantic Ocean. Southeast Greenland is a key region where the ice, ocean and atmosphere all interact with each other on a wide range of scales. In this thesis, I have covered scales ranging from the atmospheric Rossby wave scale (on the order of several 1000 km) to the mountain wave scale (on the order of 10 km). I have found that the large-scale synoptic forcing is an important component of the forcing of strong downslope wind events in southeast Greenland, but a crucial part of their dynamics occurs on smaller scales of less than 20 km. Therefore, the results presented in this thesis contribute to the scientific understanding of ice-ocean-atmosphere interactions around Greenland, and they will be useful for future studies. In particular:

- Investigations of the mass balance of the ice sheet will benefit from knowledge of the onshore winds across the southeast Greenland coast, even if they occur in winter when the temperature is below freezing. The influence of winter circulation on melting later in the year has not previously been acknowledged.

- Knowledge of the offshore winds across the southeast coast can improve estimates of the ocean heat fluxes, especially over the Irminger Sea, and thus is relevant for appropriate simulations of deep water formation. Moreover, ice sheet models might profit from including strong along-fjord winds and their influences on the sea ice near floating tongue glaciers.

- The findings about the dynamics of the winds in Ammassalik can help to predict the strong winds, and also provide useful information for the design of climate models. Specifically, these models need to resolve dynamics on the small scales of the local topography, or have adequate parameterizations that take the full complexity of the flow into account.

Many questions still remain open:

- How far do small-scale processes over steep topography in key regions such as southeast Greenland influence larger scales? Longer ensemble simulations, covering larger domains, are needed to address this question.

- How will future climate change, e.g. a shift in the jet stream and mean wind pattern, influence the distribution of melting over Greenland? What is the role of the present and past atmospheric circulation for Greenland's current surface elevation?

- Future warming of the subpolar North Atlantic ocean can affect the submarine melt rate of outlet glaciers (e.g. Straneo and Heimbach [2013]), but also surface melting through onshore winds across the southeast coast. How important will these ocean contributions be for the mass balance of the Greenland ice sheet

when the temperature of the surface ocean continues to increase? Warming of the subpolar North Atlantic can also result in a larger land-sea temperature contrast and thereby affect atmospheric dynamics. Thus, Greenland is a region of complex, inter-twined ice-ocean-atmosphere interactions and many of the details are still unknown. More studies are needed to pin down individual processes that contribute to the energy balance of the ice sheet, and to investigate how they relate to larger scale climate variability.

Bibliography

A. P. Ahlstrøm, S. B. Andersen, M. L. Andersen, M. Citterio, K. Edelvang, P. Gravesen, H. Machguth, F. M. Nick, S. Nielsen, and A. Weidick. Programme for monitoring of the greenland ice sheet (promice): first temperature and ablation records. *Geological Survey of Denmark and Greenland Bulletin*, 23:73–76, 2011.

J. M. Amundson, M. Fahnestock, M. Truffer, J. Brown, MP Lüthi, and RJ Motyka. Ice mélange dynamics and implications for terminus stability, jakobshavn isbræ, greenland. *Journal of Geophysical Research*, 115:F01005, 2010.

J. T. Bacmeister and R. T. Pierrehumbert. On high-drag states of nonlinear stratified flow over an obstacle. *Journal of the atmospheric sciences*, 45(1):63–80, 1988.

A. Barnston and R. Livezey. Classification, seasonality and persistence of low-frequency atmospheric circulation patterns. *Mon. Wea. Rev.*, 115(6):1083–1126, 1987.

G. B. Bonan. *Ecological climatology: concepts and applications*. Cambridge University Press, 2002.

C. W. Böning, W. R. Bryan, W. R. Holland, and R. Döscher. Deep-water formation and meridional overturning in a high-resolution model of the north atlantic. *Journal of Physical Oceanography*, 26:1142–1164, 1996.

E. W. Born and J. B. Boecher. *The ecology of Greenland*. Atuakkiorfik Education, 2000.

J. E. Box, X. Fettweis, J. C. Stroeve, M. Tedesco, D. K. Hall, and K. Steffen. Greenland ice sheet albedo feedback: thermodynamics and atmospheric drivers. *The Cryosphere*, 6(4):821–839, 2012.

D. H. Bromwich and D. D. Kurtz. Katabatic wind forcing of the terra nova bay polynya. *Journal of Geophysical Research*, 89(C3):3561–3572, 1984.

D. H. Bromwich, Y. Du, and K. M. Hines. Wintertime surface winds over the greenland ice sheet. *Mon. Wea. Rev.*, 124(9):1941–1947, 1996.

H. L. Bryden, H. R. Longworth, and S. A. Cunningham. Slowing of the atlantic meridional overturning circulation at 25 n. *Nature*, 438(7068):655–657, 2005.

J. Cappelen. Dmi monthly climate data collection 1768-2010, denmark, the faroe islands and greenland. Technical report, Danish Meteorological Institute, 2011.

L. S. Carstensen and B. V. Jorgensen. Weather and climate data from greenland 1958-2009. Technical report, Danish Meteorological Institute, 2010.

J. J. Cassano and T. R. Parish. An analysis of the nonhydrostatic dynamics in numerically simulated antarctic katabatic flows*. *Journal of the atmospheric sciences*, 57(6):891–898, 2000.

C. Cassou, L. Terray, J. W. Hurrell, and C. Deser. North atlantic winter climate regimes: Spatial asymmetry, stationarity with time, and oceanic forcing. *Journal of Climate*, 17(5):1055–1068, 2004.

D. Cavalieri, T. Markus, and J. Comiso. Amsr-e/aqua daily l3 12.5 km brightness temperature, sea ice concentration, & snow depth polar grids v002, january to may, 2003 to 2010. *National Snow and Ice Data Center. Boulder, Colorado\ http://nsidc.org*, 2004.

E. K. M. Chang, S. Lee, and K. L. Swanson. Storm track dynamics. *Journal of Climate*, 15(16):2163–2183, 2002.

J. G. Charney and A. Eliassen. A numerical method for predicting the perturbations of the middle latitude westerlies. *Tellus*, 1(2):38–54, 1949.

A. H. Chaudhuri, R. M. Ponte, and A. T. Nguyen. A comparison of atmospheric reanalysis products for the arctic ocean and implications for uncertainties in air–sea fluxes. *Journal of Climate*, 27(14):5411–5421, 2014.

F. Chen and J. Dudhia. Coupling an advanced land surface-hydrology model with the penn state-ncar mm5 modeling system. part i: Model implementation and sensitivity. *Monthly Weather Review*, 129(4):569–585, 2001.

P. U. Clark, N. G. Pisias, T. F. Stocker, and A. J. Weaver. The role of the thermohaline circulation in abrupt climate change. *Nature*, 415(6874):863–869, 2002.

T. L. Clark, W. D. Hall, R. M. Kerr, D. Middleton, L. Radke, F. M. Ralph, P. J. Neiman, and D. Levinson. Origins of aircraft-damaging clear-air turbulence during the 9 december 1992 colorado downslope windstorm: Numerical simulations and comparison with observations. *Journal of the atmospheric sciences*, 57(8):1105–1131, 2000.

R. A. Clarke and J.-C. Gascard. The formation of labrador sea water. part i: Large-scale processes. *Journal of Physical Oceanography*, 13(10):1764–1778, 1983.

M. F. de Jong, H. M. van Aken, K. Våge, and R. S. Pickart. Convective mixing in the central irminger sea: 2002–2010. *Deep Sea Research Part I: Oceanographic Research Papers*, 63:36–51, 2012.

D. P. Dee, S. M. Uppala, A. J. Simmons, P. Berrisford, P. Poli, S. Kobayashi, U Andrae, M. A. Balmaseda, G. Balsamo, P. Bauer, P. Bechtold, A. C. M. Beljaars, L. van de Berg, J. Bidlot, N. Bormann, C. Delsol, R. Dragani, M. Fuentes, A. J. Geer, L. Haimberger, S. B. Healy, H. Hersbach, E. V. Holm, L. Isaksen, P. Kallberg, M. Koehler, M. Matricardi, A. P. McNally, B. M. Monge-Sanz, J.-J. Morcrette, B.-K. Park, C. Peubey, P. de Rosnay, C. Tavolato, J.-N. Thepaut, and F. Vitart. The era-interim reanalysis: configuration and performance of the data assimilation system. *Royal Meteorological Society*, 59:141–161, 2011.

P. A. Dodd, B. Rabe, E. Hansen, E. Falck, A. Mackensen, E. Rohling, C. Stedmon, and S. Kristiansen. The freshwater composition of the fram strait outflow derived from a decade of tracer measurements. *Journal of Geophysical Research: Oceans (1978–2012)*, 117(C11), 2012.

A. Dörnbrack and T. Dürbeck. Turbulent dispersion of aircraft exhausts in regions of breaking gravity waves. *Atmospheric Environment*, 32(18):3105–3112, 1998.

J. D. Doyle and M. A. Shapiro. Flow response to large-scale topography: The greenland tip jet. *Tellus*, 51(5):728–748, 1999.

J. D. Doyle, M. A. Shapiro, Q. Jiang, and D. L. Bartels. Large-amplitude mountain wave breaking over greenland. *J. Atmos. Sci.*, 62(9):3106–3126, 2005.

J. Dudhia. Numerical study of convection observed during the winter monsoon experiment using a mesoscale two-dimensional model. *Journal of the Atmospheric Sciences*, 46(20):3077–3107, 1989.

D. R. Durran. Another look at downslope windstorms. part i: The development of analogs to supercritical flow in an infinitely deep continuously stratified fluid. *J. Atmos. Sci.*, 43(21):2527–2543, 1986.

D. R. Durran. Mountain waves and downslope winds. *Meteor. Monogr*, 23:59–81, 1990.

D. R. Durran. Lee waves and mountain waves, 2003.

A. K. DuVivier and J. J. Cassano. Evaluation of wrf model resolution on simulated mesoscale winds and surface fluxes near greenland. *Monthly Weather Review*, 141 (3), 2013.

ECMWF. *IFS Documentation–Cy31r1, Part IV: Physical Processes*. Shinfield Park, Reading, RG2 9AX, England, 2010.

A. Eliassen and E. Palm. On the transfer of energy in stationary mountain waves. *Geofysiske Publikasjoner*, 22:1–23, 1961.

M. A. Estoque. A theoretical investigation of the sea breeze. *Quarterly Journal of the Royal Meteorological Society*, 87(372):136–146, 1961.

X. Fettweis, G. Mabille, M. Erpicum, S. Nicolay, and M. Van den Broeke. The 1958–2009 greenland ice sheet surface melt and the mid-tropospheric atmospheric circulation. *Climate Dynamics*, 36(1-2):139–159, 2011.

X. Fettweis, E. Hanna, C. Lang, A. Belleflamme, M. Erpicum, and H. Gallée. Important role of the mid-tropospheric atmospheric circulation in the recent surface melt increase over the greenland ice sheet. *Cryosphere (The)*, 7:241–248, 2013.

D. C. Fritts and M. J. Alexander. Gravity wave dynamics and effects in the middle atmosphere. *Reviews of Geophysics*, 41(1), 2003.

H. Gallée. Air-sea interactions over terra nova bay during winter: Simulation with a coupled atmosphere-polynya model. *Journal of Geophysical Research - all series*, 102:13–13, 1997.

J.-C. Gascard and R. A. Clarke. The formation of labrador sea water. part ii. mesoscale and smaller-scale processes. *Journal of Physical Oceanography*, 13(10): 1779–1797, 1983.

J.-M. Gherardi, L. Labeyrie, J. F. McManus, R. Francois, L. C. Skinner, and E. Cortijo. Evidence from the northeastern atlantic basin for variability in the rate of the meridional overturning circulation through the last deglaciation. *Earth and Planetary Science Letters*, 240(3):710–723, 2005.

A. E. Gill. *Atmosphere-ocean dynamics*, volume 30. Academic Pr, 1982.

H. Goosse, P. Y. Barriat, W. Lefebvre, M. F. Loutre, and V. Zunz. Introduction to climate dynamics and climate modeling. `http://www.climate.be/textbook`, 2015. Online textbook, accessed March 20, 2015.

S. Häkkinen, P. B. Rhines, and D. L. Worthen. Atmospheric blocking and atlantic multidecadal ocean variability. *Science*, 334(6056):655–659, 2011.

D. K. Hall, J. C. Comiso, N. E. DiGirolamo, C. A. Shuman, J. E. Box, and L. S. Koenig. Variability in the surface temperature and melt extent of the greenland ice sheet from modis. *Geophysical Research Letters*, 40(10):2114–2120, 2013.

E. Hanna, P. Huybrechts, J. Cappelen, K. Steffen, R. C. Bales, E. Burgess, J. R. McConnell, P. J. Steffensen, M. Van den Broeke, L. Wake, et al. Greenland ice sheet surface mass balance 1870 to 2010 based on twentieth century reanalysis, and

links with global climate forcing. *Journal of Geophysical Research: Atmospheres (1984–2012)*, 116(D24), 2011.

E. Hanna, J. M. Jones, J. J. Cappelen, S. H. Mernild, L. Wood, K. Steffen, and P. Huybrechts. The influence of north atlantic atmospheric and oceanic forcing effects on 1900–2010 greenland summer climate and ice melt/runoff. *International Journal of Climatology*, 33(4):862–880, 2013.

E. Hanna, X. Fettweis, S. H. Mernild, J. Cappelen, M. H. Ribergaard, C. A. Shuman, K. Steffen, L. Wood, and T. L. Mote. Atmospheric and oceanic climate forcing of the exceptional greenland ice sheet surface melt in summer 2012. *International Journal of Climatology*, 34(4):1022–1037, 2014.

A. Hannachi, T. Woollings, and K. Fraedrich. The north atlantic jet stream: a look at preferred positions, paths and transitions. *Quarterly Journal of the Royal Meteorological Society*, 138(665):862–877, 2012.

B. E. Harden and I. A. Renfrew. On the spatial distribution of high winds off southeast greenland. *Geophysical Research Letters*, 39(14):L14806, 2012.

B. E. Harden, I. A. Renfrew, and G. N. Petersen. A climatology of wintertime barrier winds off southeast greenland. *J. Climate*, 24:4701–4717, 2011.

G. Heinemann. The kabeg'97 field experiment: An aircraft-based study of katabatic wind dynamics over the greenland ice sheet. *Boundary-Layer Meteorology*, 93(1): 75–116, 1999.

G. Heinemann. Forcing and feedback mechanisms between the katabatic wind and sea in the coastal areas of polar ice sheets. *Global Atmosphere and Ocean System*, pages 169–201, 2003.

G. Heinemann and T. Klein. Modelling and observations of the katabatic flow dynamics over greenland. *Tellus*, 54 A:542–554, 2002.

J. P. Hennessey. Some aspects of wind power statistics. *J. Appl. Meteor. Climatol.*, 16(2):119–128, 1977.

R. Hock. Glacier melt: a review of processes and their modelling. *Progress in physical geography*, 29(3):362–391, 2005.

J. R. Holton and G. J. Hakim. *An introduction to dynamic meteorology*. Academic press, 2013.

S.-Y. Hong, J. Dudhia, and S.-H. Chen. A revised approach to ice microphysical processes for the bulk parameterization of clouds and precipitation. *Monthly Weather Review*, 132(1):103–120, 2004.

S.-Y. Hong, Y. Noh, and J. Dudhia. A new vertical diffusion package with an explicit treatment of entrainment processes. *Monthly Weather Review*, 134(9):2318–2341, 2006.

B. J. Hoskins, M. E. McIntyre, and A. W. Robertson. On the use and significance of isentropic potential vorticity maps. *Quarterly Journal of the Royal Meteorological Society*, 111(470):877–946, 1985.

J. T. Houghton, Y. D. J. G. Ding, D. J. Griggs, M. Noguer, P. J. van der Linden, X. Dai, K. Maskell, and C. A. Johnson. Climate change 2001: the scientific basis. 2001.

I. M. Howat, J. E. Box, Y. Ahn, A. Herrington, and E. M. McFadden. Seasonal variability in the dynamics of marine-terminating outlet glaciers in greenland. *Journal of Glaciology*, 56(198):601–613, 2010.

A. Hu, G. A. Meehl, W. Han, J. Yin, B. Wu, and M. Kimoto. Influence of continental ice retreat on future global climate. *Journal of Climate*, 26(10):3087–3111, 2013.

J. W. Hurrell. Decadal trends in the north atlantic oscillation: regional temperatures and precipitation. *Science*, 269(5224):676–679, 1995.

J. W. Hurrell and C. Deser. North atlantic climate variability: the role of the north atlantic oscillation. *Journal of Marine Systems*, 79(3):231–244, 2010.

Z. Janjic, T. Black, M. Pyle, B. Ferrier, H. Y. Chuang, D. Jovic, N. McKee, R. Rozumalski, J. Michalakes, D. Gill, et al. UserâĂŹs guide for the nmm core of the weather research and forecast (wrf) modeling system version 3. 2011.

P. A. Jiménez, J. Dudhia, J. F. González-Rouco, J. Navarro, J. P. Montávez, and E. García-Bustamante. A revised scheme for the wrf surface layer formulation. *Monthly Weather Review*, 140(3):898–918, 2012.

Y. Jin, S. E. Koch, Y.-L. Lin, F. M. Ralph, and C. Chen. Numerical simulations of an observed gravity current and gravity waves in an environment characterized by complex stratification and shear. *Journal of the atmospheric sciences*, 53(23): 3570–3588, 1996.

J. H. Jungclaus, H. Haak, M. Latif, and U. Mikolajewicz. Arctic-north atlantic interactions and multidecadal variability of the meridional overturning circulation. *J. Climate*, 18(19):4013–4031, 2005.

J. S. Kain and J. M. Fritsch. A one-dimensional entraining/detraining plume model and its application in convective parameterization. *Journal of the Atmospheric Sciences*, 47(23):2784–2802, 1990.

T. Klein and G. Heinemann. Interaction of katabatic winds and mesocyclones near the eastern coast of greenland. *Meteorological Applications*, 9:407–422, 2002.

J. E. Kristjánsson and H. McInnes. The impact of greenland on cyclone evolution in the north atlantic. *Quarterly Journal of the Royal Meteorological Society*, 125 (560):2819–2834, 1999.

J. E. Kristjánsson, S. Thorsteinsson, and G. F. Ulfarsson. Potential vorticity-based interpretation of the evolution of 'the greenhouse low', 2–3 february 1991. *Tellus A*, 51(2):233–248, 1999.

J. E. Kristjánsson, S. Thorsteinsson, and B. Røsting. Phase-locking of a rapidly developing extratropical cyclone by greenland's orography. *Quarterly Journal of the Royal Meteorological Society*, 135(645):1986–1998, 2009.

M. Kurz. On the dynamics of the splitting process of cyclones near southern greenland. *Meteorologische Zeitschrift*, 13(2):143–148, 2004.

T. P. Lane, J. D. Doyle, R. D. Sharman, M. A. Shapiro, and C. D. Watson. Statistics and dynamics of aircraft encounters of turbulence over greenland. *Monthly Weather Review*, 137(8):2687–2702, 2009.

K. L. Lavender, R. E. Davis, and B. Owens. Mid-depth recirculation observed in the interior labrador and irminger seas by direct velocity measurements. *Nature*, 109 (6800):66–69, 2000.

J. Lynch-Stieglitz, J. F. Adkins, W. B. Curry, T. Dokken, I. R. Hall, J. C. Herguera, J. J.-M. Hirschi, E. V. Ivanova, C. Kissel, O. Marchal, et al. Atlantic meridional overturning circulation during the last glacial maximum. *science*, 316(5821):66–69, 2007.

L. Mahrt. Momentum balance of gravity flows. *J. Atmos. Sci.*, 39:2701–2711, 1982.

S. Manabe and R. J. Stouffer. Simulation of abrupt climate change induced by freshwater input to the north atlantic ocean. *Nature*, 378(6553):165–167, 1995.

R. Marsh, D. Desbruyeres, J. L. Bamber, B. A. De Cuevas, A. C. Coward, and Y. Aksenov. Short-term impacts of enhanced greenland freshwater fluxes in an eddy-permitting ocean model. *Ocean Science*, 6(3):749–760, 2010.

J. Marshall and F. Schott. Open-ocean convection: Observations, theory, and models. *Reviews of Geophysics*, 37(1):1–64, 1999.

N. A. McFarlane. The effect of orographically excited gravity wave drag on the general circulation of the lower stratosphere and troposphere. *Journal of the atmospheric sciences*, 44(14):1775–1800, 1987.

T. L. McKnight and D. Hess. Foehn/chinoonk winds. in. *Physical Geography: A Landscape Appreciation*, page 132, 2000.

J. F. McManus, R. Francois, J.-M. Gherardi, L. D. Keigwin, and S. Brown-Leger. Collapse and rapid resumption of atlantic meridional circulation linked to deglacial climate changes. *Nature*, 428(6985):834–837, 2004.

S. H. Mernild, B. U. Hansen, B. H. Jakobsen, and B. Hasholt. Climatic conditions at the mittivakkat glacier catchment (1994–2006), ammassalik island, se greenland, and in a 109-year perspective (1898–2006). *Geografisk Tidsskrift-Danish Journal of Geography*, 108(1):51–72, 2008.

J. Michalakes, J. Dudhia, D. Gill, T. Henderson, J. Klemp, W. Skamarock, and W. Wang. The weather research and forecast model: software architecture and performance. In *Proceedings of the 11th ECMWF Workshop on the Use of High Performance Computing In Meteorology*, volume 25, page 29. World Scientific, 2004.

B. J. Mills and M. R. Anderson. Monitoring a piteraq storm system using dmsp imagery and quikscat wind data. In *12th Conf. on Satellite Meteorology and Oceanography*, Long Beach, CA, 2003. American Meteorological Society.

E. J Mlawer, S. J. Taubman, P. D. Brown, M. J. Iacono, and S. A. Clough. Radiative transfer for inhomogeneous atmospheres: Rrtm, a validated correlated-k model for the longwave. *Journal of Geophysical Research: Atmospheres (1984–2012)*, 102 (D14):16663–16682, 1997.

G. W. K. Moore. Gale force winds over the irminger sea to the east of cape farewell, greenland. *Geophysical Research Letters*, 30(17):1894, 2003.

G. W. K. Moore. A new look at greenland flow distortion and its impact on barrier flow, tip jets and coastal oceanography. *Geophysical Research Letters*, 39(22), 2012.

G. W. K. Moore and I. A. Renfrew. Tip jets and barrier winds: A quikscat climatology of high wind speed events around greenland. *J. Climate*, 18(18):3713–3725, 2005.

G. W. K. Moore and I. A. Renfrew. Cold european winters: interplay between the nao and the east atlantic mode. *Royal Meteorological Society*, 2011.

G. W. K. Moore and P. W. Vachon. A polar low over the labrador sea: Interactions with topography and an upper-level potential vorticity anomaly, and an observation by radarsat-1 sar. *Geophysical research letters*, 29(16):20–1, 2002.

G. W. K. Moore, M. C. Reader, J. York, and S. Sathiyamoorthy. Polar lows in the labrador sea. *Tellus A*, 48(1):17–40, 1996.

G. W. K. Moore, K. Alverson, and I. A. Renfrew. A reconstruction of the air-sea interaction associated with the weddell polynya. *J. Phys. Oceanogr.*, 32(6):1685–1698, 2002.

G. W. K. Moore, R. S. Pickart, and I. A. Renfrew. Complexities in the climate of the subpolar north atlantic: a case study from the winter of 2007. *Royal Meteorological Society*, 2011.

G. W. K. Moore, I. A. Renfrew, and R. S. Pickart. Spatial distribution of air-sea fluxes over the sub-polar north atlantic ocean. 2012. Submitted to Geophysical Research Letters.

G. W. K. Moore, I. A. Renfrew, and J. J. Cassano. Greenland plateau jets. *Tellus A*, 65, 2013.

T. L. Mote. Greenland surface melt trends 1973–2007: Evidence of a large increase in 2007. *Geophysical Research Letters*, 34(22), 2007.

E. Mursch-Radlgruber. Observations of flow structure in a small forested valley system. *Theoretical and applied climatology*, 52(1-2):3–17, 1995.

W. Neff, G. P. Compo, F. M. Ralph, and M. D. Shupe. Continental heat anomalies and the extreme melting of the greenland ice surface in 2012 and 1889. *Journal of Geophysical Research: Atmospheres*, 119(11):6520–6536, 2014.

H. Ólafsson and P. Bougeault. The effect of rotation and surface friction on orographic drag. *Journal of the atmospheric sciences*, 54(1):193–210, 1997.

M. Oltmanns, F. Straneo, G. W. K. Moore, and S. H. Mernild. Strong downslope wind events in ammassalik, southeast greenland. *Journal of Climate*, 27(3), 2014.

I. Orlanski. A rational subdivision of scales for atmospheric processes. *Bulletin of the American Meteorological Society*, 56:527–530, 1975.

S. D. Outten, I. A. Renfrew, and G. N. Petersen. An easterly tip jet off cape farewell, greenland. ii: Simulations and dynamics. *Quarterly Journal of the Royal Meteorological Society*, 135(645):1934–1949, 2009.

J. E. Overland, J. A. Francis, E. Hanna, and M. Wang. The recent shift in early summer arctic atmospheric circulation. *Geophysical Research Letters*, 39(19), 2012.

J. P. Palutikof, B. B. Brabson, D. H. Lister, and S. T. Adcock. A review of methods to calculate extreme wind speeds. *J. Appl. Meteor. Climatol.*, 6(02):119–132, 1999.

T. R. Parish and D. H. Bromwich. The surface windfield over the antarctic ice sheets. *Nature*, 328(6125):51–54, 1987.

T. R. Parish and J. J. Cassano. Forcing of the wintertime antarctic boundary layer winds from the ncep-ncar global reanalysis. *J. Appl. Meteor. Climatol.*, 40(4): 810–821, 2001.

T. R. Parish and J. J. Cassano. The role of katabatic winds on the antarctic surface wind regime. *Mon. Wea. Rev.*, 131(2):317–333, 2003.

E. G. Pavia and J. J. O'Brien. Weibull statistics of wind speed over the ocean. *J. Appl. Meteor. Climatol.*, 25:1324–1332, 1986.

G. N. Petersen and I. A. Renfrew. Aircraft-based observations of air–sea fluxes over denmark strait and the irminger sea during high wind speed conditions. *Quarterly Journal of the Royal Meteorological Society*, 135(645):2030–2045, 2009.

G. N. Petersen, I. A. Renfrew, and G. W. K. Moore. An overview of barrier winds off southeastern greenland during the greenland flow distortion experiment. *Quaterly Journal of the Royal Meteorological Society*, 135:1950–1967, 2009.

P. Pettré, C. Payan, and T. R. Parish. Interaction of katabatic flow with local thermal effects in a coastal region of adelie land, east antarctica. *Journal of Geophysical Research*, 98(D6):10429–10, 1993.

R. S. Pickart, M. A. Spall, M. H. Ribergaard, G. W. K. Moore, and R. F. Milliff. Deep convection in the irminger sea forced by the greenland tip jet. *Nature*, 424 (6945):152–156, 2003a.

R. S. Pickart, F. Straneo, and G. W. K. Moore. Is labrador sea water formed in the irminger basin? *Deep Sea Research Part I: Oceanographic Research Papers*, 50(1): 23–52, 2003b.

G. S. Poulos, J. E. Bossert, T. B. McKee, and R. A. Pielke. The interaction of katabatic flow and mountain waves. part i: Observations and idealized simulations. *J. Atmos. Sci.*, 57(12):1919–1936, 2000.

G. S. Poulos, J. E. Bossert, T. B. McKee, and R. A. Pielke Sr. The interaction of katabatic flow and mountain waves. part ii: case study analysis and conceptual model. *J. Atmos. Sci.*, 64(6):1857–1879, 2007.

F. M. Ralph, P. J. Neiman, and D. Levinson. Lidar observations of a breaking mountain wave associated with extreme turbulence. *Geophysical research letters*, 24(6):663–666, 1997.

L. Rasmussen. *Greenland winds and satellite imagery.* The Danish Meteorological Institute, 1989.

P. A. Reinecke and D. R. Durran. The overamplification of gravity waves in numerical solutions to flow over topography. *Monthly Weather Review*, 137(5):1533–1549, 2009.

I. A. Renfrew and P. S. Anderson. The surface climatology of an ordinary katabatic wind regime in coats land, antarctica. *Tellus*, 54(5):463–484, 2002.

I. A. Renfrew, G. W. K. Moore, J. E. Kristjánsson, H. Olafsson, S. L. Gray, G. N. Petersen, K. Bovis, I. Fore, T. Haine, C. Hay, et al. The greenland flow distortion experiment. *Bull. Amer. Meteor. Soc.*, 89(9):1307–1324, 2008.

I. A. Renfrew, S. D. Outten, and G. W. K. Moore. An easterly tip jet off cape farewell, greenland. i: Aircraft observations. *Quarterly Journal of the Royal Meteorological Society*, 135(645):1919–1933, 2009a.

I. A. Renfrew, G. N. Petersen, D. A. J. Sproson, G. W. K. Moore, H. Adiwidjaja, S. Zhang, and R. North. A comparison of aircraft-based surface-layer observations over denmark strait and the irminger sea with meteorological analyses and quikscat winds. *Quarterly Journal of the Royal Meteorological Society*, 135(645):2046–2066, 2009b.

L. Ricciardulli and F. Wentz. Reprocessed quikscat (v04) wind vectors with ku-2011 geophysical model function. *Remote Sensing Systems Technical Report*, 43011, 2011.

B. Rudels and D. Quadfasel. Convection and deep water formation in the arctic ocean-greenland sea system. *Journal of Marine Systems*, 2(3):435–450, 1991.

C. L. Sabine, R. A. Feely, N. Gruber, R. M. Key, K. Lee, J. L. Bullister, R. Wanninkhof, C. S. Wong, D. W. R. Wallace, B. Tilbrook, et al. The oceanic sink for anthropogenic co2. *Science*, 305(5682):367–371, 2004.

T. Sampe and S. Xie. Mapping high sea winds from space: A global climatology. *Bulletin of the American Meteorological Society*, 88(12):1965–1978, 2007.

S. Sathiyamoorthy and G. W. K. Moore. Buoyancy flux at ocean weather station bravo. *J. Phys. Oceanogr.*, 32(2):458–474, 2002.

S. C. Scherrer, M. Croci-Maspoli, C. Schwierz, and C. Appenzeller. Two-dimensional indices of atmospheric blocking and their statistical relationship with winter climate patterns in the euro-atlantic region. *International journal of climatology*, 26(2): 233–249, 2006.

W. Schwerdtfeger. Weather and climate of the antarctic. *Amsterdam: Elsevier,/ c1984*, 1, 1984.

R. S. Scorer. Causes and consequences of standing waves. In *Proceedings of the Symposium on Mountain Meteorology: Colorado State University. Atmospheric Science Paper*, volume 122, 1967.

M. C. Serreze and R. G. Barry. *The Arctic climate system*. Cambridge University Press, 2005.

M. C. Serreze, A. P. Barrett, A. G. Slater, M. Steele, J. Zhang, and K. E. Trenberth. The large-scale energy budget of the arctic. *Journal of Geophysical Research: Atmospheres (1984–2012)*, 112(D11), 2007.

A. Shepherd, E. R. Ivins, A. Geruo, V. R. Barletta, M. J. Bentley, S. Bettadpur, K. H. Briggs, D. H. Bromwich, R. Forsberg, N. Galin, et al. A reconciled estimate of ice-sheet mass balance. *Science*, 338(6111):1183–1189, 2012.

G. Siedler, J. Gould, and J. A. Church. *Ocean circulation and climate: observing and modelling the global ocean*, volume 103. Academic Press, 2001.

J. E. Simpson. *Sea breeze and local winds*. Cambridge University Press, 1994.

W. C. Skamarock. Evaluating mesoscale nwp models using kinetic energy spectra. *Monthly Weather Review*, 132(12):3019–3032, 2004.

W. C. Skamarock, J. B. Klemp, J. Dudhia, D. O. Gill, and D. M. Barker. Coauthors, 2008: A description of the advanced research wrf version 3. ncar technical note. Technical report, NCAR/TN–475+ STR, 2005.

R. B. Skeie, J. E. Kristjánsson, H. Ólafsson, and B. Røsting. Dynamical processes related to cyclone development near greenland. *Meteorologische Zeitschrift*, 15(2): 147–156, 2006.

R. B. Smith. On severe downslope winds. *J. Atmos. Sci.*, 42(23):2597–2603, 1985.

R. B. Smith. Hydrostatic airflow over mountains. *Advances in Geophysics*, 31:1–41, 1989.

G. Spreen, L. Kaleschke, and G. Heygster. Sea ice remote sensing using amsr-e 89-ghz channels. *Journal of Geophysical Research*, 113(C2):C02, 2008.

D. Stammer. Response of the global ocean to greenland and antarctic ice melting. *Journal of Geophysical Research: Oceans (1978–2012)*, 113(C6), 2008.

K. Steffen, J. E. Box, and W. Abdalati. Greenland climate network: Gc-net. *US Army Cold Regions Reattach and Engineering (CRREL), CRREL Special Report*, pages 98–103, 1996.

R. H. Stewart. *Introduction to physical oceanography*. Texas A & M University, 2004.

R. J. Stouffer, J. Yin, J. M. Gregory, K. W. Dixon, M. J. Spelman, W. Hurlin, A. J. Weaver, M. Eby, G. M. Flato, H. Hasumi, et al. Investigating the causes of the response of the thermohaline circulation to past and future climate changes. *J. Climate*, 19(8):1365–1387, 2006.

F. Straneo and P. Heimbach. North atlantic warming and the retreat of greenland's outlet glaciers. *Nature*, 504(7478):36–43, 2013.

M. Sturm, J. Holmgren, and G. E. Liston. A seasonal snow cover classification system for local to global applications. *Journal of Climate*, 8(5):1261–1283, 1995.

M. Sturm, J. Holmgren, M. König, and K. Morris. The thermal conductivity of seasonal snow. *Journal of Glaciology*, 43(143):26–41, 1997.

M. Sturm, B. Taras, G. E. Liston, C. Derksen, T. Jonas, and J. Lea. Estimating snow water equivalent using snow depth data and climate classes. *Journal of Hydrometeorology*, 11(6):1380–1394, 2010.

U. Survey. Atlantic meridional overturning circulation. `http://www.eoearth.org/view/article/150290`, 2012.

D. A. Sutherland, F. Straneo, G. B. Stenson, F. J. M. Davidson, M. O. Hammill, and A. Rosing-Asvid. Atlantic water variability on the se greenland continental shelf and its relationship to sst and bathymetry. *Journal of Geophysical Research: Oceans*, 2013.

L. D. Talley and M. S. McCartney. Distribution and circulation of labrador sea water. *Journal of Physical Oceanography*, 12(11):1189–1205, 1982.

K. E. Trenberth and J. M. Caron. Estimates of meridional atmosphere and ocean heat transports. *Journal of Climate*, 14(16):3433–3443, 2001.

M. Tsukernik, D. N. Kindig, and M. C. Serreze. Characteristics of winter cyclone activity in the northern north atlantic: Insights from observations and regional modeling. *Journal of Geophysical Research: Atmospheres (1984–2012)*, 112(D3), 2007.

M. Tsukernik, C. Deser, M. Alexander, and R. Tomas. Atmospheric forcing of fram strait sea ice export: a closer look. *Climate dynamics*, 35(7-8):1349–1360, 2010.

W. Ulrich. A comparison between hydrostatic and nonhydrostatic simulations of gravity currents and their interaction with orography. *Meteorology and Atmospheric Physics*, 46(1-2):1–13, 1991.

K. Vage. Circulation and convection in the irminger sea. Technical report, DTIC Document, 2010.

K. Våge, T. Spengler, H. C. Davies, and R. S. Pickart. Multi-event analysis of the westerly greenland tip jet based upon 45 winters in era-40. *Quarterly Journal of the Royal Meteorological Society*, 135(645):1999–2011, 2009.

K. Våge, R. S. Pickart, A. Sarafanov, Ø. Knutsen, H. Mercier, P. Lherminier, H. M. Van Aken, J. Meincke, D. Quadfasel, and S. Bacon. The irminger gyre: Circulation, convection, and interannual variability. *Deep Sea Research Part I: Oceanographic Research Papers*, 58(5):590–614, 2011.

J. H. van Angelen, M. R. van den Broeke, and W. J. van de Berg. Momentum budget of the atmospheric boundary layer over the greenland ice sheet and its surrounding seas. *Journal of Geophysical Research*, 116(D10):D10101, 2011.

M. Van Den Broeke, J. Bamber, J. Ettema, E. Rignot, E. Schrama, W. J. Van de Berg, E. Van Meijgaard, I. Velicogna, and B. Wouters. Partitioning recent greenland mass loss. *Science*, 326(5955):984, 2009.

M. R. Van den Broeke and N. P. M. Van Lipzig. Factors controlling the near-surface wind field in antarctica*. *Mon. Wea. Rev.*, 131(4):733–743, 2003.

M. R. Van den Broeke, N. P. M. Van Lipzig, and E. Van Meijgaard. Momentum budget of the east antarctic atmospheric boundary layer: results of a regional climate model. *J. Atmos. Sci.*, 59(21):3117–3129, 2002.

M. Vellinga and R. A. Wood. Global climatic impacts of a collapse of the atlantic thermohaline circulation. *Climatic Change*, 54(3):251–267, 2002.

J. E. Walsh, W. L. Chapman, and D. H. Portis. Arctic cloud fraction and radiative fluxes in atmospheric reanalyses. *Journal of Climate*, 22(9):2316–2334, 2009.

J. I. Walter, E. Jason, S. Tulaczyk, E. E. Brodsky, I. M. Howat, A. H. N. Yushin, and A. Brown. Oceanic mechanical forcing of a marine-terminating greenland glacier. *Annals of Glaciology*, 53(60):181, 2012.

W. Weijer, M. E. Maltrud, M. W. Hecht, H. A. Dijkstra, and M. A. Kliphuis. Response of the atlantic ocean circulation to greenland ice sheet melting in a strongly-eddying ocean model. *Geophysical Research Letters*, 39(9), 2012.

T. Woollings, B. Hoskins, M. Blackburn, and P. Berrisford. A new rossby wave-breaking interpretation of the north atlantic oscillation. *Journal of the Atmospheric Sciences*, 65(2):609–626, 2008.

T. Woollings, A. Hannachi, and B. Hoskins. Variability of the north atlantic eddy-driven jet stream. *Quarterly Journal of the Royal Meteorological Society*, 136(649): 856–868, 2010.

X. Zhang, J. E. Walsh, J. Zhang, U. S. Bhatt, and M. Ikeda. Climatology and interannual variability of arctic cyclone activity: 1948-2002. *Journal of Climate*, 17(12):2300–2317, 2004.

Y. Zhang, D. J. Seidel, J. C. Golaz, C. Deser, and R. A. Tomas. Climatological characteristics of arctic and antarctic surface-based inversions. *J. Climate*, 2011.